August 2023

Synthesis, Characterization, and Simulation of Two-Dimensional Materials

Lawrence Hudy
University of Wisconsin-Milwaukee

SYNTHESIS, CHARACTERIZATION, AND SIMULATION OF TWO-DIMENSIONAL MATERIALS

by

Lawrence Hudy

A Dissertation Submitted in

Partial Fulfillment of the

Requirements for the Degree of

Doctor of Philosophy

in Physics

at

The University of Wisconsin-Milwaukee

August 2023

ABSTRACT

SYNTHESIS, CHARACTERIZATION, AND SIMULATION OF TWO-DIMENSIONAL MATERIALS

by

Lawrence Hudy

The University of Wisconsin-Milwaukee, 2023
Under the Supervision of Professor Michael Weinert

This dissertation focuses on my journey through many aspects of surface science leading to the first principles investigation of transition metal dichalcogenides studying the impact of defects, twist, and decreasing interlayer separation to probe their effect on the electronic properties of these materials. My journey started out learning many aspects of material science such as methods for material synthesis and characterization but later ended on simulation of material properties using density functional theory.

In the first experiments, we focus on two-dimensional material synthesis, mostly involving graphene, where we see that polymer transferred graphene forms a Schottky junction when interfaced with a semiconductor. From atomic force microscopy and scanning tunneling microscopy we see that polymer transferred graphene is not entirely flat and forms ripples and ridges on the surface. Scanning tunneling spectroscopy and temperature dependent current-voltage measurements help to show that the behavior of these graphene Schottky diodes are not ideal. The observed temperature dependent Schottky barrier height can be explained using a distribution of barriers with varying barrier heights.

The theoretical studies focus on various transition metal dichalcogenides, composed of $MoSe_2$ and WSe_2, using their monolayer and their homo and hetero bilayer counterparts. The

first studies observed that adding defects alters the electronic band structure, and in particular, a copper dopant creates impurity states at the Fermi level and induces a significant magnetic moment in the material. The resulting occupied unpaired spin states are the key contributor to the creation of the magnetic moment in this material. Next, we see that twisted bilayer transition metal dichalcogenides, specifically bilayers composed of $MoSe_2$ and WSe_2, where we observe pressure induced flat bands and real space localization. Using a commensurate set of twist angles and varying interlayer spacing led to the discovery of flat bands and real space localization. These flat bands are a result of forcing the bilayers to interact causing a localization in real space. It is only under special conditions where the closest chalcogens, along with the nearest metal atoms, form a hybridized state that contribute to the flat bands in the energy band diagram. These findings help to highlight the impact impurities can have on transition metal dichalcogenides and the role of twist and interlayer separation has on the formation of flat bands as well as real space localization in these materials.

I dedicate this dissertation to my supporting wife and our children.

TABLE OF CONTENTS

LIST OF FIGURES

LIST OF TABLES

LIST OF ABBREVIATIONS

AFM	Atomic force microscope/microscopy
ARPES	Angle resolved photoemission spectroscopy
Bi_2Se_3	Bismuth Selenide
BZ	Brillouin zone
CMOS	Conventional metal oxide semiconductor
CVD	Chemical vapor deposition
DFT	Density functional theory
DI	Deionized
dI/dV	Differential conductance
DOS	Density of states
FeSe	Iron Selenide
FET	Field effect transistor
GaAs	Gallium Arsenide
GEA	Gradient expansion approximation
GGA	Generalized gradient approximation
GPIB	General purpose interface bus
IV	Current-voltage
LCAO	Linear combination of atomic orbitals
LDA	Local density approximation
LED	Light emitting diode
MBE	Molecular beam epitaxy
MoS_2	Molybdenum disulfide
$MoSe_2$	Molybdenum diselenide
NaOH	Sodium Hydroxide
PAW	Projected augmented wave
PBE	Perdew, Burke, and Ernzerhof
PDOS	Partial density of states
PMMA	Polymethyl methacrylate
RPA	Random phase approximation
rpm	Revolutions per minute
Si	Silicon
SiC	Silicon Carbide
SiO_2	Silicon Dioxide
SOC	Spin-orbit coupling
STM	Scanning tunneling microscope/microscopy
STO	Strontium Titanate
STS	Scanning tunneling spectroscopy
TMD	Transition Metal Dichalcogenide
UHV	Ultra-high vacuum
VASP	Vienna Ab initio simulation package
vDW	van der Waals
WSe_2	Tungsten diselenide

μ_B	Bohr magneton

ACKNOWLEDGEMENTS

There have been many people that have helped me on my journey to completing my PhD. I would like to first thank Dr. Lian Li for his support and encouragement in my experimental studies. I would also like to thank Dr. Michael Weinert for helping me complete the last leg of my PhD after I took some time off. I would like to thank his patience in helping me work through concepts and helping me shape this dissertation. I am also thankful for his commitment to help me complete this dissertation.

I would also like to express my gratitude to my other committee members, Dr. Daniel Agterberg, Dr. Ionel Popa, Dr. Min Gyu Kim, and Dr. Peter Schwander for supporting me during my studies.

I would like to express my thanks to the other graduate students and post docs that I encountered along the way; Dr. Shivani Rajput, Dr. Dushyant Tomer, Dr. Zhuozhi Ge, Rusty Mundorf, Xi Dong, and Dr. Danylo Radevych. They made the difficult times easier through their friendships along the way.

I am also grateful for all the UWM's resources that helped me throughout this journey. This ranges from custom parts made in the machine shop, surface science equipment, to the computational tools available through the High-Performance Computing resources.

Last but surely not least, I would like to thank my loving and supporting wife. She has been with me throughout all my struggles, in school and out, as we began building our life and family together. It is with her support that I am able to complete this dissertation.

Chapter One Introduction and Motivation

1.1 Overview

Modern society and its thirst for a technology driven lifestyle has put a high demand on smaller and more powerful semiconducting devices. Current computational technology is based on silicon because it is readily available based on current processing techniques, it is resistant to very high temperatures and high currents [1]. Silicon also requires low voltages for operation and can be easily doped to tailor its characteristics [2]. There are physical limitations to shrinking conventional metal on semiconductor (CMOS) devices based on silicon in order to create more computational dense chips. These limitations have fueled research on new devices that could possibly replace standard silicon CMOS technology. One approach would be to investigate systems where the dimensionality is reduced, that is, as we constrain a dimension, we can see what possible physical characteristics we can exploit into a mechanism which can be used as an on/off switch for a logical device. A natural extension would be to go from 3-dimensional space to two-dimensional space and this is where layered van der Waals (vDW) systems come into play. A single layer is the two-dimensional physical limit where the material's thickness can be of a single atom. Graphene is a good example of a single atom layer thick material.

Since the discovery of graphene's properties by Novoselov et al. in 2004, there has been great interest in graphene and two-dimensional material systems [3]. Two dimensional materials have displayed numerous interesting properties such as spintronics, charge density waves, superconductivity, electron correlations, as well as, but not limited to, topological

effects [4-11]. These two-dimensional materials can be fabricated in many ways such as the simple and effective technique of mechanical exfoliation also known as the “Scotch” tape method [3]. This is achievable because the bulk material is made up of layers of two-dimensional sheets that are weakly bounded by vdW forces. This architecture also allows us an opportunity to engineer new materials by stacking different types of layers. Not only can we stack different layers, but we can also rotate the layers with respect to each other to achieve other desired effects. This twisting produces an interference pattern, called a Moiré pattern, in the material which also gives rise to new and exciting properties. This gives us many knobs to turn in terms of functionalizing performance out of these stacked layered material systems.

Generally, two-dimensional materials fall into 4 families of materials. Graphene and its analogues like hexagonal boron nitride, black phosphorous analogues, III-VI semiconductors, and transition metal dichalcogenides (TMDs). These materials span a variety of electronic property types such as insulators, semiconductors, semimetals, metals, and superconductors [12]. Those also produce a variety of effects that can be used to create new novel devices such as spintronics or valleytronics [4,5].

1.2 Graphene

Graphene, the prototypical two-dimensional material, has shown great promise because of its unique band structure [14]. Graphene gets its unique band structure from the equivalent carbon sublattices, A and B in the honeycomb lattice. This is a result of the fact that the irreducible representation is 2-fold degenerate. Using conventional tight-binding theory, where the first nearest neighbor hoping is primarily considered leads to the linear energy dispersion relation at the corners of the hexagonal Brillouin zone (BZ) near the fermi level [13]. Since the

energy dispersion is linear at these high symmetry points, the charge carriers behave more like relativistic particles that obey the Dirac equation [14]. The band gap for graphene is 0 eV and the fermi level also lies at this point making graphene a semimetal [13,14]. It hosts many exotic properties such as relativistic carriers, high thermal and electrical conductivities, topological effects, and, but not limited to, unconventional superconductivity [3,8,10,15-17]. More recently small angle twisted bilayer graphene, or commonly referred to as "magic angle" twisted bilayer graphene, has shown flat electronic bands and unconventional superconductivity, which has been attributed to the strongly correlated electrons [8]. This has inspired research into other twisted bilayer material systems.

1.3 Transition Metal Dichalcogenides

Transition metal dichalcogenides are composed of a transition metal atom like Molybdenum, M = Mo, and a chalcogen ion like Sulfur, X = S and are chemically designated as MX_2. These materials are similar to graphene in that they can be cleaved into a single layer except where graphene is one atomic layer TMDs consists of a metal layer sandwiched between the two chalcogen layers. These materials are typically semiconducting and have a non-zero band gap, 0-2 eV, where spin orbit coupling (SOC) plays an important role in their band structures [18-21]. For systems without inversion symmetry but still have time reversal symmetry, the effect of SOC lifts the degeneracy for the valleys at K and K' because they no longer correspond to time reversal invariant momenta [18]. The valence and conduction band valleys split into two spin polarized bands because time reversal symmetry requires that the spin and momentum degrees of freedom to be coupled to the symmetry points at K and K' [18]. This means that at those high symmetry points the charge carriers have opposite spin

polarizations. Many TMDs have an indirect band gap in their bulk form meaning that additional crystal momentum is required to go from the valence band maximum to the conduction band minimum. The band gap transitions from indirect to direct as we move from the bulk systems towards the monolayer systems [18].

1.4 Twisted Transition Metal Dichalcogenides

A natural extension from twisted bilayer graphene would be to investigate twisted bilayer TMDs. There are many possibilities, such as combinations of atoms or twist angles, when it comes to creating twisted transition metal dichalcogenides. The layers can be of the same species or of differing species, homo or hetero bilayers. These quantities can be used to functionalize the material in order to yield desirable responses. The twisting of the layers changes the interaction between the layers which impacts the orbital interaction, charge density, energy bands, and excitons. Under special conditions, these twisted vDW materials have displayed flat bands, correlation effects, trapped excitons from the Moiré potential, inter and intra layer excitons, as well as many other interesting effects [22-27].

This dissertation explores both experimental and theoretical methods used to test these thin film systems. First is the discussion of methods used to create and characterize samples of graphene and TMDs. Then there is the theoretical exploration of TMDs with defects as well as twisted TMDs using first principles calculations and their impact on the electronic properties of the TMDs. Lastly, is the outlook on the results of this study as well as possible paths forward.

1.5 Thesis Outline

Chapter 2

This chapter outlines the methods used in this dissertation to create, characterize, and also predict the properties of thin film samples. This covers material synthesis using polymer-based transfer method and molecular beam epitaxy. It also covers characterizations methods such as atomic force microscopy, Raman spectroscopy, scanning tunneling microscopy, scanning tunneling spectroscopy, as well as electronic transport measurements. This chapter also includes information on a custom built chamber used to perform temperature dependent current-voltage measurements. The predictive methods that are covered in this chapter are density functional theory and the tight binding method. This chapter lays the ground work for interpreting the results of the following chapters. Overall, these are the tools used to make, characterize, and predict the properties of thin film systems.

Chapter 3

This chapter discusses graphene including its crystal structure and its properties. It also covers studies done on polymer transferred graphene onto a semiconducting substrate forming a Schottky junction. This Schottky diode shows non-ideal performance by the temperature variation of the Schottky barrier height. This variation in the barrier height is modeled by a gaussian distribution of barriers because the interface between graphene and the semiconducting material is not inherently uniform.

Chapter 4

This chapter covers transition metal dichalcogenides including their crystal structure and their respective properties. It also covers the effect of doping the transition metal dichalcogenides with manganese, iron, and copper. Interestingly we find that the copper

doped systems display an induced magnetic moment and a non-zero off-diagonal component to the optical response.

Chapter 5

This chapter covers twisted transition metal dichalcogenides including their crystal structure, properties, and current findings from my investigation. We compressed the twisted bilayers to find the emergence of flat bands states in the band structure and localized states in the simulated scanning tunneling microscopy imagery. Defects were also introduced into these twisted bilayer systems which results in the reduction of effects the dopants, reduced magnetic moments, and the features from the twist bilayers get washed out by the defects, real space localization is dominated by added defect.

Chapter 6

This last chapter discusses the findings in this dissertation, their impact, as well as outlook on future studies.

References

1. Guisinger, N. P., Arnold, M. S., & Guest Authors. (2010). Beyond Silicon: Carbon-Based Nanotechnology. *MRS BULLETIN*, 273-276.
2. Neamen, D. A. (2003). *Semiconductor Physics and Devices: Basic Principles.* New York: McGraw-Hill.
3. Novoselov, K. S., Geim, A. K., Morozov, S. V., Jiang, D., Zhang, Y., Dubonos, S. V., & Firsov, A. A. (2004). Electric Field Effect in Atomically Thin Carbon Films. *Science, 306*(5696), 666-669. doi:10.1126/science.1102896
4. Han, W., Kawakami, R. K., Gmitra, M., & Fabian, J. (2014). Graphene spintronics. *Nature Nanotechnology*, 794-807.
5. Schaibley, J. R., Yu, H., Clark, G., Rivera, P., Ross, J. S., Seyler, K. L., Wang, Y., & Xu, X. (2016). Valleytronics in 2D materials. *Nature Reviews Materials, 1*, 1-15. doi:10.1038/natrevmats.2016.55
6. Wilson, J. A., Di Salvo, F. J., & Mahajan, S. (1973). Charge-Density Waves in Metallic, Layered, Transition-Metal Dichalcogenides. *Physical Review Letters*, 882-885.
7. Feng, H., Xu, Z., Zhuang, J., Wang, L., Liu, Y., Xu, X., Song, L., Hao, W., & Du, Y. (2019). Role of Charge Density Wave in Monatomic Assembly in Transition Metal Dichalcogenides. *Advanced Functional Materials, 29*(15), 1-7. doi: 10.1002/adfm.201900367
8. Cao, Y., Fatemi, V., Fang, S., Watanabe, K., Taniguchi, T., Kaxiras, E., & Jarillo-Herrero, P. (2018). Unconventional superconductivity in magic-angle graphene superlattices. *Nature, 556*, 43-50. doi:10.1038/nature26160
9. Xie, Y., Lian, B., Jäck, B., Liu, X., Chiu, C.-L., Watanabe, K., Taniguchi, T., Bernevig, B. A., & Yazdani, A. (2019). Spectroscopic signatures of many-body correlations in magic-angle twisted bilayer graphene. *Nature, 572*, 101-105. doi:https://doi.org/10.1038/s41586-019-1422-x
10. Kane, C. L., & Mele, E. J. (2005). Quantum Spin Hall Effect in Graphene. *Physical Review Letters, 95*, 1--4. doi:https://doi.org/10.1103/PhysRevLett.95.226801
11. Qian, X., Liu, J., Fu, L., & Li, J. (2014). Quantum spin Hall effect in two-dimensional transition metal dichalcogenides. *Science, 346*(6215), 1344-1347. doi:10.1126/science.1256815
12. Ajayan, P., Kim, P., & Banerjee, K. (2016). Two-dimensional van der Waals materials. *Physics Today, 69*(9), 38-44. doi:https://doi.org/10.1063/PT.3.3297
13. Wallace, P. R. (1947). The Band Theory of Graphite. *Physical Review, 71*(9), 622-634. doi:https://doi.org/10.1103/PhysRev.71.622
14. Castro Neto, A. H., Guinea, F., Peres, N. M., Novoselov, K. S., & Geim, A. K. (2009). The electronic properties of graphene. *Reviews of Modern Physics, 81*, 109-162. doi:10.1103/RevModPhys.81.109
15. Novoselov, K. S., Geim, A. K., Morozov, S. V., Jiang, D., Katsnelson, M. I., Grigorieva, I. V., Dubonos, S. V., & Firsov, A. A. (2005). Two-dimensional gas of massless Dirac fermions in graphene. *Nature, 438*, 197-200. doi:10.1038/nature0423
16. Balandin, A. A., Ghosh, S., Bao, W., Calizo, I., Teweldebrhan, D., Miao, F., & Lau, C. (2008). Superior Thermal Conductivity of Single-Layer Graphene. *Nano Letters, 8*, 902-907. doi:https://doi.org/10.1021/nl0731872

17. Petrone, N., Dean, C. R., Meric, I., van der Zande, A. M., Huang, P. Y., Wang, L., Muller, D., Shepard, K.L., & Hone, J. (2011). Chemical Vapor Deposition-Derived Graphene with Electrical Performance of Exfoliated Graphene. *Nano Letters*, 2751-2756. doi:10.1021/nl204481s
18. Manzeli, S., Ovchinnikov, D., Pasquier, D., Yazyev, O. V., & Kis, A. (2017). 2D transition metal dichalcogenides. *Nature Reviews Materials, 2*, 1-15. doi:10.1038/natrevmats.2017.33
19. Zhu, Z. Y., Cheng, Y. C., & Schwingenschlögl, U. (2011). Giant spin-orbit-induced spin splitting in two-dimensional transition-metal dichalcogenide semiconductors. *Physical Review B, 84*, 1-5. doi:10.1103/PhysRevB.84.153402
20. Xiao, D., Liu, G.-B., Feng, W., Xu, X., & Yao, W. (2012). Coupled Spin and Valley Physics in Monolayers of MoS2 and Other Group-VI Dichalcogenides. *Physical Review Letters, 108*, 1-5. doi:10.1103/PhysRevLett.108.196802
21. Liu, G.-B., Shan, W.-Y., Yao, Y., Yao, W., & Xiao, D. (2013). Three-band tight-binding model for monolayers of group-VIB transition metal dichalcogenides. *Physical Review B, 88*, 1-10. doi:10.1103/PhysRevB.88.085433
22. Zhang, Z., Wang, Y., Watanabe, K., Taniguchi, T., Ueno, K., Tutuc, E., & LeRoy, B. J. (2020). Flat bands in twisted bilayer transition metal dichalcogenides. *Nature Physics, 16*, 1093-1096. doi:https://doi.org/10.1038/s41567-020-0958-x
23. Wang, L., Shih, E.-M., Ghiotto, A., Xian, L., Rhodes, D. A., Tan, C., . . . Dean, C. R. (2020). Correlated electronic phases in twisted bilayer transition metal dichalcogenides. *Nature Materials, 19*, 861-866. doi:https://doi.org/10.1038/s41563-020-0708-6
24. Shabani, S., Halbertal, D., Wu, W., Chen, M., Liu, S., Hone, J., . . . Pasupathy, A. N. (2021). Deep moiré potentials in twisted transition metal dichalcogenide bilayers. *Nature Physics, 17*, 720-725. doi:https://doi.org/10.1038/s41567-021-01174-7
25. Tran, K., Moody, G., Wu, F., Lu, X., Choi, J., Kim, K., . . . Li, X. (2019). Evidence for moiré excitons in van der Waals heterostructures. *Nature, 567*, 71-75. doi:https://doi.org/10.1038/s41586-019-0975-z
26. Choi, J., Hsu, W.-T., Lu, L.-S., Sun, L., Cheng, H.-Y., Lee, M.-H., . . . Chang, W.-H. (2020). Moiré potential impedes interlayer exciton diffusion in van der Waals heterostructures. *Science Advances, 6*, 1-6. doi:10.1126/sciadv.aba8866
27. Regan, E. C., Wang, D., Jin, C., Utama, M. I., Gao, B., Wei, X., . . . Wang, F. (2020). Mott and generalized Wigner crystal states in WSe2/WS2 moiré superlattices. *Nature, 579*, 359-363. doi:https://doi.org/10.1038/s41586-020-2092-4

Chapter Two Methodology

2.1 Introduction

This chapter covers the methods we use to create two-dimensional samples, methods used to characterize those samples, as well as theoretical methods used to predict properties of those samples. Typical methods used to create monolayer or few layer samples are mechanical exfoliation, chemical vapor deposition (CVD), and molecular beam epitaxy (MBE). Methods used to characterize these samples are either used to image the surface of the sample such as atomic force microscopy (AFM) and scanning tunneling microscopy (STM) or they probe the sample to understand its physical properties such as Raman Spectroscopy, scanning tunneling spectroscopy (STS), and charge carrier transport measurements. There are other methods used to probe sample information but are not the focus of this dissertation such as optical microscopy, ellipsometry, x-ray photoelectron spectroscopy, angle-resolved photoemission spectroscopy, etc.

2.2 Material Synthesis

Two dimensional materials can be synthesized in many ways, some are most definitely easier than others. Methods we used for two-dimensional material synthesis covered in this dissertation include mechanical exfoliation or the Scotch tape method [1,2], polymer-based transfer [3], and molecular beam epitaxy [4,5]. Methods like mechanical exfoliation and the polymer-based transfer are fast and simple but provide little control on sample creation. Chemical vapor deposition and molecular beam epitaxy allow much more control over the growth conditions allowing a user to fine tune sample creation. Most of our high-quality thin

films are made using molecular beam epitaxy because it provides the ultimate control in terms of quality and repeatability.

2.2.1 Polymer Transfer Method

The polymer transfer method is a technique that uses a polymer backing layer to transfer a two-dimensional material, like graphene, onto an arbitrary surface [3]. The graphene samples we used were monolayer graphene on copper made using chemical vapor deposition. These samples are readily available and can be bought from many material providers. Figure 2.1 is a simple diagram of the polymer transfer process we used to transfer graphene onto any arbitrary substrate.

The following outlines our polymer-based transfer method. First, a polymethyl methacrylate (PMMA) polymer is spin coated at a rate of 3000 rpm for 45 seconds to create a uniform layer that is approximately 300 nm thick. The polymer coated sample is then heated on a hot plate at 135 °C for 10 minutes to cure. Then the sample is placed in a copper etch solution of iron chloride ($FeCl_3$) to remove the copper backing layer. The sample is then transferred to multiple deionized (DI) water baths in order to remove any residual particles. To further clean the sample, it is placed into an RCA solution (1:1:10 HCL/H_2O_2/H_2O) for 15 minutes at room temperature and subsequently rinsed in DI a few more times. The sample is then scooped out of the DI water and placed on an arbitrary surface. To promote adhesion to the substrate, the sample is spun at 1000 rpm for 90 seconds. Then the sample is heated at 135 °C for 10 minutes to further promote adhesion and remove any residual liquid. Lastly, the topcoat polymer is removed using solvents like acetone. Figure 2.9 is a picture of an AFM

image of PMMA transferred graphene where you can see the ridges of monolayer graphene on SiO_2.

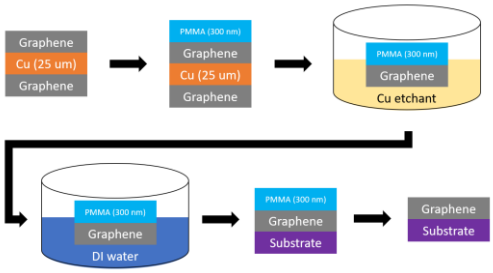

Figure 2.1: Diagram of the polymer transfer process for graphene

2.2.2 Ultrahigh Vacuum Systems

In order to grow high quality films, it is critical to prevent the films from exposure to contaminants during and after film growth. Thin films grown using molecular beam epitaxy require an ultra-high vacuum (UHV) system that removes all the contaminants from the atmosphere and allows only the sources to interact with the surface of the substrate to grow a sample. The main contaminants in a UHV system are gases from the atmosphere, water vapor which is mostly absorbed on the interior surface of the UHV chamber, and the other materials within the UHV chamber. Most of the materials within a UHV chamber have low vapor pressure at room temperature and do not impact the level of vacuum in a UHV system.

UHV systems pump air out of the chambers using a variety of pumps. The variety of pumps that are employed usually determines the level of vacuum that can be achieved in the UHV chamber. Initially a mechanical pump, also known as a positive displacement pump, is used to pump the system down to approximately 10^{-4} Torr. Figure 2.2 a) and b) displays a typical mechanical pump we used along with its cross section as well as the cycle it goes through in order to evacuate air out of the chamber. This is done by moving gas from a low-

pressure region to a high-pressure region through compression of the gas and subsequent exhaustion to the atmosphere. The next stage employs a turbomolecular pump that uses spinning blades to transfer momentum to the remaining gas molecules and can achieve a pressure from 10^{-4} to 10^{-12} Torr. Figure 2.3 displays a turbo pump and its cross section for its function. After the initial pump down the UHV chamber is baked at 100 °C in order to remove all the water vapor from the chamber. These are the typical components needed to achieve ultra-high vacuum for high quality crystal growth.

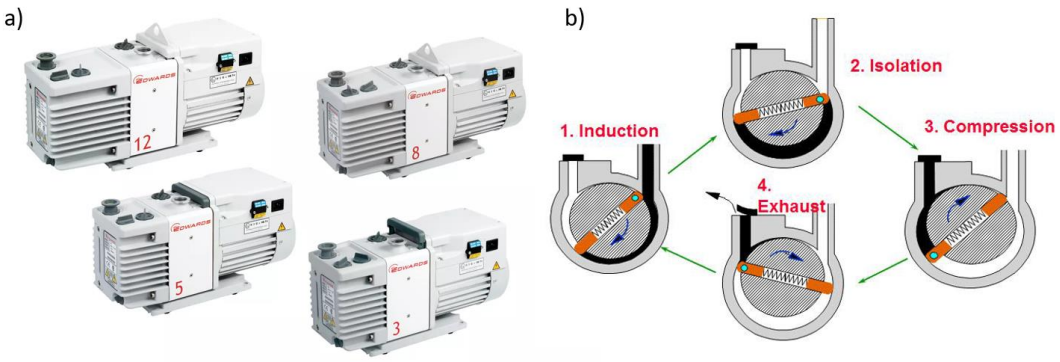

Figure 2.2. Rotary vane mechanical pumps. a) Edwards rotary vane mechanical pumps [6]. b) Rotary vane cycle [7]

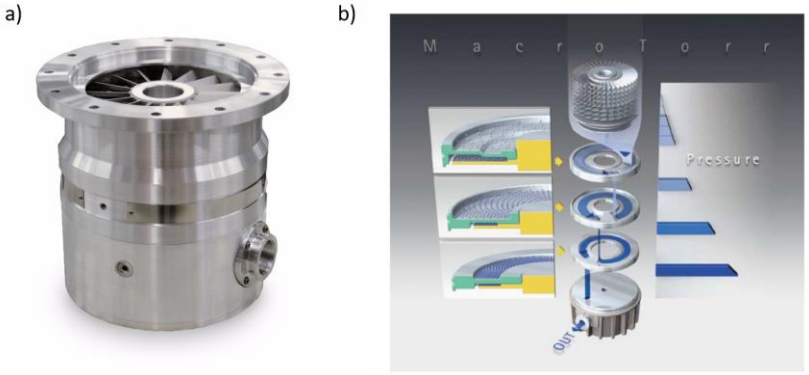

Figure 2.3. Turbomolecular pump and operation. a) turbomolecular pump [8]. b) exploded view of a turbomolecular pump. Also contains cartoon drawing of operation to help show the various stages of the stators in the turbo pump [8].

2.2.3 Molecular Beam Epitaxy

Molecular beam epitaxy is the well-controlled thin film growth method we used to create layer by layer growth for various materials. This allowed us to create high quality, single crystal epitaxial thin films. Quality MBE films require UHV chambers to grow high-quality samples. The main components required for an MBE chamber are the components required for UHV conditions, the platform for heating the substrate, and material sources such as effusion or electron beam sources. There are different ideal growth conditions based on the growth materials and the substrate they want to grow their materials on. This requires preparing a substrate by annealing at high temperatures. This allows the atoms to diffuse on the surface leading to a low energy minimum configuration which commonly ends up being step-flow growth where flat terrace and steps will propagate across the surface of the sample. Some of this step-flow growth by annealing at high temperature can be seen in the AFM image of Strontium Titanate (STO) in Figure 2.10.

We typically used silicon carbide (SiC) as a test substrate. Samples of 6H-Si-SiC and 4H-C-SiC were used to test thin film growth parameters before using the desired substrate. SiC can be heated to release the silicon leaving flat layers of epitaxial graphene for films to grow on. Samples of SiC are useful for determining initial growth conditions given that bad films can be baked off and the growth conditions can be reset. A simple method used for heating samples is by passing current through the conducting substrate. SiC is a good candidate because it is semiconducting and can withstand high temperatures. Heating of the samples provides the benefit of giving absorbed atoms mobility to diffuse on the surface and find other atoms to begin film growth as well as burning off poor films. Non conducting samples can be used as well

but they either need to be stacked on a conducting sample or heated by another method such as electron beam heating. In electron beam heating, the metallic holder can be used as an electrode placing a bias between the sample and electron beam source, such as a wound wire filament. The bias potential provides the thermionic electrons with kinetic energy. As the electrons strike the surface of the other electrode, their kinetic energy gets converted into thermal energy thus heating the sample surface. Figure 2.4 a) show the sample holder that was made from ceramic material to isolate the contacts from electricity and help isolate the temperature of the sample holder. Figure 2.4 b) shows the glowing orange sample being heated by electron bombardment from the filament pictured in Figure 2.4 a). Figure 2.10 a) is an AFM image of annealed strontium titanate that was annealed using electron beam heating. Figure 2.10 b) shows the line profile of the well-defined steps.

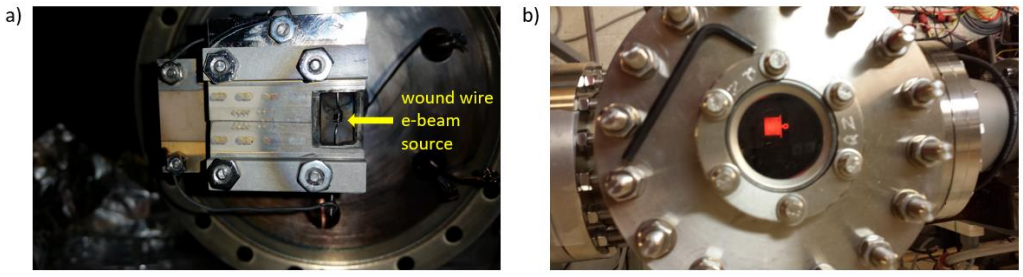

Figure 2.4. Sample heating apparatus. a) electron beam heating stage b) sample holder heated using electron beam heating.

Material deposition is done by heating samples of elements to cause them to melt and evaporate. The materials used for deposition need to be of high purity to ensure quality crystalline growth. The UHV system provides an environment where the mean free path of the gas flux is larger than the UHV chamber, meaning that the gas molecules do not interact with each other in flight but rather interact with each other on the surface with which they are absorbed on. The heating of these elemental sources is typically done using Knudsen cells or

electron beam evaporators. Figure 2.5 a) shows a Knudsen cell evaporator and Figure 2.5 b) is a picture of a 4-source electron beam evaporator that were used in the lab. A bias potential between the filament and the source, or container, provides the mechanism for the thermionic electrons to bombard the sources as the current flows through the filament. The rate of evaporation can be controlled by the bias voltage or the amount current running through the filament. Typical growth rates are very slow to allow films to grow epitaxially, meaning they grow in a well-defined orientation typically sharing in plane lattice constants for similar crystalline structures.

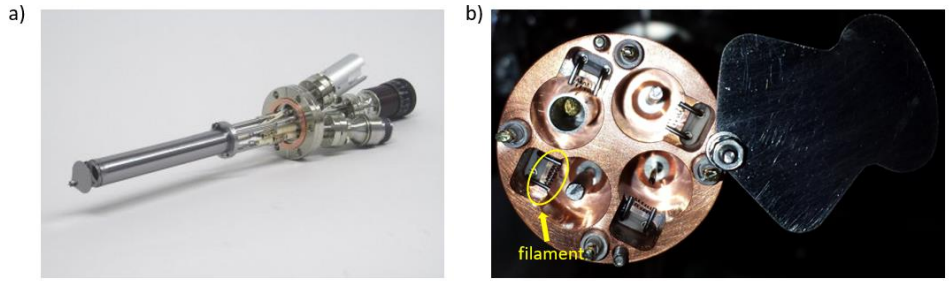

Figure 2.5. Molecular beam sources. a) sample Knudsen cell from Scienta Omicron [9] b) 4 source electron beam evaporator from Mantis Deposition

2.2.4 Photolithography

A common method used in electronic device fabrication is photolithography. Photolithography uses chemicals that harden when exposed to ultraviolet radiation to create patterns on a material or substrate. You can stack these patterns to create different types of devices. The process varies based on the chemicals you use but the generic process is as follows [10]. Step 1 is substrate preparation. In this step the key component is to remove contaminants from the surface using chemicals, etching, or high temperature. Step 2 typically includes growing a thing film of the prepared substrate. These steps are outlined in the process of creating samples using a technique like molecular beam epitaxy. Step 3 involves spin coating

a photosensitive chemical to provide a coating on our prepared sample. This is then subsequently baked to stiffen the photosensitive material. Step 4 is the alignment of the shadow mask and the sample. The sample and shadow mask are placed in a holder and subsequently aligned to create a predesigned pattern based on the device's application. Step 5 is when the sample is exposed to ultraviolet radiation. Step 6 is when the sample is placed in a vacuum chamber with an electron beam evaporator that will deposit either a dielectric film or metal layer. Step 7 involves treating the sample to chemicals to remove the undeveloped photoresist material and dielectric or metal that was deposited in the electron beam evaporation chamber. Some of the previous steps can be repeated to create stacks of dielectric material or metal based on the device design. Figure 2.6 is a pictorial description of the photolithography process used to create electronic devices.

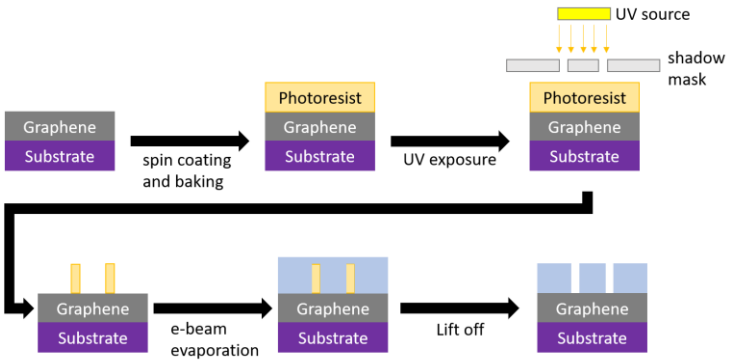

Figure 2.6. Schematic diagram of the photolithography process used to create electronic devices.

A typical device that is used to measure the current-voltage (IV) characteristics of a material is a Hall bar sample. We constructed Hall bars by using the photolithography process outlined in the previous section. These Hall bars help to determine the conductivity of a sample as well as the type of carriers using IV measurements under a magnetic field. Figure 2.7 shows a set of Hall bars of Bi_2Se_3 on sapphire used for conductivity measurements. Contacts are made

from the large metal pads on the sample to the metal contacts on the chip carrier. The contacts from the chip carrier to the pads of the Hall bar are made by a gold wire ball bonding machine. This machine has parameters that can tune the heat of the sample, mostly to promote adhesion, as well as the pressure and time the tip contacts the surface. The larger pads on the chip carrier make it easier to make electrical connections to other devices that can perform the IV characteristics of the sample.

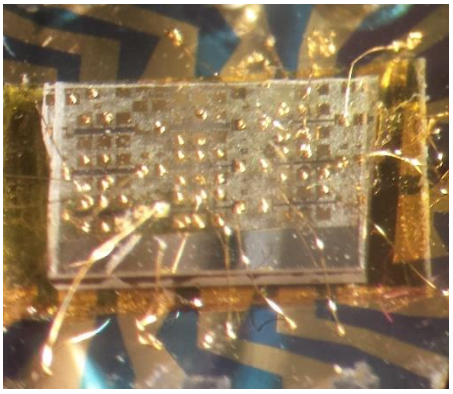

Figure 2.7. Samples of Bi_2Se_3 on sapphire that were created using photolithography.

2.3 Material Characterization

Thin films can be characterized by many methods which probe their structural, mechanical, and electrical properties. The two main methods we use for characterization are various types of microscopies and spectroscopies. There are also other macroscopic types of testing that can probe properties of materials such as mechanical or electrical types of testing. Electrical testing plays a key role in characterizing new materials that could use a different type of mechanism which could be the basis of a new and emerging technology. The electrical testing we utilize is the current-voltage measurements to help investigate the properties of our samples.

2.3.1 Atomic Force Microscopy

Atomic force microscopy is a scanning probe technique used to probe the surface of a material and extract its surface topography and force interactions, as well as material manipulation. The typical set up of an atomic force microscope consists of a cantilever, piezoelectric element for oscillating the cantilever, or tip, system to detect the deflection of the cantilever, and an xyz stage to move the sample or the cantilever set up. Figure 2.8 a) pictures an atomic force microscope from Agilent, similar to the one we used in our lab, and b) is the key components for an atomic force microscope. This technique shares similarities with scanning tunneling microscopy except that the sample being imaged does not need to be conducting. Instead, the atomic forces between the tip and the sample are mapped to provide an image of the surface. These forces are measured indirectly using the deflection of the cantilever which is typically monitored by a laser. Figure 2.9 is a sample of polymer transferred graphene onto SiO_2. The image verifies that the sample of graphene was transferred onto the SiO_2 substate. There are also clearly ridges of the graphene film formed through the polymer transfer process. Figure 2.10 a) is a sample of annealed STO imaged using atomic force microscopy. The AFM image shows well defined steps that were created from the annealing process. Figure 2.10 b) is a line profile across these steps showing the deflection of the tip and the flat surface of each of these steps. Atomic force microscopy makes it simple to verify various steps in a sample or device making process.

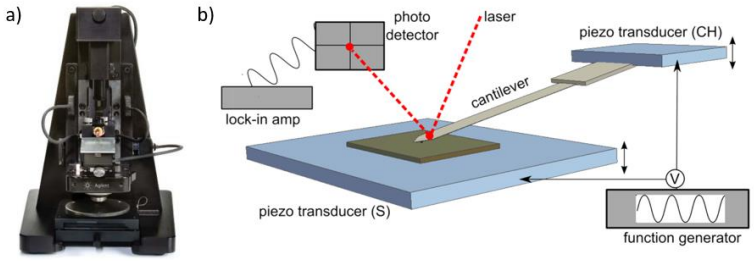

Figure 2.8. Atomic force microscope overview. a) Agilent atomic force microscope [11] b) key components in the operation of an AFM [12]

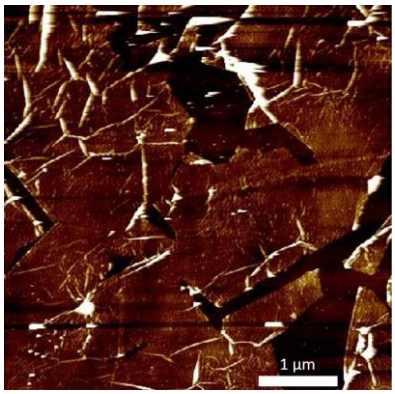

Figure 2.9: Atomic force microscopy image of polymer transferred graphene onto SiO_2.

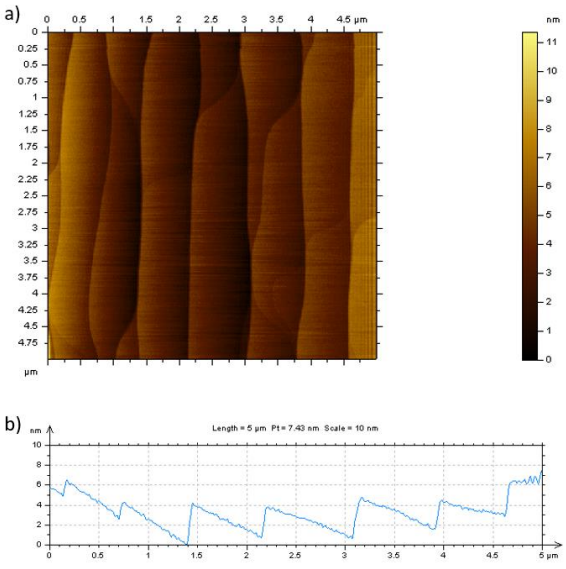

Figure 2.10. Atomic force microscopy image of annealed STO.

2.3.2 Raman Spectroscopy

Raman spectroscopy is a non-destructive technique used to determine the chemical structure of a material. A monochromatic laser is used to excite the vibrational modes within the material. Most of the scattered light will be of the same wavelength as the source, known as Rayleigh scattering, but there will also be other scattered wavelengths, either shifted up or down, based on the chemical structure of the material. This Raman spectrum will have several peaks that correspond to specific molecular vibrations within the material. We use this technique to determine if monolayer graphene was present within our test samples that do not have good contrast and can't be seen with an optical microscope. Figure 2.11 a) is a Raman spectrum of transferred monolayer graphene onto SiO_2/Si. The more intense G, 1520-1640 cm^{-1}, and 2D, 2600-2750 cm^{-1}, peaks are signatures of monolayer graphene [13]. The G peak is a symmetric E_{2g} vibrational mode that corresponds to the top and bottom parts of the hexagon moving outward and the middle points moving inward as pictured in Figure 2.11 d). The D peak corresponds to the A_{1g} symmetric vibrational mode where all the atoms located at the hexagon move outwardly as seen in Figure 2.11 e). Raman spectroscopy allows us to indirectly gain useful chemical and structural information from newly made samples and help verify steps in the sample making process.

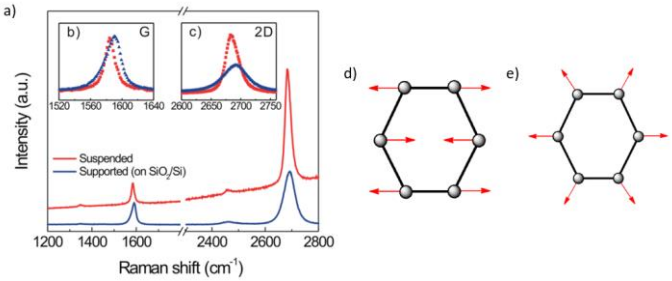

Figure 2.11. Raman spectroscopy overview of graphene. a) Raman spectra of monolayer graphene on SiO_2/Si and perforated silicon nitride using

514 nm laser adapted from Suk et al [13] b) G peak (1520-1640 cm^{-1}) c) 2D peak (2600-2750 cm^{-1}) d) E_{2g} vibrational mode e) A_{1g} vibrational mode.

2.3.3 Scanning Tunneling Microscopy

Scanning tunneling microscopy is another scanning probe technique that uses a metal tip over a conducting sample along with a feedback loop to provide an image of the surface. A typical scanning tunneling microscope consists of a metal tip, piezoelectric element to control the tip, and electronics to monitor and control the feedback loop which is depicted in Figure 2.12. Scanning tunneling microscopes relies on the quantum mechanical effect of tunneling to image the sample's surface. The electrons have to overcome the potential barrier between the sample and the tip. Using a simple 1-dimensional model, we can write the solution to the Schrödinger equation, where the energy is less than the potential barrier, as $\psi(z) = \psi(0)exp(\pm\kappa z)$ where $\kappa = \frac{\sqrt{2m(U-E)}}{\hbar}$. The probability that the electron tunnels through the barrier is proportional to $|\psi(z)|^2 = |\psi(0)|^2 exp(\pm 2\kappa z)$. We can see from this relation that the tunneling current has an exponential relationship with the tip to sample distance which allows STM imaging to produce such high resolution STM imagery. The tunneling current feedback loop can maintain a current set point by altering the location of the tip which then can be mapped to the topography of the sample. Figure 2.13 shows the rectangular island growth of Iron Selenide (FeSe) on epitaxial graphene/SiC. Figure 2.10 shows the annealed surface of Strontium Titanate (STO) where we can see the well-defined flat ridges. This provides an ideal surface for films to grow to because it is flat. Figure 2.14 is an STM image of FeSe growth on STO. You can see the layer-by-layer growth as well as the excess Fe on the surfaces of each layer meaning that the flux of Fe is too high.

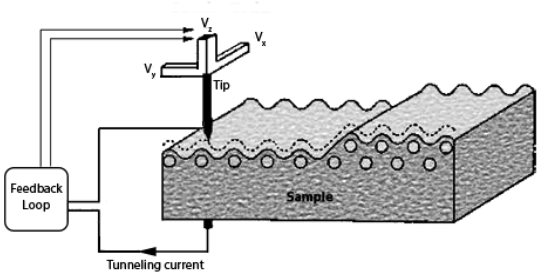

Figure 2.12. Model of the key components in a scanning tunneling microscope [14].

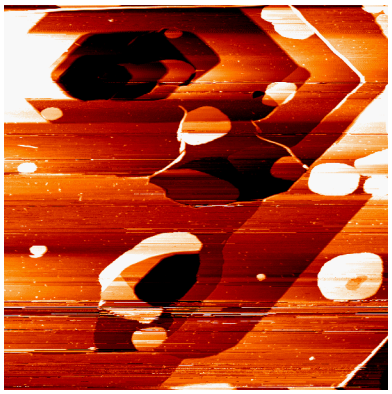

Figure 2.13. Scanning tunneling microscopy image of FeSe growth on epitaxial graphene/SiC.

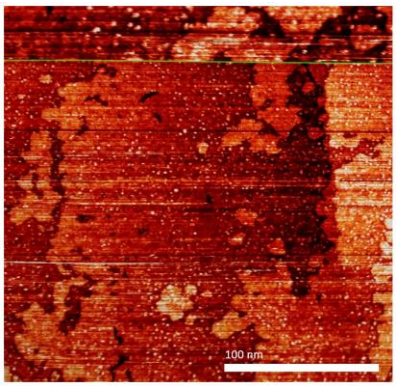

Figure 2.14. Scanning tunneling microscopy image of FeSe on STO.

In order to get high quality images, a user needs to make a high-quality tip. Our tips were made using chemical etching where the tip, typically tungsten wire, which is placed in a NaOH solution and then a cathode placed in the same bath has a voltage applied between the tip and the cathode. The rate of etching impacts the shape of the STM tip. The most desirable

tip shape is one that is very sharp because it will produce the best images. Changing a tip is a very time-consuming process, so when a tip is damaged in the ultra-high vacuum chamber it is easier to try and recover it by smashing it into the sample rather than replacing it altogether.

2.3.4 Scanning Tunneling Spectroscopy

Scanning tunneling spectroscopy uses the same instrumentation as scanning tunneling microscopy except that the tip is kept at a constant position above the surface of the sample and the bias voltage is varied and the resulting differential conductance, dI/dV, is recorded. The differential conductance gives information about the local density of states. We used this technique to determine the position of Dirac point, where the linear bands cross, of a sample of graphene. This can give you information about the type of charge carriers or doping of the sample which can be seen in Figure 2.15 a) and b). Figure 2.15 a) shows the Dirac point below the sample bias meaning that the charge carriers are electrons and in Figure 2.15 b) shows the Dirac point above the sample bias meaning that the carriers are holes.

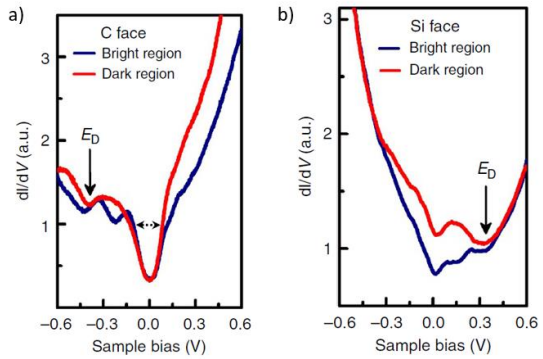

Figure 2.15. Scanning tunneling spectroscopy of graphene. a) Graphene on SiC - C Face from [15] b) Graphene on SiC - Si Face from [15]

2.3.5 Charge Carrier Transport Measurements

Transport measurements can be used to characterize samples in many ways such as determining carrier type, carrier concentration, material doping, metal-insulator transitions, current-voltage characteristics, as well as but not limited to superconductivity. Transport measurements help to highlight the viability of new electronic devices that could potentially replace the current silicon technology used in devices today. Typically, the current and voltage are measured to determine the IV characteristics of the sample. Using this information, you can also deduce the conductivity and resistivity of a sample. This can also be recorded as a function of temperature to help understand the mechanisms involved in the conductance of a sample. The main premise is that the carriers in the metals and semiconductors will react to either an applied electric field or temperature gradient. In non-ballistic regimes, this flow is impacted by scattering from impurities, defects, as well as lattice vibrations, or phonons.

The equation of motion for a charge carrier under the influence of an applied field can be written as

$$\boldsymbol{F} = m\frac{d\boldsymbol{v}}{dt} = -q\boldsymbol{E}. \tag{2.1}$$

Integrating over time τ, which is the time between scattering events we can write the velocity as

$$\boldsymbol{v} = -\frac{e\tau}{m}\boldsymbol{E}. \tag{2.2}$$

The current density can be written as the number of carriers carrying charge *e* at velocity $\boldsymbol{v}$ or $\boldsymbol{j} = -ne\boldsymbol{v}$. Then using Ohm's law, $\boldsymbol{j} = \sigma\boldsymbol{E}$, we can write the current density as

$$\boldsymbol{j} = \frac{ne^2\tau}{m}\boldsymbol{E}. \tag{2.3}$$

This gives us the relation of the conductivity as

$$\sigma = \frac{1}{\rho} = \frac{ne^2\tau}{m}. \tag{2.4}$$

We can see that as the relaxation time increases the conductivity also increases as one would expect. If we include alternating time varying fields, the electric field and the velocity would include a term like $exp(-i\omega t)$, where ω is the frequency. Then the equation of motion for a charge particle can be written as

$$m\frac{d\boldsymbol{v}}{dt} = -e\boldsymbol{E} - m\frac{\boldsymbol{v}}{\tau}, \tag{2.5}$$

yielding a new conductivity relation of

$$\sigma = \frac{ne^2\tau}{m(1-i\omega\tau)}. \tag{2.6}$$

We see that with alternating time varying fields the conductivity is complex and has real and imaginary components.

Measuring the current and voltage are key components to the IV characteristics of a sample. Simple 2 probe methods are not sensitive enough to measure minute changes in voltage, so for accurate methods a 4-point probe method is employed. Figure 2.16 shows a sample Hall bar configuration that is commonly used to measure the IV characteristics of a material. Typically, current is sent from connection 1 to 2 and the potential difference is measured from 3 to 5 and 4 to 6. Then the current is sent in the opposite direction and the potential difference is measured again from the same contacts. Then all the measurements are averaged to get a reading for either the resistivity and/or the conductivity since both are related to each other. Starting from a form of Ohm's law, V=IR, and the noting that the resistance R depends on the geometry of the sample we can write, $R = \rho\frac{l}{t}$. ρ is the resistivity, l

is the length between the voltage probes and t is the thickness of the sample. We can write the resistivity as a function of the IV measurements in the region that the response is linear as

$$\rho = \frac{1}{\sigma} = \frac{t}{l}\frac{V}{I}. \tag{2.7}$$

If the response is not linear then a more complex analysis is required to find the conductivity. The resistance that is measured is useful in determining the mechanisms that are involved during conduction. The Hall bar sample is also advantageous because IV measurements under the presence of a magnetic field can also determine the type of charge carriers by the sign of the Hall coefficient R_H.

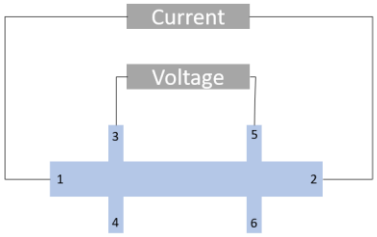

Figure 2.16. Sample Hall bar configuration for IV measurements.

2.3.6 Custom Built Current-Voltage-Temperature Measurement System

A custom built station used to make current-voltage measurements as function of temperature consisted of mechanical vacuum pump, cryo pump, heating coil and control system, Keithley meters to control the current and measure the voltage. The temperature control system and Keithley meters are able to communicate over the general purpose interface bus (GPIB) which can allow control using software such as National Instruments LabVIEW. The custom LabVIEW programs are able to automate the measurements and collect the data.

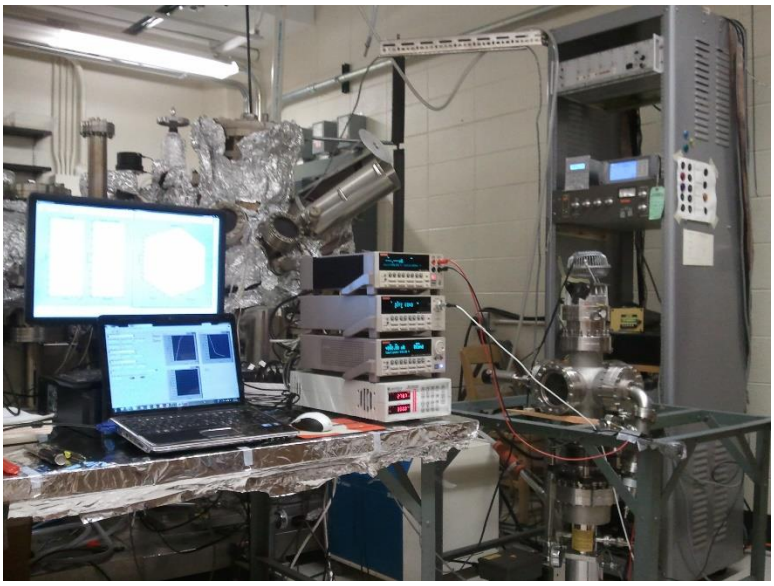

Figure 2.17. A small UHV chamber that uses a cryopump to reduce the temperature in the system as well as other electronic devices used to measure the IV characteristics of a sample.

For polymer transferred graphene, there are many defects in the surface structure due to the transfer method used and induce varying gaps between the transferred material and the substrate. Tomer at al. performed Schottky measurements to show that the surface between graphene and SiC/Si/GaAs has many inhomogeneities creating a distribution of barriers that become evident by the temperature dependence of the IV characteristics [16-18]. This is a challenge for any polymer transferred thin film device.

2.4 Predictive Methods

Predictive methods allow scientists to theoretically probe a material's properties through calculations based on a set of assumptions. This allows many experiments that might be difficult to build in reality to instead take place theoretically. This approach also allows scientists to push the boundary of knowledge and hopefully help guide experimentalists with what types of studies might be the most beneficial. We used density functional theory and tight binding modeling to determine a material's electronic band structure. The electronic band

structure gives a lot of information about a material such as the types of carriers, possible energy gap, energy dispersion relation, and density of states. The electronic band structure can yield important information about a material's electronic, thermal, and optical properties.

2.4.1 Supercell Atomic Structure

To study any system using an ab initio approach, one must accurately describe the crystal structure. When calculations involve supercells, considerations involving supercell size need to be taken into account when determining which supercells to study. For instance, any calculation involving the magic angle twisted bilayer graphene would require around 12,000 atoms in the supercell which makes electron band calculations computationally intensive. Not only would require a large amount of computational power but it would also require more time as well. The approach that is used in this study will be to find the supercells with the least number of atoms to facilitate calculations. We can find supercells for twisted bilayer materials by assuming the center of rotation is located at the center of the common hexagons. In actual materials there is some deformation/relaxation that can occur. For this study, we only allow relaxation to occur for atoms in the direction that is perpendicular to the axis of the layers.

The supercells can be found by starting from a simple hexagonal lattice where we choose an atom as the center and then move outward in concentric circles searching for the next nearest neighbor. As each new atom is identified we can rotate that point into another point on the lattice creating and angle between those two points. This is pictured in Figure 2.18 where the two solid blue lines show the new larger supercell and, the solid red line corresponds to that same cell rotated onto a different lattice point. The dashed magenta rings is how we move outward to check for possible orientations and new angles. The angle between the blue

and the red supercells is the twist angle between these lattices. We can continue to do this to identify new sets of supercells along with their twist angles. The twist angles that are identified are commensurate and only exist for a certain set of angles. As we continue to build larger supercells, some of the twist angles repeat but just for larger supercells which are actually multiples of the smaller supercells with the same angle. This can be seen in Table 2.1 where the $\sqrt{21}\ x\ \sqrt{21}$ supercells are repeat angles of the $\sqrt{7}\ x\ \sqrt{7}$ supercells.

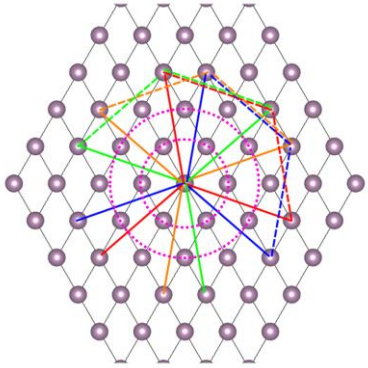

Figure 2.18. Simple hexagonal lattice with concentric rings to show how the twisted structures are created.

Table 2.1. Supercell basis vectors in relation to the primitive cell

Cell Type	Angle (°)	Layer	Direction		
			A	B	C
$\sqrt{7}\ x\ \sqrt{7}$	21.787	top	$a_1 = \frac{2}{7} A_1 - \frac{1}{7} A_2$	$a_2 = \frac{1}{7} A_1 + \frac{3}{7} A_2$	c
		bottom	$a_1 = \frac{1}{7} A_1 - \frac{2}{7} A_2$	$a_2 = \frac{2}{7} A_1 + \frac{3}{7} A_2$	c
	38.213	top	$a_1 = \frac{1}{7} A_1 - \frac{2}{7} A_2$	$a_2 = \frac{2}{7} A_1 + \frac{3}{7} A_2$	c
		bottom	$a_1 = -\frac{1}{7} A_1 - \frac{3}{7} A_2$	$a_2 = \frac{3}{7} A_1 + \frac{2}{7} A_2$	c
$\sqrt{13}\ x\ \sqrt{13}$	27.796	top	$a_1 = \frac{1}{13} A_1 - \frac{3}{13} A_2$	$a_2 = \frac{3}{13} A_1 + \frac{4}{13} A_2$	c
		bottom	$a_1 = -\frac{1}{13} A_1 - \frac{4}{13} A_2$	$a_2 = \frac{4}{13} A_1 + \frac{3}{13} A_2$	c

	32.204	top	$a_1 = \frac{3}{13} A_1 - \frac{1}{13} A_2$	$a_2 = \frac{1}{13} A_1 + \frac{4}{13} A_2$	c
		bottom	$a_1 = \frac{1}{13} A_1 - \frac{3}{13} A_2$	$a_2 = \frac{3}{13} A_1 + \frac{4}{13} A_2$	c
$\sqrt{19}\, x\, \sqrt{19}$	13.174	top	$a_1 = \frac{3}{19} A_1 - \frac{2}{19} A_2$	$a_2 = \frac{2}{19} A_1 + \frac{5}{19} A_2$	c
		bottom	$a_1 = \frac{2}{19} A_1 - \frac{3}{19} A_2$	$a_2 = \frac{3}{19} A_1 + \frac{5}{19} A_2$	c
	46.826	top	$a_1 = \frac{2}{19} A_1 - \frac{3}{19} A_2$	$a_2 = \frac{3}{19} A_1 + \frac{5}{19} A_2$	c
		bottom	$a_1 = -\frac{2}{19} A_1 - \frac{5}{19} A_2$	$a_2 = \frac{5}{19} A_1 + \frac{3}{19} A_2$	c
$\sqrt{21}\, x\, \sqrt{21}$	21.787	top	$a_1 = \frac{1}{21} A_1 - \frac{4}{21} A_2$	$a_2 = \frac{4}{21} A_1 + \frac{5}{21} A_2$	c
		bottom	$a_1 = -\frac{1}{21} A_1 - \frac{5}{21} A_2$	$a_2 = \frac{5}{21} A_1 + \frac{4}{21} A_2$	c
	38.213	top	$a_1 = \frac{4}{21} A_1 - \frac{1}{21} A_2$	$a_2 = \frac{1}{21} A_1 + \frac{5}{21} A_2$	c
		bottom	$a_1 = \frac{1}{21} A_1 - \frac{4}{21} A_2$	$a_2 = \frac{4}{21} A_1 + \frac{5}{21} A_2$	c

2.4.2 Density Functional Theory

There are many methods to extract information from crystal systems. Here we focus on using density functional theory to calculate the electronic structure of various TMDs to include ones with defects and twists. Density functional theory shifts away from the traditional approach of focusing on the wavefunction information but instead focuses on the electron density, or more accurately the system energy is a functional of the electron density [19]. It is standard to assume the Born-Oppenheimer approximation where the heavy nuclear centers move little in terms of their electron counterparts and thus can be fixed. Then we can write the many electron Schrödinger equation as:

$$\hat{H}\Psi = \left[-\sum_i \frac{\hbar^2}{2m_e} \nabla_{r_i}^2 - \sum_{i,\alpha} \frac{Z_\alpha e^2}{|r_i - R_\alpha|} + \frac{1}{2} \sum_{i \neq j} \frac{e^2}{|r_i - r_j|} \right] \Psi = E\Psi \tag{2.8}$$

which includes the electron kinetic energies, electron potential from the nuclei, and the electron-electron interaction. The many electron problem can be reduced using simple products of one electron orbitals that obey the Pauli exclusion principle. These can be computed using the Slater determinant.

Moving towards an electron density approach, we then utilize 2 theorems proved by Hohenburg and Kohn [20]:

Theorem 1. The electron density of a closed system determines the external potential uniquely, to within an additive constant.

Proof:

Starting from the Schrödinger equation, let $n(\boldsymbol{r})$ be the non-degenerate ground state density in the potential $v_1(\boldsymbol{r})$, then we can write

$$E_1 = \langle \Psi_1 | \mathrm{H}_1 | \Psi_1 \rangle \tag{2.9 a}$$

$$= \langle \Psi_1 | T + U | \Psi_1 \rangle + \int v_1(\boldsymbol{r}) n(\boldsymbol{r}) d\boldsymbol{r} \tag{2.9 b}$$

where T and U are the kinetic energy and interaction energy operators. Suppose there is another different wavefunction and potential that give the same density, then we can write

$$E_2 = \langle \Psi_2 | T + U | \Psi_2 \rangle + \int v_2(\boldsymbol{r}) n(\boldsymbol{r}) d\boldsymbol{r} \tag{2.10}$$

Using the variational method, we can use Ψ_2 as a trial wavefunction for H_1.

$$E_1 < \langle \Psi_2 | \mathrm{H}_1 | \Psi_2 \rangle \tag{2.11 a}$$

$$= \langle \Psi_2 | T + U | \Psi_2 \rangle + \int v_1(\boldsymbol{r}) n(\boldsymbol{r}) d\boldsymbol{r} \tag{2.11 b}$$

$$= E_2 + \int [v_1(\boldsymbol{r}) - v_2(\boldsymbol{r})] n(\boldsymbol{r}) d\boldsymbol{r}. \tag{2.11 c}$$

Doing the same for use Ψ_1 as a trial wavefunction for H_2,

$$= E_1 + \int [v_2(\boldsymbol{r}) - v_1(\boldsymbol{r})] n(\boldsymbol{r}) d\boldsymbol{r}. \tag{2.12}$$

Now adding these equations, we arrive at the contradiction

$$E_1 + E_2 < E_1 + E_2, \tag{2.13}$$

meaning that the second potential that does equal the first potential plus a constant does not give the same density must be wrong. This means that the density $n(\vec{r})$ uniquely defines the potential and all ground state properties derived from the Hamiltonian H.

Theorem 2. For any positive definite trial density , ρ_t, such that

$$\int \rho_t(\boldsymbol{r})\, d\boldsymbol{r} = N \text{ then } E[\rho_t] \geq E_0 \tag{2.14}$$

Starting with a trial ground state wavefunction, we want to use the variational principle to show that

$$E = min\langle\psi|H|\psi\rangle. \tag{2.15}$$

For a given density n(r) which determines the ground state and external potential we can rewrite equation 2.15 as

$$E_v[n(\boldsymbol{r})] = min\langle\psi_n|H|\psi_n\rangle \tag{2.16 a}$$

$$= \int v(\boldsymbol{r})n(\boldsymbol{r})d\boldsymbol{r} + F[n(\boldsymbol{r})] \tag{2.16 b}$$

where F[n(**r**)] is a universal functional of the density and can be written as

$$F[n(\boldsymbol{r})] = min\langle\psi_n|T + U|\psi_n\rangle. \tag{2.17}$$

Minimizing the density n(r) we can write

$$min\ E_v[n(\boldsymbol{r})] = min[\int v(\boldsymbol{r})n(\boldsymbol{r})d\boldsymbol{r} + F[n(\boldsymbol{r})]] \geq E_0 \tag{2.18}$$

where the equality holds for the minimum density n_0(r). Now instead of minimizing the wavefunction to find the ground state energy, all that is required is to minimize the density to find the ground state of the system.

The first theorem asserts that the electron density determines the Hamiltonian operator. The second allows us to take a variational approach when solving for the ground state energy. We can write the following equation using these two theorems

$$\delta[E[\rho] - \mu(\int \rho(\boldsymbol{r})d\boldsymbol{r} - N)] = 0 \tag{2.19}$$

where E is a functional of the density ρ, μ is a Lagrange multiplier or chemical potential, and N is the total number of electrons. Then each term in the Hamiltonian can be written as a functional of the density. Kohn and Sham later proposed a solution to this equation where they wrote the kinetic energy and the density as a set of non-interacting orbitals. The kinetic term is not exact, but the density is the true density since it is constructed from a set of orbitals like so

$$\rho(\boldsymbol{r}) = \sum_i^N |\phi_i(\boldsymbol{r})|^2 \tag{2.20}$$

We can take a similar approach with the Coulomb interaction as we did with the density and rewrite the Hamiltonian to correct for the error in the kinetic and potential energies as

$$E[\rho] = T_s[\rho] + V_{ext}[\rho] + V_C[\rho] + E_{xc}[\rho] \tag{2.21}$$

where the subscript s denotes that this is not the true kinetic energy, V_C is the classical Coulomb energy, E_{xc} is the exchange correlation which incorporates the error from our assumptions but allows us to calculate the energy using the density. Lastly, we can write the Schrödinger equation as:

$$\left[-\frac{1}{2}\nabla^2 + v_{ext} + \int \frac{\rho(\boldsymbol{r\prime})}{|\boldsymbol{r}-\boldsymbol{r\prime}|}d\boldsymbol{r}' + v_{xc}(\boldsymbol{r})\right]\phi_i(\boldsymbol{r}) = \varepsilon_i\phi_i(\boldsymbol{r}) \tag{2.22}$$

where,

$$v_{xc}(\boldsymbol{r}) = \frac{\delta E_{xc}[\rho]}{\delta\rho}. \tag{2.23}$$

These equations are the key components of DFT. These set of equations are solved iteratively until self-consistency is achieved by the filled states $\phi_i(\boldsymbol{r})$ and the electron density used in

$v_{xc}(\boldsymbol{r})$. The complex electron-electron interactions are absorbed in the exchange correlation functional and play an important role in calculating the ground state energy. The exact form of the electron exchange correlation is not known but some common approximations to the exchange correlation functionals are the local-density approximation (LDA) or the generalized gradient approximation (GGA).

2.4.2.1 Exchange Correlation Functionals

The exchange correlation functionals absorb the complex interactions between the many electrons within a system and its impact on the total energy of the system. This arises from the fact that the electrons are indistinguishable and cannot occupy the same quantum mechanical state resulting in a repulsion between the electrons impacting the total energy of the system. The exchange correlation functionals are not known and there are two main approximations that are used in density functional theory, the local density and generalized gradient approximations. These approximations must incorporate the properties of the particles and their interaction such as the Pauli exclusion principle. This leads to the concept of the exchange-correlation hole where the probability of finding an electron in the proximity of another to be reduced. We can write the exchange correlation conditional probability of finding an electron at $\mathbf{r}_2$ given that there is an electron at $\mathbf{r}_1$ as

$$P_{xc}(\boldsymbol{r}_1, \boldsymbol{r}_2) = \frac{P_2(\boldsymbol{r}_1, \boldsymbol{r}_2)}{\rho(\boldsymbol{r}_1)} - \rho(\boldsymbol{r}_2). \tag{2.24}$$

We also require the normalization condition where integrating over all space we find exactly one electron,

$$\int P_{xc}(\boldsymbol{r}_1, \boldsymbol{r}_2) d\boldsymbol{r}_2 = -1 \tag{2.25}$$

2.4.2.1.1 Local Density Approximation

The local density approximation assumes that the exchange correlation energy depends on the particle density at that point in space within a range of **r** and is not affected by changes outside that range [21]. For a system whose density varies slowly, an approximation of the exchange correlation energy can be written as

$$E_{xc} \approx \int \varepsilon_{xc}[n(\boldsymbol{r})]d\boldsymbol{r} \tag{2.26}$$

which leads to the exchange correlation potential

$$v_{xc}[n(\boldsymbol{r})] \approx \frac{d\varepsilon_{xc}[n(\boldsymbol{r})]}{dn(\boldsymbol{r})} = \mu_{xc}[n(\boldsymbol{r})]. \tag{2.27}$$

A simple approximation is to ignore the correlation effects and assume the exchange energy is Coulombic in nature and the density is the same of the homogeneous electron gas then we can write the exchange energy as [22]

$$\varepsilon_{xc}[n(\boldsymbol{r})] \approx -\frac{e^2}{2\pi^{1/3}}\left(3n(\boldsymbol{r})\right)^{4/3}, \tag{2.28}$$

as well as the exchange potential

$$v_{xc}[n(\boldsymbol{r})] \approx -2e^2\left(\frac{3n(\boldsymbol{r})}{\pi}\right)^{1/3}. \tag{2.29}$$

Based on these simple assumptions, DFT using the LDA has been successful in calculating the energy bands for even complex structures. Perdew and Wang published their model of the energy associated with correlation and it has proven to be accurate [23]. Unfortunately, LDA does a poor job in estimating the form of P_{xc} but it satisfies the sum condition of the Pauli exclusion principle.

2.4.2.1.2 Generalized Gradient Approximation

The generalized gradient approximation is an extension of the LDA with the inclusion of the gradient of the local density to account for the inhomogeneity of the true electron density. This can be interpreted as a Taylor series expansion of the density where LDA is first term in the expansion and is the uniform density. Each additional term would be a correction to this uniform density and the gradient expansion approximation (GEA) includes the next lowest term which can be written as

$$E_{xc}^{GEA}[\rho_\alpha, \rho_\beta] = \int \rho \varepsilon_{xc}(\rho_\alpha, \rho_\beta)\, d\boldsymbol{r} + \sum_{\sigma,\sigma'} \int C_{xc}^{\sigma\sigma'}(\rho_\alpha, \rho_\beta) \frac{\nabla\rho_\sigma}{\rho_\sigma^{2/3}} \frac{\nabla\rho_{\sigma'}}{\rho_{\sigma'}^{2/3}}\, d\boldsymbol{r}. \quad (2.30)$$

The GEA performed poorly due to the fact that it did not enforce the exchange correlation hole condition. Perdew used the real space cutoff in the density gradient to fulfill the exchange correlation hole condition [24] leading to the general gradient corrected exchange energy

$$E_{xc}^{GGA}[\rho_\alpha, \rho_\beta] = \int f(\rho_\alpha, \rho_\beta, \nabla\rho_\alpha, \nabla\rho_\beta)\, d\boldsymbol{r}. \quad (2.31)$$

In an attempt to find functional forms of the exchange correlation energy using GGA we separate the exchange and correlation energies. While this might be useful it has proven to be difficult to gain any physical insight using these forms so instead, we can write the exchange correlation energy in terms of a perturbation to the LDA. We can write the exchange energy contribution as

$$E_X^{GGA} = E_X^{LDA} - \sum_\sigma \int F(s_\sigma) \rho_\sigma^{4/3}(\boldsymbol{r}) d\boldsymbol{r}. \quad (2.32)$$

Here F is the reduced gradient density for spin σ

$$s_\sigma = \frac{|\nabla\rho_\sigma(\boldsymbol{r})|}{\rho_\sigma^{4/3}(\boldsymbol{r})} \quad (2.33)$$

and accounts for the local inhomogeneity.

In this work, the Perdew, Burke, and Ernzerhof (PBE) functionals are used for the density functionals in the calculations. These functionals start from the work down by Perdew and Wang form of the exchange and correlation [23] and include modifications that provide an accurate description of the linear response of the uniform electron gas, correct behavior under uniform scaling, as well as a smoother potential [25].

2.4.2.2 Calculations using Vienna Ab initio Simulation Package

The Vienna ab-initio simulation package (VASP) is a computer program used for atomic scale modeling of materials [26]. In this dissertation, VASP is the main tool used in solving for the electronic structure properties such as the energy bands, charge densities, density of states, optical properties, as well as other physical properties. VASP has many parameters that a user can enable to incorporate constraints based on the type of the materials under study, such as enable weak van der Waals interactions between layered materials like graphene, or TMDs.

2.4.2.2.1 Energy Band Calculations

Energy band calculations were performed using the VASP software package and the projected augmented wave (PAW) approach. The electron-electron interactions have been captured in the ultra-soft pseudopotentials available through the VASP database. The Monkhorst-Pack sampling scheme was used to generate a uniform k-point grid sampling in the first Brillouin Zone. The generalized gradient approximation using PBE functionals was also used to describe the electron exchange correlation interactions. Band unfolding was also required to compare the energy bands of the supercell to the energy bands of the primitive cell in its BZ. This way we can do a direct comparison of the effect twisting the bilayers has on the energy bands. The band unfolding was achieved by comparing the lattice vectors of the

supercell and primitive cell given the constraints that the supercell reciprocal lattice vectors are also reciprocal lattice vectors of the primitive BZ. In addition to band unfolding, layer projection was also performed on the systems to further determine which layer contributes to which part of the band structure. This is helpful when the layers contain different types of atoms. This can also be seen by doing an orbital band projection for each element and its orbitals. This allows us to further probe not only the layers but the atoms themselves along with their contributing orbitals.

2.4.2.2.2 Optical Conductivity

In section, we will briefly cover some key electromagnetic concepts that relate to the conductivity of a material and theoretical calculations that can be used to obtain the optical response of a material. The optical response in TMDs plays a larger role because of the direct band gap at K and K' and the large binding energy of the excitons formed in TMDs [27,28]. The strong light matter interaction within TMDs, resulting from their excitonic properties, presents itself as strong photoluminescence and absorption characteristics [27,28].

The induced dipole moment from each charge carrier is $\vec{p} = -e\vec{r}$. The displacement $\vec{r}$ can be found by integrating the velocity of the charge carriers. Then summing over all charges, we can write the polarization as

$$\vec{P} = -ne\vec{r} = -\frac{ne^2}{m}\frac{1}{\omega^2+i\omega/\tau}\vec{E}. \tag{2.34}$$

Recall, $\vec{D} = \epsilon_0\vec{E} + \epsilon_0\chi_e\vec{E} = \epsilon\vec{E}$, then we can write the frequency dependent dielectric function as

$$\frac{\epsilon(\omega)}{\epsilon_0} = 1 - \frac{\omega_p^2}{\omega^2+i\omega/\tau}, \tag{2.35}$$

where the plasma frequency is written as $\omega_p^2 = \frac{ne^2}{\epsilon_0 m}$. The dielectric function has both real and imaginary components. The Kramers-Kronig relations relate the real and imaginary parts of the dielectric function and are typically written as [29]

$$Re\ \epsilon(\omega)/\epsilon_0 = 1 + \frac{2}{\pi} P \int_0^\infty \frac{\omega' Im\ \epsilon(\omega\prime)/\epsilon_0}{\omega'^2 - \omega^2} d\omega' \tag{2.36}$$

$$Im\ \epsilon(\omega)/\epsilon_0 = -\frac{2\omega}{\pi} P \int_0^\infty \frac{[Re\ \epsilon(\omega\prime)/\epsilon_0 - 1]}{\omega'^2 - \omega^2} d\omega' \tag{2.37}$$

The imaginary part of the dielectric function can be measured using methods that probe the energy absorption of a material. Using the Kramers-Kronig relations and the measured imaginary part of the dielectric function, one can obtain the real part of the dielectric function in order to understand the frequency response of the material.

The following is the derivation from VASP literature on how the dielectric properties are calculated. The derivation relies on the fact that with small perturbations the response is linear. An external potential is applied as a perturbation and the Kohn-Sham equations are solved giving information about the excited states. The dielectric function is calculated from the excited states. Starting from the response of the internal electric field in a material to an external electric field we can write [30]

$$\boldsymbol{E} = \epsilon^{-1} \boldsymbol{E}_{ext}. \tag{2.38}$$

where ϵ is the dielectric tensor. This external field causes a change in the charge density which results in an induced potential which can be written as

$$\rho_{ind} = \chi v_{ext} \tag{2.39}$$

$$\rho_{ind} = P v_{tot} \tag{2.40}$$

where $v_{tot} = v_{ext} + v_{ind}$, χ is the reducible polarizability, and P is the irreducible polarizability.

Relating the dielectric constant and the polarizability we can write

$$\epsilon^{-1} = 1 + v\chi \tag{2.41}$$

$$\epsilon = 1 - vP \tag{2.42}$$

$$\chi = P + Pv\chi \tag{2.43}$$

where v is the Coulomb kernel and can be written as $v = \frac{4\pi e^2}{q^2}$.

We can also write equation 2.38 in terms of micro and macroscopic dielectric functions,

$$\boldsymbol{E}(\boldsymbol{r}, \omega) = \int \epsilon_{mac}^{-1}(\boldsymbol{r} - \boldsymbol{r}', \omega)\boldsymbol{E}_{ext}(\boldsymbol{r}', \omega)d\boldsymbol{r}' \tag{2.44}$$

$$\boldsymbol{e}(\boldsymbol{r}, \omega) = \int \epsilon^{-1}(\boldsymbol{r}, \boldsymbol{r}', \omega)\boldsymbol{E}_{ext}(\boldsymbol{r}', \omega)d\boldsymbol{r}', \tag{2.45}$$

where the macro form focuses on averages over the sample whereas the micro form focuses on where you are in the material and where the other charges are. We can also write equations 2.44 and 2.45 in momentum space as

$$\boldsymbol{E}(\boldsymbol{q}, \omega) = \epsilon_{mac}^{-1}(\boldsymbol{q}, \omega)\boldsymbol{E}_{ext}(\boldsymbol{q}, \omega) \tag{2.46}$$

$$\boldsymbol{e}(\boldsymbol{q} + \boldsymbol{G}, \omega) = \sum_{\boldsymbol{G}'} \epsilon_{\boldsymbol{G},\boldsymbol{G}'}^{-1}(\boldsymbol{q}, \omega)\, \boldsymbol{E}_{ext}(\boldsymbol{q} + \boldsymbol{G}', \omega). \tag{2.47}$$

Now relating the microscopic dielectric function to the external field we can write

$$\epsilon_{\boldsymbol{G},\boldsymbol{G}'}^{-1}(\boldsymbol{q}, \omega) = \delta_{\boldsymbol{G},\boldsymbol{G}'} + \frac{4\pi e^2}{|\boldsymbol{q}+\boldsymbol{G}||\boldsymbol{q}+\boldsymbol{G}'|} \frac{\partial \rho_{ind}(\boldsymbol{q}+\boldsymbol{G},\omega)}{\partial v_{ext}(\boldsymbol{q}+\boldsymbol{G}',\omega)} \tag{2.48}$$

$$\epsilon_{\boldsymbol{G},\boldsymbol{G}'}(\boldsymbol{q}, \omega) = \delta_{\boldsymbol{G},\boldsymbol{G}'} - \frac{4\pi e^2}{|\boldsymbol{q}+\boldsymbol{G}||\boldsymbol{q}+\boldsymbol{G}'|} \frac{\partial \rho_{ind}(\boldsymbol{q}+\boldsymbol{G},\omega)}{\partial v_{tot}(\boldsymbol{q}+\boldsymbol{G}',\omega)} \tag{2.49}$$

where

$$\chi_{\boldsymbol{G},\boldsymbol{G}'}(\boldsymbol{q}, \omega) = \frac{\partial \rho_{ind}(\boldsymbol{q}+\boldsymbol{G},\omega)}{\partial v_{ext}(\boldsymbol{q}+\boldsymbol{G}',\omega)} \tag{2.50}$$

$$P_{\boldsymbol{G},\boldsymbol{G}'}(\boldsymbol{q}, \omega) = \frac{\partial \rho_{ind}(\boldsymbol{q}+\boldsymbol{G},\omega)}{\partial v_{tot}(\boldsymbol{q}+\boldsymbol{G}',\omega)} \tag{2.51}$$

$$v^{S}_{\boldsymbol{G},\boldsymbol{G}'}(\boldsymbol{q}) = \frac{4\pi e^2}{|\boldsymbol{q}+\boldsymbol{G}||\boldsymbol{q}+\boldsymbol{G}'|}. \tag{2.52}$$

Using the Dyson equation, we can also relate P and χ which takes on the form

$$\chi_{\boldsymbol{G},\boldsymbol{G}'}(\boldsymbol{q},\omega) = P_{\boldsymbol{G},\boldsymbol{G}'}(\boldsymbol{q},\omega) + \sum_{\boldsymbol{G}_1,\boldsymbol{G}_2} P_{\boldsymbol{G}_1,\boldsymbol{G}_2}(\boldsymbol{q},\omega) v^{S}_{\boldsymbol{G}_1,\boldsymbol{G}_2}(\boldsymbol{q}) \chi_{\boldsymbol{G}_2,\boldsymbol{G}'}(\boldsymbol{q},\omega). \tag{2.53}$$

In the Kohn-Sham picture along with the independent particle approximation we can access the irreducible polarizability χ^0 and Adler [31] derived an expression in terms of Bloch functions in reciprocal space which can be written as

$$\chi^0_{\boldsymbol{G},\boldsymbol{G}'}(\boldsymbol{q},\omega) = \frac{1}{\Omega}\sum_{nn'\boldsymbol{k}} 2\omega_{\boldsymbol{k}}\left(f_{n'\boldsymbol{k}+\boldsymbol{q}} - f_{n\boldsymbol{k}}\right) \frac{\left\langle \psi_{n'\boldsymbol{k}+\boldsymbol{q}} \middle| e^{(i(\boldsymbol{q}+\boldsymbol{G})\boldsymbol{r})} \middle| \psi_{n\boldsymbol{k}} \right\rangle \left\langle \psi_{n\boldsymbol{k}} \middle| e^{(-i(\boldsymbol{q}+\boldsymbol{G}')\boldsymbol{r}')} \middle| \psi_{n'\boldsymbol{k}+\boldsymbol{q}} \right\rangle}{\epsilon_{n'\boldsymbol{k}+\boldsymbol{q}} - \epsilon_{n\boldsymbol{k}} - \omega - i\eta}. \tag{2.54}$$

We can also rewrite equations 2.41, 2.42, and 2.43 to include the exchange correlation terms such that

$$\chi = \chi^0 + \chi^0(\upsilon + f_{xc})\chi \tag{2.55}$$

$$P = \chi^0 + \chi^0 f_{xc} P \tag{2.56}$$

$$\chi = P + P\upsilon\chi \tag{2.57}$$

where $f_{xc} = \left.\frac{\partial \upsilon_{xc}}{\partial \rho}\right|_{\rho=\rho_0}$. Using the random phase approximation (RPA), $P = \chi^0$, then we can write equation 2.49 as

$$\epsilon_{\boldsymbol{G},\boldsymbol{G}'}(\boldsymbol{q},\omega) = \delta_{\boldsymbol{G},\boldsymbol{G}'} - \frac{4\pi e^2}{|\boldsymbol{q}+\boldsymbol{G}||\boldsymbol{q}+\boldsymbol{G}'|}\chi^0_{\boldsymbol{G},\boldsymbol{G}'}(\boldsymbol{q},\omega). \tag{2.58}$$

In the long wavelength limit, where $\boldsymbol{q} \to 0$, the dominant term in the dielectric tensor is the $\epsilon_{0,0}$ term. Then we can finally arrive at the imaginary part of the dielectric function

$$\epsilon^{(2)}_{\alpha\beta}(\omega) = \frac{4\pi e^2}{\Omega}\lim_{q\to 0}\frac{1}{q^2}\sum_{v,c,\boldsymbol{k}} 2\omega_{\boldsymbol{k}}\delta(\epsilon_{c\boldsymbol{k}} - \epsilon_{v\boldsymbol{k}} - \omega)\left\langle u_{c\boldsymbol{k}+qe_\alpha} \middle| u_{v\boldsymbol{k}} \right\rangle \left\langle u_{v\boldsymbol{k}} \middle| u_{c\boldsymbol{k}+qe_\beta} \right\rangle \tag{2.59}$$

where *c* and *v* are the conduction and valence band states. The summation is performed over the empty states yielding the imaginary part of the dielectric function. We can use the

Kramers-Kronig relations to find the real part of the dielectric function and also the optical conductivity because those quantities are related. To find the relationship between the dielectric function and the conductivity we start with the electric current and the displacement under alternating time varying fields. We can write them as

$$\boldsymbol{j}(\omega) = \sigma \boldsymbol{E}(\omega) \tag{2.60}$$

$$\boldsymbol{D}(\omega) = \epsilon_0 \boldsymbol{E}(\omega). \tag{2.61}$$

Now using Maxwell's equations for the curl of the auxiliary field we can write

$$\nabla \times \boldsymbol{H} = \mu_0 \frac{\partial \boldsymbol{D}}{\partial t} + \mu_0 \boldsymbol{j} = \mu_0 \left(\epsilon_0 + \frac{i\sigma}{\omega}\right) \frac{\partial \boldsymbol{E}}{\partial t} = \mu_0 \epsilon(\omega) \frac{\partial \boldsymbol{E}}{\partial t}. \tag{2.62}$$

Rearranging terms to write the conductivity in terms of the dielectric function as

$$\sigma(\omega) = i\omega\big(\epsilon_0 - \epsilon(\omega)\big). \tag{2.63}$$

2.4.3 Tight Binding Method

The tight binding method is used to calculate the energy bands of a system using a linear combination of atomic orbitals (LCAO). The main concepts in the tight binding method are that if we have wavefunctions of separate atoms, ψ_A and ψ_B, that are far apart and, we bring them closer together, their wavefunctions overlap resulting in states that are linear combinations of the wavefunctions with differing energy levels, $\psi_A \pm \psi_B$. Starting with the electron wavefunction of a system and the Hamiltonian operator, $H = H_{at} + \Delta U$ where H_{at} is the atomic Hamiltonian, we can write the Hamiltonian as

$$H|\psi_{nk}\rangle = E|\psi_{nk}\rangle. \tag{2.64}$$

where *n* and *k* are the band index and wavevector respectively. The atomic wavefunctions are eigenstates of the atomic Hamiltonian,

$$H_{at}\phi_i(\boldsymbol{r}) = \epsilon_i \phi_i(\boldsymbol{r}) \tag{2.65}$$

where ϵ_i is the energy of the ith isolation atom. The states ϕ_i are not required to be orthonormal but typically are in order to make the math easier. The electron wavefunction must have the periodicity of the lattice, meaning that is going to be similar to the Bloch form, so we can write

$$\psi_{nk}(\boldsymbol{r}) = \frac{1}{\sqrt{N}} \sum_R exp(i\boldsymbol{k} \cdot \boldsymbol{R}) \phi_{nk}(\boldsymbol{r} - \boldsymbol{R}). \tag{2.66}$$

Proof:

If T is a translation vector then

$$\psi_{nk}(\boldsymbol{r} + \boldsymbol{T}) = \frac{1}{\sqrt{N}} \sum_R exp(i\boldsymbol{k} \cdot \boldsymbol{R}) \phi_{nk}(\boldsymbol{r} - \boldsymbol{R} + \boldsymbol{T}) \tag{2.67 a}$$

$$= \frac{1}{\sqrt{N}} exp(i\boldsymbol{k} \cdot \boldsymbol{T}) \sum_R exp\big(i\boldsymbol{k} \cdot (\boldsymbol{R} - \boldsymbol{T})\big) \phi_{nk}\big(\boldsymbol{r} - (\boldsymbol{R} - \boldsymbol{T})\big) \tag{2.67 b}$$

$$= \psi_{nk}(\boldsymbol{r}) \frac{1}{\sqrt{N}} exp(i\boldsymbol{k} \cdot \boldsymbol{T}). \tag{2.67 c}$$

Which is the Bloch condition we sought to satisfy. Now writing the total wavefunction as a linear combination of periodic wavefunctions, ψ_α, we have

$$\psi = \sum_\alpha u_\alpha \psi_\alpha. \tag{2.68}$$

We can find the eigenvalues of the system by solving the Hamiltonian matrix formed from $\langle \psi | H | \psi \rangle$. This can be written as

$$\langle \psi_\beta | H (\sum_\alpha u_\alpha | \psi_\alpha \rangle) = E \langle \psi_\beta | \sum_\alpha u_\alpha | \psi_\alpha \rangle \tag{2.69 a}$$

$$\sum_\alpha u_\alpha \langle \psi_\beta | H | \psi_\alpha \rangle = E \sum_\alpha u_\alpha \langle \psi_\beta | \psi_\alpha \rangle \tag{2.69 b}$$

$$H_{\beta\alpha} a_\alpha = E S_{\beta\alpha} a_\alpha \tag{2.69 c}$$

$$\big(H_{\beta\alpha} - E S_{\beta\alpha}\big) a_\alpha = 0 \tag{2.69 d}$$

where

$$H_{\beta\alpha} = \langle \psi_\beta | H | \psi_\alpha \rangle \tag{2.70}$$

$$S_{\beta\alpha} = \langle \psi_\beta | \psi_\alpha \rangle. \tag{2.71}$$

A non-trivial solution is found by finding the determinant of equation 2.69 d, which can be written as

$$\left| H_{\beta\alpha} - ES_{\beta\alpha} \right| = 0, \tag{2.72}$$

where the eigenvalues of this matrix are also the eigenvalues of the system, or rather energy bands of the system.

2.4.3.1 Slater-Koster Parameters

Writing equations 2.70 and 2.71 in terms of the orbitals in real space we have

$$H_{\beta\alpha} = \frac{1}{N} \sum_R \sum_{R'} e^{(ik\cdot(R-R'))} \int \phi_\beta^*(r-R) H \phi_\alpha(r-R')dr \tag{2.73}$$

$$S_{\beta\alpha} = \frac{1}{N} \sum_R \sum_{R'} e^{(ik\cdot(R-R'))} \int \phi_\beta^*(r-R) \phi_\alpha(r-R')dr. \tag{2.74}$$

The integral part of equation 2.73 is known as the hopping parameters and the integral part of equation 2.74 is known as the overlap integrals. Slater and Koster simplified the matrix elements found in solving the tight binding problem [32]. These are typically known as the direction cosines and they focus on the vector from one state to the other. They are of the form

$$r_i = l\hat{x} + m\hat{y} + n\hat{z} \tag{2.75}$$

and the solution to the hopping integral is of the form

$$E_{\alpha,\beta} = \langle R, \beta | H | R', \alpha \rangle = \frac{1}{N} \sum_R \sum_{R'} e^{(ik\cdot(R-R'))} \int \phi_\beta^*(r-R) H \phi_\alpha(r-R')dr. \tag{2.76}$$

The solutions are in terms of the vector from one state to the other and the strength of the potential as well as the type of bond noted as $V_{\alpha\beta\gamma}$ where α,β are the basis orbitals and γ is the type of bond between those orbitals. The basis set used in this dissertation to represent the

atomic orbitals are the real atomic orbitals: s, p_x, p_y, p_z, d_{xy}, d_{yz}, d_{zx}, $d_{x^2-y^2}$ and d_{z^2}. Now using the basis set relevant to our material system we can solve the determinant of the matrix using the simplified direction cosines in table 2.2. The potential terms are used as fit parameters used when fitting tight binding bands to DFT energy bands calculations. Typically, bands around the Fermi level or around the symmetry points are used when determining the strength of these potentials.

Table 2.2. Energy integrals as a function of direction cosines

$E_{s,s}$	$V_{ss\sigma}$
$E_{s,x}$	$lV_{sp\sigma}$
$E_{x,x}$	$l^2V_{pp\sigma} + (1-l^2)V_{pp\pi}$
$E_{x,y}$	$lmV_{pp\sigma} - lmV_{pp\pi}$
$E_{x,z}$	$lnV_{pp\sigma} - lnV_{pp\pi}$
$E_{s,xy}$	$\sqrt{3}lmV_{sd\sigma}$
E_{s,x^2-y^2}	$\frac{1}{2}\sqrt{3}(l^2-m^2)V_{sd\sigma}$
$E_{s,3z^2-r^2}$	$\left[n^2 - \frac{1}{2}(l^2+m^2)\right]V_{sd\sigma}$
$E_{x,xy}$	$\sqrt{3}l^2mV_{pd\sigma} + m(1-2l^2)V_{pd\pi}$
$E_{x,yz}$	$\sqrt{3}lmnV_{pd\sigma} - 2lmnV_{pd\pi}$
$E_{x,zx}$	$\sqrt{3}l^2nV_{pd\sigma} + n(1-2l^2)V_{pd\pi}$
E_{x,x^2-y^2}	$\frac{1}{2}\sqrt{3}l(l^2-m^2)V_{pd\sigma} + l(1-l^2+m^2)V_{pd\pi}$
E_{y,x^2-y^2}	$\frac{1}{2}\sqrt{3}m(l^2-m^2)V_{pd\sigma} - m(1+l^2-m^2)V_{pd\pi}$
E_{z,x^2-y^2}	$\frac{1}{2}\sqrt{3}n(l^2-m^2)V_{pd\sigma} - n(l^2-m^2)V_{pd\pi}$
$E_{x,3z^2-r^2}$	$l\left[n^2 - \frac{1}{2}(l^2+m^2)\right]V_{pd\sigma} - \sqrt{3}ln^2V_{pd\pi}$

$E_{y,3z^2-r^2}$	$m\left[n^2-\frac{1}{2}(l^2+m^2)\right]V_{pd\sigma}-\sqrt{3}mn^2V_{pd\pi}$
$E_{z,3z^2-r^2}$	$n\left[n^2-\frac{1}{2}(l^2+m^2)\right]V_{pd\sigma}-\sqrt{3}n(l^2+m^2)V_{pd\pi}$
$E_{xy,xy}$	$3l^2m^2V_{dd\sigma}+(l^2+m^2-4l^2m^2)V_{dd\pi}+(n^2+l^2m^2)V_{dd\delta}$
$E_{xy,yz}$	$3lm^2nV_{dd\sigma}+ln(1-4m^2)V_{dd\pi}+ln(m^2-1)V_{dd\delta}$
$E_{xy,zx}$	$3l^2mnV_{dd\sigma}+mn(1-4l^2)V_{dd\pi}+mn(l^2-1)V_{dd\delta}$
E_{xy,x^2-y^2}	$\frac{3}{2}lm(l^2-m^2)V_{dd\sigma}+2lm(m^2-l^2)V_{dd\pi}+\frac{1}{2}lm(l^2-m^2)V_{dd\delta}$
E_{yz,x^2-y^2}	$\frac{3}{2}mn(l^2-m^2)V_{dd\sigma}-mn\left(1+2(l^2-m^2)\right)V_{dd\pi}+mn\left(1+\frac{1}{2}(l^2-m^2)\right)V_{dd\delta}$
E_{zx,x^2-y^2}	$\frac{3}{2}nl(l^2-m^2)V_{dd\sigma}+nl\left(1-2(l^2-m^2)\right)V_{dd\pi}-nl\left(1-\frac{1}{2}(l^2-m^2)\right)V_{dd\delta}$
$E_{xy,3z^2-r^2}$	$\sqrt{3}lm\left[n^2-\frac{1}{2}(l^2+m^2)\right]V_{dd\sigma}-\sqrt{3}2lmn^2V_{dd\pi}+\frac{1}{2}\sqrt{3}lm(1+n^2)V_{dd\delta}$
$E_{yz,3z^2-r^2}$	$\sqrt{3}mn\left[n^2-\frac{1}{2}(l^2+m^2)\right]V_{dd\sigma}-\sqrt{3}mn(l^2+m^2-n^2)V_{dd\pi}-\frac{1}{2}\sqrt{3}mn(l^2+m^2)V_{dd\delta}$
$E_{zx,3z^2-r^2}$	$\sqrt{3}ln\left[n^2-\frac{1}{2}(l^2+m^2)\right]V_{dd\sigma}+\sqrt{3}ln(l^2+m^2-n^2)V_{dd\pi}-\frac{1}{2}\sqrt{3}ln(l^2+m^2)V_{dd\delta}$
$E_{x^2-y^2,x^2-y^2}$	$\frac{3}{4}(l^2-m^2)^2V_{dd\sigma}+[l^2+m^2-(l^2-m^2)^2]V_{dd\pi}+\left[n^2+\frac{1}{4}(l^2-m^2)^2\right]V_{dd\delta}$
$E_{x^2-y^2,3z^2-r^2}$	$\frac{1}{2}\sqrt{3}(l^2-m^2)\left[n^2-\frac{1}{2}(l^2+m^2)\right]V_{dd\sigma}+\sqrt{3}n^2(m^2-l^2)V_{dd\pi}+\frac{1}{4}\sqrt{3}(1+n^2)(l^2-m^2)V_{dd\delta}$
$E_{3z^2-r^2,3z^2-r^2}$	$\left[n^2-\frac{1}{2}(l^2+m^2)\right]^2V_{dd\sigma}+3n^2(l^2+m^2)V_{dd\pi}+\frac{3}{4}(l^2+m^2)^2V_{dd\delta}$

2.4.4 Band Unfolding using K-Projection

In order to compare electronic band structures in varying supercells a projection onto the primitive 1x1 Brillouin zone is required. This k-projection is a method where the wavefunctions of the supercell are decomposed into linear combinations of Bloch states that are associated with the primitive unit cell [33]. This can be written as

$$\psi_k^S = \sum c_k \psi_k. \tag{2.77}$$

The supercell reciprocal lattice vector can be written as a linear combination of primitive supercell reciprocal lattice vectors or primitive cell reciprocal basis vectors if

$$G_s = \sum m_i B_i = \sum g_j b_j \tag{2.78}$$

where *m*, *B*, *b* are integers, primitive supercell reciprocal lattice vector, and primitive reciprocal lattice vector respectively. The term g_j can be written as

$$g_j = \sum m_i \left(B_i a_j\right). \tag{2.79}$$

where a_j is the primitive lattice vector. The weights associated with states in the supercell that correspond to states in the primitive cell enables someone to plot something more representative of what would be observed from experiments such as angle resolved photoemission spectroscopy (ARPES).

References

1. Novoselov, K. S., Geim, A. K., Morozov, S. V., Jiang, D., Zhang, Y., Dubonos, S. V., & Firsov, A. A. (2004). Electric Field Effect in Atomically Thin Carbon Films. *Science, 306*(5696), 666-669. doi:10.1126/science.1102896
2. Mak, K. F., Lee, C., Hone, J., Shan, J., & Heinz, T. F. (2010). Atomically Thin MoS2: A New Direct-Gap Semiconductor. *Physical Review Letters, 105*, 1-4. doi:10.1103/PhysRevLett.105.136805
3. Caldwell, J. D., Anderson, T. J., Culbertson, J. C., Jernigan, G. G., Hobart, K. D., Kub, F. J., . . . Gaskill, K. D. (2010). Technique for the Dry Transfer of Epitaxial Graphene onto Arbitrary Substrates. *ACS Nano, 4*, 1108-1114. doi:10.1021/nn901585p
4. Liu, Y., Weinert, M., & Li, L. (2012). Spiral Growth without Dislocations: Molecular Beam Epitaxy of the Topological Insulator Bi2Se3 on Epitaxial Graphene/SiC(0001). *Physical Review Letters, 108*, 1-5. doi:10.1103/PhysRevLett.108.115501
5. Liu, Y., Li, Y. Y., Rajput, S., Gilks, D., Lari, L., Galindo, P. L., . . . Li, L. (2014). Tuning Dirac states by strain in the topological insulator Bi2Se3. *Nature Physics, 10*, 294-299. doi:10.1038/NPHYS2898
6. Edwards Vacuum. (2023, 6 21). *RV Two Stage Rotary Vane Pumps*. Retrieved from Edwards: https://www.edwardsvacuum.com/en-us/our-products/oil-sealed-pumps/rv-rotary-vane
7. VAC AERO International. (2023, 6 21). *Oiled Sealed Rotary Vane Pumps*. Retrieved from VAC AERO International INC.: https://vacaero.com/information-resources/vacuum-pump-technology-education-and-training/195875-oil-sealed-rotary-vane-pumps.html
8. Agilent. (2023, 6 21). *Turbo Pumps: Turbo-V 1K-G Pump*. Retrieved from Agilent: https://www.agilent.com/en/product/vacuum-technologies/turbo-pumps-controllers/turbo-pumps/turbo-v-1k-g-pump
9. Scienta Omicron. (2023, 6 21). *Effusion Cells*. Retrieved from scientaomicron: https://scientaomicron.com/en/productDetailPages/products-solutions/thin-film-deposition/Effusion%20Cells
10. Mack, C. (2007). *Fundamental Principles of Optical Lithography: The Science of Microfabrication.* Hoboken, New Jersey: John Wiley & Sons, Ltd.
11. Agilent. (2023, 6 21). *Agilent 5400 AFM/SPM Data Sheet*. Retrieved from Agilent: https://www.agilent.com/cs/library/datasheets/public/5989-5842EN.pdf
12. National Institute of Standards and Technology. (2023, 6 21). *NIST*. Retrieved from Schematic of an Atomic Force Microscope: https://www.nist.gov/image/afmschematic
13. Suk, J. W., Kitt, A., Magnuson, C. W., Hao, Y., Ahmed, S., Swan, A. K., . . . Ruoff, R. S. (2011). Transfer of CVD-Grown Monolayer Graphene onto Arbitrary Substrates. *ACS Nano, 5*(9), 6916-6924. doi:10.1021/nn201207c
14. Nanoscience Instruments. (2023, 6 21). *Scanning Tunneling Microscopy*. Retrieved from nanoScience Instruments: https://www.nanoscience.com/techniques/scanning-tunneling-microscopy/
15. Rajput, S., Chen, M. X., Liu, L., Li, Y. Y., Weinert, M., & Li, L. (2013). Spatial fluctuations in barrier height at the graphene–silicon carbide Schottky junction. *Nature Communications, 4*, 2752. doi:10.1038/ncomms3752

16. Tomer, D., Rajput, S., Hudy, L. J., Li, C. H., & Li, L. (2014). Intrinsic inhomogeneity in barrier height at monolayer graphene/SiC Schottky junction. *Applied Physics Letters, 105*, 021607. doi:10.1063/1.4890405
17. Tomer, D., Rajput, S., Hudy, L. J., Li., C. H., & Li, L. (2015). Carrier transport in reverse-biased graphene/semiconductor Schottky junctions. *Applied Physics Letters, 106*, 173510. doi:10.1063/1.4919727
18. Tomer, D., Rajput, S., Hudy, L. J., Li., C. H., & Li, L. (2015). Inhomogeneity in barrier height at graphene/Si (GaAs) Schottky junctions. *26*(21), 215702.
19. Hohenberg, P., & Kohn, W. (1964). Inhomogeneous Electron Gas. *Physical Review, 136*, B964-B871. doi:https://doi.org/10.1103/PhysRev.136.B864
20. Kohn, W., & Sham, L. J. (1965). Self-Consistent Equations Including Exchange and Correlation Effects. *Physical Review, 140*, A1133-A1138. doi:https://doi.org/10.1103/PhysRev.140.A1133
21. Kohn, W. (1996). Density Functional and Density Matrix Method Scaling Linearly with the Number of Atoms. *Physical Review Letters, 76*, 3168-3171.
22. Perdew, J. P., & Zunger, A. (1981). Self-interaction correction to density-functional approximations for many-electron systems. *Physical Review B, 23*, 5048-5079. doi:https://doi.org/10.1103/PhysRevB.23.5048
23. Perdew, J. P., & Wang, Y. (1992). Accurate and simple analytic representation of the electron-gas correlation energy. *Physical Review B, 45*, 13244-13249. doi:https://doi.org/10.1103/PhysRevB.45.13244
24. Perdew, J. P. (1985). Accurate Density Functional for the Energy: Real-Space Cutoff of the Gradient Expansion for the Exchange Hole. *Physical Review Letters, 55*, 1665-1668. doi:https://doi.org/10.1103/PhysRevLett.55.1665
25. Perdew, J. P., Burke, K., & Ernzerhof, M. (1996). Generalized Gradient Approximation Made Simple. *Physical Review Letters, 77*, 3865-3868. doi:https://doi.org/10.1103/PhysRevLett.77.3865
26. VASP Software GmbH. (2023, 07 10). *The Vienna Ab initio Simulation Package: atomic scale materials modelling from first principles.* Retrieved from VASP: https://www.vasp.at/
27. Wang, Q. H., Kalantar-Zadeh, K., Kis, A., Coleman, J. N., & Strano, M. S. (2012). Electronics and optoelectronics of two-dimensional transition metal dichalcogenides. Nature Nanotechnology, 7, 699-712. doi:10.1038/NNANO.2012.193
28. Manzeli, S., Ovchinnikov, D., Pasquier, D., Yazyev, O. V., & Kis, A. (2017). 2D transition metal dichalcogenides. *Nature Reviews Materials, 2*, 1-15. doi:10.1038/natrevmats.2017.33
29. Jackson, J. D. (1999). Classical Electrodynamics (3rd ed.). Hoboken, New Jersey: John Wiley & Sons, Inc.
30. VASP. (2023, 07 10). *VASP: Dielectric response Perturbation theory, linear response, and finite electric fields*. Retrieved from NERSC: https://www.nersc.gov/assets/Uploads/VASP-lecture-Dielectric.pdf
31. Adler, S. L. (1962). Quantum Theory of the Dielectric Constant in Real Solids. *Physical Review, 126*, 413-420. doi:https://doi.org/10.1103/PhysRev.126.413
32. Slater, J. C., & Koster, G. F. (1954). Simplified LCAO Method for the Periodic Potential Problem. *Physical Review, 94*, 1498-1524. doi:https://doi.org/10.1103/PhysRev.94.1498

33. Chen, M. X., & Weinert, M. (2014). Revealing the Substrate Origin of the Linear Dispersion of Silicene/ Ag(111). *Nano Letters, 14*, 5189-5193. doi:https://doi.org/10.1021/nl502107v

Chapter Three Electronic Properties of Graphene

Since graphene's isolation and publication of its electric field effect by Novoselov and Geim [1], it has fueled research into graphene-based devices, 2 dimensional materials, as well as many other aspects of materials science [2,3]. This chapter covers the basic aspects of graphene's electronic properties as well as findings on polymer transferred graphene based Schottky devices.

3.1 Crystal Structure

Graphene is composed of carbon atoms on a hexagonal lattice, or commonly referred to as a honeycomb lattice. This crystal structure is pictured in Figure 3.1 a). The lattice vectors for this structure can be written as

$$\boldsymbol{a}_1 = \frac{a}{2}\left(3, \sqrt{3}\right) \tag{3.1}$$

$$\boldsymbol{a}_2 = \frac{a}{2}\left(3, -\sqrt{3}\right) \tag{3.2}$$

where a = 1.42 Å and the lattice constant is $\sqrt{3}a = 2.47$ Å . Each carbon has 3 nearest neighbors separated by 1.42 Å which is the carbon-carbon distance. The three nearest neighbor positions can be written as

$$\delta_1 = \frac{a}{2}\left(1, \sqrt{3}\right) \tag{3.3}$$

$$\delta_2 = \frac{a}{2}\left(1, -\sqrt{3}\right) \tag{3.4}$$

$$\delta_3 = -a(1,0). \tag{3.5}$$

The 6 next nearest neighbors can be written as

$$\delta_1{}' = \pm\boldsymbol{a}_1 \tag{3.6}$$

$$\delta_2{}' = \pm\boldsymbol{a}_2 \tag{3.7}$$

$$\delta_3' = \pm(\boldsymbol{a}_2 - \boldsymbol{a}_1). \tag{3.8}$$

The formula for the reciprocal lattice vectors can be found in any standard solid state [4] textbook and for graphene they are

$$\boldsymbol{b}_1 = \frac{2\pi}{3a}\left(1, \sqrt{3}\right) \tag{3.9}$$

$$\boldsymbol{b}_2 = \frac{2\pi}{3a}\left(1, -\sqrt{3}\right) \tag{3.10}$$

where they satisfy the condition that $b_i \cdot a_j = 2\pi\delta_{ij}$. The Brillouin zone for graphene is also hexagonal and is pictured in Figure 3.1 b). There are 4 key symmetry points in the BZ. They are Γ, K, K', and M which are pictured in Figure 3.1 b). 2 important points within graphene's BZ is the K and K' point which are referred to as the Dirac points. This is where many of the interesting properties of graphene stem from. In reciprocal space the K and K' points are

$$\boldsymbol{K} = \left(\frac{2\pi}{3a}, \frac{2\pi}{3\sqrt{3}a}\right) \tag{3.11}$$

$$\boldsymbol{K}' = \left(\frac{2\pi}{3a}, -\frac{2\pi}{3\sqrt{3}a}\right) \tag{3.12}$$

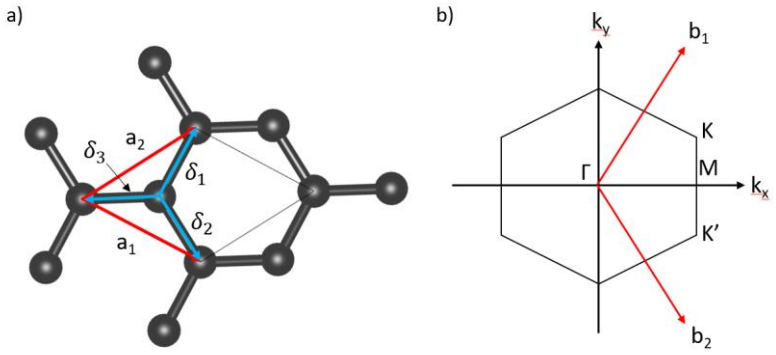

Figure 3.1. Graphene lattice, basis vectors, nearest neighbors, and Brillouin zone.

3.2 Electronic Band Structure

The electronic band structure of graphene is studied using density function theory and tight binding modeling. The band structure helps to highlight graphene's properties based on

its chemical composition and crystal structure. Graphene has a unique symmetry point, labelled the K point, where the energy dispersion is linear and the system has a vanishing density of states.

3.2.1 Density Functional Theory

The electronic band structure calculated using VASP is simple for graphene. Using the coordinates of the 2 carbon atoms for the unit cell and the pseudopotentials for carbon one can generate the band structure diagram pictured in Figure 3.2.

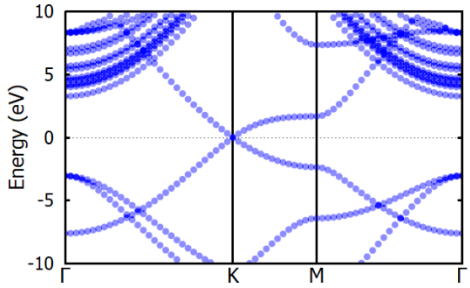

Figure 3.2. Energy bands for graphene generated using DFT

3.2.2 Tight Binding Approach

In order to solve the tight binding Hamiltonian, one needs to consider what orbitals play a more important role in the energy range you are interested in. For graphene, we have either the s or p orbitals to consider. The p_z orbitals are the main contributors to the bands around the Fermi level. Constructing a trial wavefunction that includes these orbitals and the two atoms within the unit cell, labeled a and b, we have

$$\psi_k = \sum_{\alpha,\beta} exp\big(i(\alpha \boldsymbol{k}\cdot\boldsymbol{a}_1 + \beta \boldsymbol{k}\cdot\boldsymbol{a}_2)\big)\Big(c_a\phi_{p_{za}}(\boldsymbol{r}-\alpha\boldsymbol{a}_1-\boldsymbol{\beta a}_2) + c_b\phi_{p_{zb}}(\boldsymbol{r}-\alpha\boldsymbol{a}_1-\boldsymbol{\beta a}_2)\Big). \quad (3.13)$$

We can then write the tight binding matrix as

$$\begin{bmatrix} \langle\phi_a|H|\phi_a\rangle - E & \langle\phi_a|H|\phi_b\rangle\sum_m e^{i\boldsymbol{k}\cdot\boldsymbol{\rho}_m} \\ \langle\phi_b|H|\phi_a\rangle\sum_m e^{-i\boldsymbol{k}\cdot\boldsymbol{\rho}_m} & \langle\phi_b|H|\phi_b\rangle - E \end{bmatrix}\begin{bmatrix} c_a \\ c_b \end{bmatrix} = 0 \quad (3.14)$$

where m is the summation over nearest neighbors. The determinant of the tight binding matrix will yield the energy eigenvalues of the system. This takes on the form

$$E(\boldsymbol{k}) = \varepsilon \pm t\sqrt{1 + 4cos\left(\frac{\sqrt{3}k_x a}{2}\right)cos\left(\frac{k_y a}{2}\right) + 4cos^2\left(\frac{k_y a}{2}\right)} \tag{3.15}$$

where the onsite energy ε and hopping energy t are defined as

$$\varepsilon = \langle\phi_a|H|\phi_a\rangle = E_p \tag{3.16}$$

$$t = -\langle\phi_a|H|\phi_b\rangle = V_{pp\pi}. \tag{3.17}$$

A plot of these energy bands are shown in Figure 3.3 a) where we can see that near the K point the bands are linear. These points are referred to as the Dirac points in this material because the energy dispersion mimics solutions to the Dirac equation.

Another common tight-binding Hamiltonian that considers nearest and next nearest neighbor atoms has the form given in [5]

$$H = -t\sum_{\langle i,j\rangle\sigma}\left(a^{\dagger}_{\sigma,i}b_{\sigma,j} + h.c.\right) - t'\sum_{\langle\langle i,j\rangle\rangle\sigma}\left(a^{\dagger}_{\sigma,i}a_{\sigma,j} + b^{\dagger}_{\sigma,i}b_{\sigma,j} + h.c.\right) \tag{3.18}$$

where ħ = 1, $a_{i\sigma}$, $b_{i\sigma}$, ($a^{\dagger}_{\sigma,i}$, $b^{\dagger}_{\sigma,i}$) annihilates (creates) an electron with spin σ on site $\mathbf{R_i}$ on sublattice *A*, *B*, *t* is the nearest neighbor hopping energy (~2.8 eV), and *t'* is the next nearest neighbor hopping energy. Energy bands for this Hamiltonian have been derived by Wallace [6] and are of the form

$$E_{\pm}(\boldsymbol{k}) = \pm t\sqrt{3 + f(\boldsymbol{k})} - t'f(\boldsymbol{k}) \tag{3.19}$$

where

$$f(\boldsymbol{k}) = 2cos\left(\sqrt{3}k_y a\right) + 4cos\left(\frac{\sqrt{3}}{2}k_y a\right)cos\left(\frac{3}{2}k_x a\right). \tag{3.20}$$

Wallace also showed that expanding the energy bands near the K or K' point takes on the form

$$E_{\pm}(\boldsymbol{q}) \approx \pm v_f|\boldsymbol{q}| + O[(q/K)^2] \tag{3.21}$$

where **q** is the momentum relative to the Dirac point, v_F is the Fermi velocity, $\approx 1x10^6$ m/s. This is done by writing k as k + δK, expanding f(**k**) in a Taylor series expansion, and letting $\varepsilon \to 0$ in the tight binding matrix. Wallace also showed that the Fermi velocity, $v_F = 3ta/2$, and it doesn't depend on the momentum as in the usual case, $v = k/m = \sqrt{2E/m}$.

A comparison of the bands generated using DFT and the tight-binding method are pictured in Figure 3.3 b). We can see that the tight-binding method does well in producing energy bands that have the same features as the energy bands generated using DFT. The same linear energy dispersion is represented near the Dirac point. A better comparison could be generated if the s and other p orbitals were included in the tight binding model as well as including beyond next nearest neighbors.

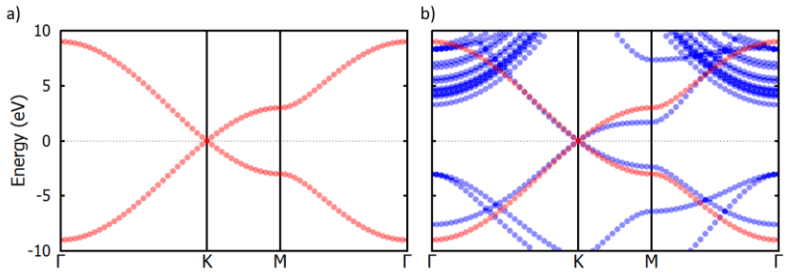

Figure 3.3. Energy band comparison of graphene. a) bands only consider p_z orbitals b) DFT bands using all orbitals

3.3 Density of States

The density of states is the number of orbitals per unit energy, or commonly known as the number of states per unit energy. We can write the number of states as

$$N = g\frac{\pi k_F^2}{(2\pi/L)^2} = g\frac{A}{4\pi}k_F^2 \tag{3.22}$$

where *g* is the degeneracy of the system, which is typically set to 2 for each spin of the electron, and A is the area of the unit cell. Near the Dirac points the energy has the form in equation 3.21, then we the number of states as

$$N = g\frac{A}{4\pi}\left(\frac{E}{v_F^2}\right)^2. \tag{3.23}$$

The density of states is defined as $n(E) = dN/dE$ [4], which we can then write as

$$n(E) = g\frac{A}{4\pi}\frac{E}{(\hbar v_F)^2} \tag{3.24}$$

We see that within graphene that the density of states formulation has a linear relationship in terms of energy differing from the typical energy dependence of a two-dimensional system,

$$n(E) = \frac{A}{2\pi}\frac{2m}{\hbar^2}. \tag{3.25}$$

A plot of the density of states for graphene is pictured in Figure 3.4 b) below. One can see that from Figure 3.4 b) in the density of states plot that the bands around the K point are only composed of p_z states. It is appropriate to use only p_z orbitals in the tight-binding model because those energy bands are dominated by those states. We can also see that the density states at the K point vanishes in Figure 3.4 b).

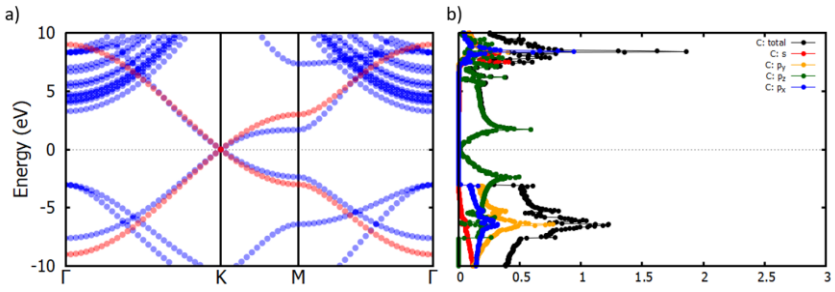

Figure 3.4. Graphene energy band plot along with the density of states

3.4 Electronic Transport Properties

Since the publication of the electric field effect in graphene [1], there has been much research in graphene-based devices that could possibly replace the current silicon-based technology. Initial work by Novoselov et al performed transport measurements on graphene measuring the temperature dependence of the carrier concentration as well as the field effect due to back gating the graphene films using the thin layer of SiO_2, ~300 nm, as a dielectric [1]. Figure 3.5 (D) adapted from Novoselov et al shows that graphene becomes more conducting as the temperature increases, increasing n means increasing σ because $\sigma = ne\mu$. Or to include both types of carriers we can write the conductivity as $\sigma = e(n\mu_e + p\mu_h)$, μ_e is the electron mobility and μ_h is the hole mobility. The conductivity as a function of temperature increases at a faster rate as the number of layers decrease [1]. We also see that the type of carriers, electrons or holes, can be controlled by the bias of the back gate in Figure 3.5 (C). These results show promise in terms of creating graphene-based devices. Schwierz wrote a review on graphene and its potential to be implemented as a field effect transistor (FET) [7]. He focuses on graphene-based devices that are extremely thin with short channels that can take advantage of graphene's large scattering times τ, or mean free path, which is related to the scattering time by $l = v_d\tau$ [7]. This means that the carriers operate in the ballistic regime [8]. Graphene-based devices will be more advantageous because these devices will also be smaller than current CMOS devices composed of silicon. Using small graphene devices such as nanoribbons not only decreases the size of the components but, it also opens the bandgap making these devices more suitable as logic devices [9].

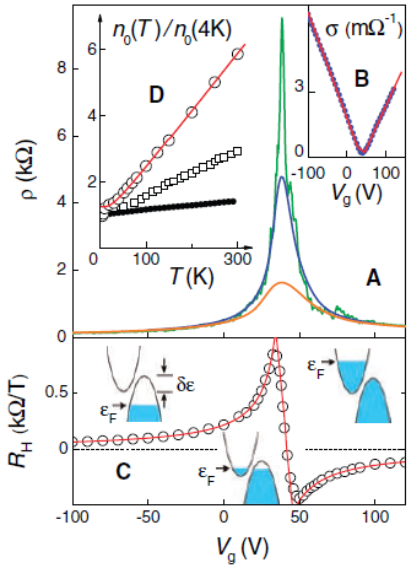

Figure 3.5. Field effect in graphene adapted from Novoselov et al [4]. A) Graphene resistivity as a function of gate voltage. B) Graphene conductivity as a function of gate voltage. C) Hall coefficient as a function of gate voltage at T = 5 K. D) Graphene carrier concentration as a function of temperature.

3.4.1 Graphene Schottky Diodes

Schottky diodes can be formed between the interface with graphene and other semiconductors. Tomer et al studied the formation of Schottky diodes formed with Graphene on SiC, Si, and GaAs under both forward and reverse bias [10-12]. The temperature dependent IV characteristics departed from the ideal Schottky diodes where the Schottky barrier height changed as a function of temperature suggesting a non-ideal Schottky junction. Rajput et al observed the spatial fluctuations of the barrier height of the polymer transferred graphene in the graphene-SiC Schottky junctions using STM/STS suggesting variations in the interface [13].

3.4.1.1 Schottky Diode Physics

A Schottky junction is formed at the metal-semiconductor interface [14]. This is due to the differences in work functions of the materials which forms a barrier called the Schottky barrier height and this can be written as [15]

$$\phi_B = \phi_M - \chi \tag{3.26}$$

where ϕ_B is the Schottky barrier height, ϕ_M is the metal work function and χ is the electron affinity of the semiconductor. When the materials come into contact, the Fermi level will normalize and reach equilibrium, causing the semiconductor bands to bend up or down depending on the semiconductor Fermi level with respect to the Fermi level within the metal. Figure 3.6 is the case where the Fermi level of the semiconductor is higher than the fermi level of the metal therefore the energy bands in the semiconductor will bend downwards to reach the equilibrium state. The Schottky barrier height is experienced by electrons going from the metal into states in the semiconductor. The electrons have to overcome this barrier in order to transfer into the semiconductor. The built in potential, V_{bi}, is the potential barrier seen by electrons that are going from the conduction band in the semiconductor into states within the metal. We can see that the built in potential can be written as

$$V_{bi} = \phi_M - \phi_S. \tag{3.27}$$

where ϕ_S is the work function of the semiconductor.

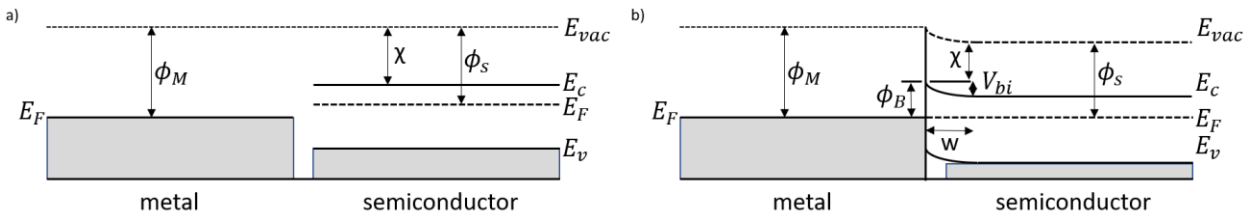

Figure 3.6. Energy bands of the metal-semiconductor interface. a) Energy bands of the isolated metal and semiconductor. b) energy bands after the metal and semiconductor become in contact and reach equilibrium.

3.4.1.1.1 Transport Mechanisms

There are four main mechanisms used in carrier transport in Schottky diodes. These are thermionic emission, quantum mechanical tunneling, electron-hole recombination in the depletion region, and hole injection from the metal to the semiconductor. Schottky junctions operate by the flow of the majority carriers and around room temperature, ~300 K, thermionic emission is the main transport mechanism where, the current density from the metal to semiconductor can be written as [15]

$$J_{S\to M} = C_1 N_C exp\left(-\frac{q\phi_B}{kT}\right). \tag{3.28}$$

C_1 is a constant and N_C is the density of states in the conduction band. Solving for the proportionality constant it can be shown that the IV characteristics for the metal-semiconductor interface under thermionic emission can be written as [15]

$$J = J_s\left(exp\left(\frac{qV}{kT}\right) - 1\right) \tag{3.29}$$

where

$$J_s = A^* T^2 exp\left(-\frac{q\phi_B}{kT}\right). \tag{3.30}$$

A^* is the Richardson constant and the current density has the typical exponential dependence, or rectifying behavior. The barrier height can be found by linearizing the saturation current as a function of temperature and relating the slope to the barrier height.

3.4.1.1.2 Spatial Inhomogeneity of Schottky Junctions Formed with Graphene

Samples using polymer transferred graphene have been shown to form ripples and ridges on the surface due to an imperfect contact with the substrate. This can be seen in AFM imagery pictured in Figure 2.9. These imperfections alter the Schottky barrier height creating a

distribution of barrier heights. At high enough temperatures, the majority carriers have energies that are larger than the Schottky barrier and these devices display the typical rectifying behavior. As the temperature decreases the majority carriers have less energy and require other modes of mechanism of transport. If there are also a distribution of barrier heights, then there are fewer channels where thermionic carriers can conduct. If we model the barrier as a Gaussian distribution, we can rewrite the barrier height as [16]

$$\phi_{B0} = \phi_{bm}(T = 0) - \frac{q\sigma_s^2}{2kT} \tag{3.31}$$

where σ_s is the zero bias standard deviation and ϕ_{bm} is the mean barrier height. This leads to the following saturation current density definition

$$J_s = A^* T^2 exp\left(-\left(\frac{q\phi_{bm}}{kT} - \frac{q^2\sigma_s^2}{2k^2T^2}\right)\right). \tag{3.32}$$

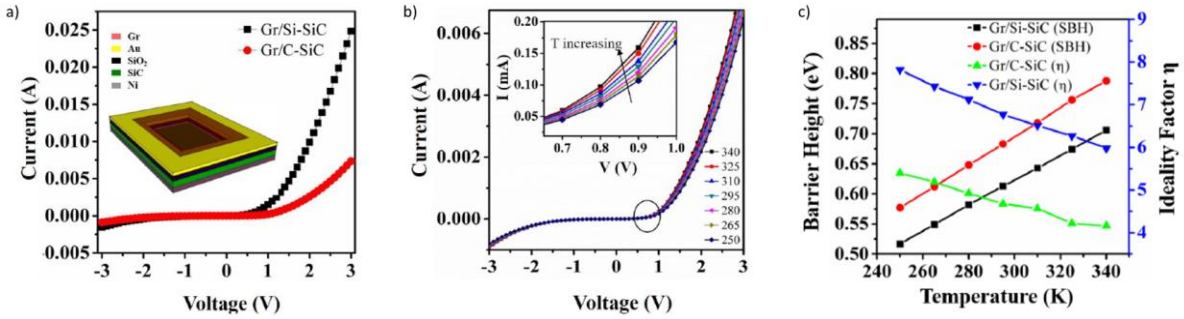

Figure 3.7. Graphene-SiC Schottky junction characteristics adapted from Tomer et al. [10]. a) IV characteristics (inset show device construction) b) IV temperature dependence. c) Barrier temperature dependence.

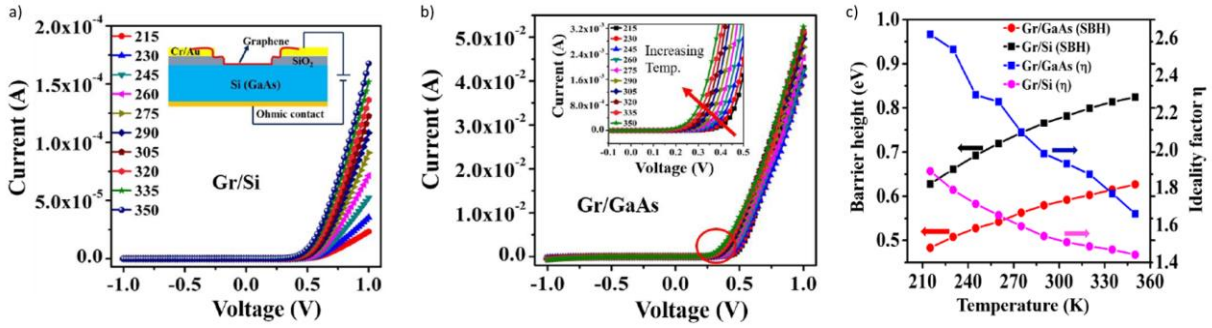

Figure 3.8. Graphene-Si Schottky junction characteristics adapted from Tomer et al. [11]. a) IV characteristics (inset show device construction) b) IV temperature dependence. c) Barrier temperature dependence.

Now fitting to the data above we see that there is a temperature dependence to the Schottky barrier height, meaning that the Schottky junction is not ideal in these systems. We can use a linear fit to the plots in Figures 3.7 c) and 3.8 c) to the barrier height temperature dependence to find the intrinsic Schottky barrier height. Overall, the linear fits perform well and the model of a Gaussian distribution of barrier heights explains the variation in the barrier height as a function of temperature.

References

1. Novoselov, K. S., Geim, A. K., Morozov, S. V., Jiang, D., Zhang, Y., Dubonos, S. V., . . . Firsov, A. A. (2004). Electric Field Effect in Atomically Thin Carbon Films. *Science, 306*(5696), 666-669. doi:10.1126/science.1102896
2. Ajayan, P., Kim, P., & Banerjee, K. (2016). Two-dimensional van der Waals materials. *Physics Today, 69*(9), 38-44. doi:https://doi.org/10.1063/PT.3.3297
3. Wang, S., Cui, X., Jian, C., Cheng, H., Niu, M., Yu, J., . . . Huang, W. (2021). Stacking-Engineered Heterostructures in Transition Metal Dichalcogenides. *Advanced Materials*, 1-21. doi:10.1002/adma.202005735
4. Kittel, C. (2005). *Introduction to Solid State Physics.* Hoboken, New Jersey: John Wiley & Sons, Inc.
5. Castro Neto, A. H., Guinea, F., Peres, N. M., Novoselov, K. S., & Geim, A. K. (2009). The electronic properties of graphene. *Reviews of Modern Physics, 81*, 109-162. doi:10.1103/RevModPhys.81.109
6. Wallace, P. R. (1947). The Band Theory of Graphite. *Physical Review, 71*(9), 622-634. doi:https://doi.org/10.1103/PhysRev.71.622
7. Schwierz, F. (2010). Graphene transistors. *Nature Nanotechnology, 5*, 487-796. doi:10.1038/nnano.2010.89
8. Mayorov, A. S., Gorbachev, R. V., Morozov, S. V., Britnell, L., Jalil, R., Ponomarenko, L. A., . . . Geim, A. K. (2011). Micrometer-Scale Ballistic Transport in Encapsulated Graphene at Room Temperature. *Nano Letters, 11*, 2396-2399. doi:dx.doi.org/10.1021/nl200758b
9. Han, M. Y., Özyilmaz, B., Zhang, Y., & Kim, P. (2007). Energy Band-Gap Engineering of Graphene Nanoribbons. *Physical Review Letters, 98*, 1-4. doi:https://doi.org/10.1103/PhysRevLett.98.206805
10. Tomer, D., Rajput, S., Hudy, L. J., Li, C. H., & Li, L. (2014). Intrinsic inhomogeneity in barrier height at monolayer graphene/SiC Schottky junction. *Applied Physics Letters, 105*, 021607. doi:10.1063/1.4890405
11. Tomer, D., Rajput, S., Hudy, L. J., Li., C. H., & Li, L. (2015). Inhomogeneity in barrier height at graphene/Si (GaAs) Schottky junctions. *26*(21), 215702.
12. Tomer, D., Rajput, S., Hudy, L. J., Li., C. H., & Li, L. (2015). Carrier transport in reverse-biased graphene/semiconductor Schottky junctions. *Applied Physics Letters, 106*, 173510. doi:10.1063/1.4919727
13. Rajput, S., Chen, M. X., Liu, L., Li, Y. Y., Weinert, M., & Li, L. (2013). Spatial fluctuations in barrier height at the graphene–silicon carbide Schottky junction. *Nature Communications, 4*, 2752. doi:10.1038/ncomms3752
14. Schottky, W. (1938). Halbleitertheorie der Sperrschicht. *Naturwissenschaften, 26*, 843.
15. Sze, S. M., & Lee, M. K. (2010). *Semiconductor Devices: Physics and Technology* (3rd ed.). New York: John Wiley & Sons, Inc.
16. Werner, J. H., & Güttler, H. H. (1991). Barrier inhomogeneities at Schottky contacts. *Journal of Applied Physics, 69*, 1522-1533. doi:https://doi.org/10.1063/1.347243

Chapter Four Electronic Properties of Transition Metal Dichalcogenides

With the discovery of graphene and its electronic field effect publication by Novoselov and Geim [1], there has been a push to investigate other van der Waals and two-dimensional materials [2-6]. Transition metal dichalcogenides are great candidates when it comes to designing new and interesting electronic devices considering that they are semiconducting, meaning that they have band gap unlike graphene, and they also typically transition to a direct band gap semiconductor in the monolayer form [2]. This chapter covers the basic electronic properties of transition metal dichalcogenides such as the energy band structure, its optoelectronic properties, as well as their transport properties.

4.1 Crystal Structure

Transition metal dichalcogenides are layered materials that are composed of stacks of transition metals sandwiched between chalcogen atoms. This can be seen in Figure 4.1 b) where the transition metal is colored blue and chalcogens are colored yellow. These stacks are loosely bound by van der Waals forces and the single layers can be isolated by mechanical exfoliation much like graphene. The monolayer lattice structure shares the same hexagonal symmetry as graphene except spin-orbit coupling plays a larger role in these materials. We can write the basis lattice vectors as

$$\boldsymbol{a}_1 = \frac{a}{2}\left(1, -\sqrt{3}\right) \tag{4.1}$$

$$\boldsymbol{a}_2 = \frac{a}{2}\left(1, \sqrt{3}\right) \tag{4.2}$$

where *a* is the lattice constant. The formula for the reciprocal lattice vectors can be found in any standard solid state [7] textbook and they are

$$\boldsymbol{b}_1 = \frac{2\pi}{3a}\left(3, -\sqrt{3}\right) \tag{4.3}$$

$$\boldsymbol{b}_2 = \frac{2\pi}{3a}\left(3, \sqrt{3}\right) \tag{4.4}$$

where they satisfy the condition that $b_i \cdot a_j = 2\pi\delta_{ij}$. There are 4 key symmetry points in the BZ. They are Γ, K, K', and M which are pictured in Figure 4.1 c). In reciprocal space we can write these 4 special symmetry points as

$$\Gamma = (0,0) \tag{4.5}$$

$$\mathrm{K} = \frac{1}{3}\boldsymbol{b}_1 + \frac{1}{3}\boldsymbol{b}_2 = \left(\frac{4\pi}{3a}, 0\right) \tag{4.6}$$

$$\mathrm{M} = \frac{1}{2}\boldsymbol{b}_2 = \frac{\pi}{3a}\left(3, \sqrt{3}\right) \tag{4.7}$$

$$\mathrm{K}' = -\frac{1}{3}\boldsymbol{b}_1 + \frac{2}{3}\boldsymbol{b}_2 = \frac{2\pi}{3a}\left(1, \sqrt{3}\right) \tag{4.8}$$

The six nearest neighbors can be written as

$$\delta_{\pm 1} = \left(0, \frac{a\sqrt{3}}{3}, \pm\alpha\right) \tag{4.9}$$

$$\delta_{\pm 2} = \left(-\frac{a}{2}, -\frac{a\sqrt{3}}{6}, \pm\alpha\right) \tag{4.10}$$

$$\delta_{\pm 3} = \left(\frac{a}{2}, -\frac{a\sqrt{3}}{6}, \pm\alpha\right). \tag{4.11}$$

where α is the distance in the *c* direction from the metal atom to the chalcogen.

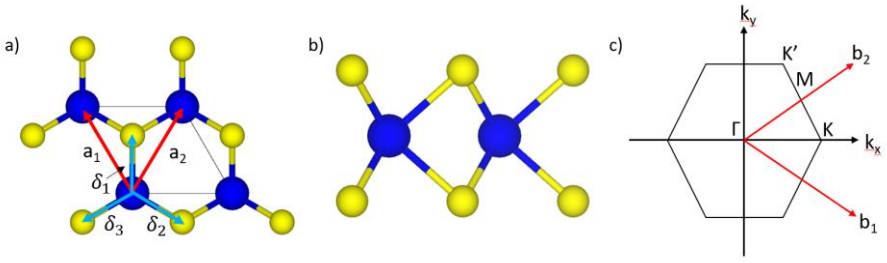

Figure 4.1. Transition metal dichalcogenides crystal structure and Brillouin zone. a) crystal structure viewed from c direction. b) crystal structure from a direction. c) Brillouin zone labeled with high symmetry points.

Now for the multilayer crystal structure, there is some variation in the stacking and orientation of the layers such as AA and AB stacked transition metal dichalcogenides. Below we are going to cover regular stacking where there is no twist applied between the layers. Chapter 5 will cover twisted transition metal dichalcogenide structures as well as their properties. Many of the TMDs can exist in both H and T type but their transport and optical responses differ based on their respective band structures.

4.1.1 H-Type AA Stacking Transition Metal Dichalcogenides

AA stacked transition metal dichalcogenide crystal structures have 3-fold rotation symmetry, a horizontal mirror plane, and a 2-fold rotational axis perpendicular to the principal axis thus belonging to the $\bar{6}m2$ Hermann-Manguin symmetry group, or D_{3h} in the Schoenflies notation. In this orientation the chalcogen atoms which are directly above each other result in breaking inversion symmetry in the system. Figure 4.2 a) shows the stacking of AA TMDs.

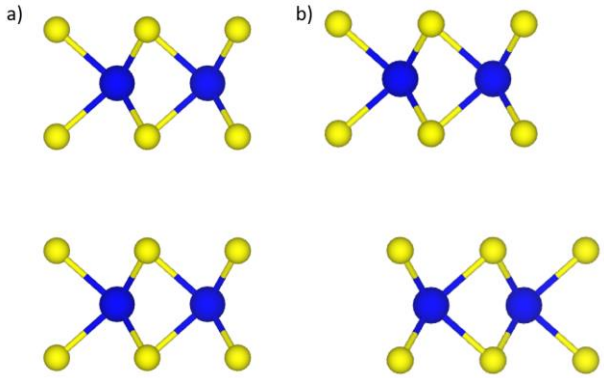

Figure 4.2. Layer stacking in transition metal dichalcogenides. a) AA stacking. b) AB stacking.

AA stacked transition metal dichalcogenides, where M = Mo, W and X = S, Se, Te, are usually semiconducting [2,8-10]. These TMDs typically have a band gap of 1-2 eV [2,8-10]. The broken inversion symmetry coupled with large spin orbit coupling results in the splitting of the energy bands typically at the valence band edge. The charge carriers can be labelled by the

valley degree of freedom of the two inequivalent K points, K and K', at the Brillouin zone edge. Bound states also exist between the electron hole pairs in the valence and conduction bands which are commonly referred to as excitons. Within TMDs, they typically have large binding energies because the monolayer or few layer materials do not have the same dielectric screening that is experienced within the bulk. In bilayer systems, this effect can be tuned based on the interaction between the layers.

AA stacked transition metal dichalcogenides, where M = Nb, Ta and X = S, Se, often display phenomenon such as superconductivity or charge density waves [8-10]. Their band structures are similar to the previous types, but they have less valence electrons and can only partially fill the bands near the Fermi level. Less is well understood between the relationship of the superconducting states and the charge density waves.

4.1.2 H-Type AB Stacking Transition Metal Dichalcogenides

AB stacked crystal structures are similar to H type AA stacked, but they also have inversion symmetry between the layers. This is pictured in Figure 4.2 b). This can be thought of as shifting the layer a half of a step to put the chalcogen in between each other similar to ABA stacking. These materials have similar properties to the AA stacked transition metal dichalcogenides. The interplay between charge density wave order and superconductivity still plays a key role [10,11]. The quantum spin hall effect has been reported in WTe_2 materials [12]. This effect along with superconductivity are the key components necessary for topological superconductivity and Majorana particles [11].

4.2 Electronic Band Structure

This dissertation is going to focus on a few of the transition metal dichalcogenides, primarily $MoSe_2$ and WSe_2, both in their monolayer and bilayer forms. The electronic band structures are generated using density functional theory and the tight-binding method. This dissertation will also compare the inclusion of spin-orbit coupling in these materials as it plays a larger role in breaking the degeneracy in the valence and conduction bands at K and K' thus splitting these spin bands when time reversal symmetry exist but inversion symmetry does not.

4.2.1 Spin-Orbit Coupling

Spin-orbit coupling can be thought of as adding a perturbation, specifically a relativistic effect, to the standard Hamiltonian where we include the interaction of the electron magnetic moment with an electric field. We can write this as [13]

$$H = H_0 + H_{S.O.} \tag{4.12}$$

where

$$H_{S.O.} = \frac{e^2}{2m^2c^2r^3}\boldsymbol{L}\cdot\boldsymbol{S}. \tag{4.13}$$

We can see that atoms with larger total angular momentum, typically heavier metal atoms, will have a larger spin-orbit effect. There is another type of spin-orbit effect that can take place in transition metal dichalcogenides which is the Rashba effect. Rashba spin-orbit coupling is an effect that is due to broken inversion symmetry which can be done using an external electric field. We can write this spin orbit coupling term as [14]

$$H_{S.O.} = -\mu_B\boldsymbol{\sigma}\cdot\left(\boldsymbol{p}\times\frac{\boldsymbol{E}}{2mc^2}\right) \tag{4.14}$$

where μ_B is the Bohr magneton, $\boldsymbol{\sigma}$ are the Pauli matrices, m is the effective mass of the carriers, and c is the speed of light. Not only does this effect split the bands at the corners of the Brillouin zone, but it also leads to interesting effects like the spin Hall effect and spin ballistic transport [15,16].

4.2.2 Density Functional Theory

The electronic band structure for these transition metal dichalcogenide systems were generated using VASP. The pseudopotentials used were the projected augmented wave (PAW) using the generalized gradient approximation along with the PBE exchange functional. The Monkhorst pack spacing was typically set to 18 x 18 x 1. There was also an approximate 30 Å vacuum between monolayers or bilayers to isolate those TMD systems. The lattice constant for $MoSe_2$ was set to 3.376 Å and the lattice constant for WSe_2 was set to 3.361 Å. These values were found by plotting the total energy, from a self-consistent DFT calculation, as a function of the lattice constant and finding the minimum of that function. Figure 4.3 shows the fits to find the lattice constant for $MoSe_2$ and WSe_2.

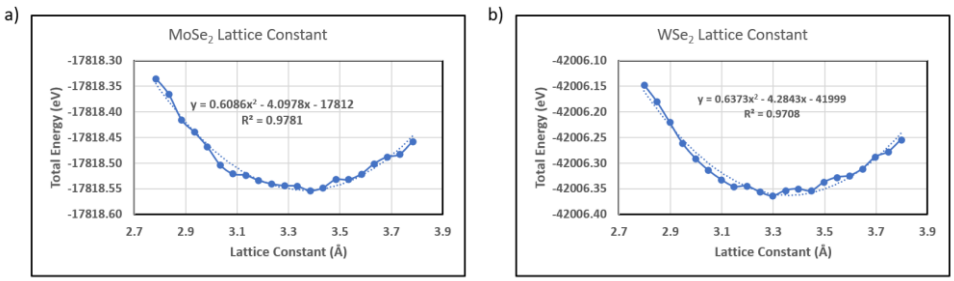

Figure 4.3. Total energy as a function of TMD lattice constants. a) $MoSe_2$ b) WSe_2

4.2.2.1 Monolayer Films

The monolayer films show a direct band gap with the following band gap energies, 1.55 eV ($MoSe_2$) and 1.64 eV (WSe_2), which is depicted in Figure 4.4. We can see that the direct

band gap occurs at the K and K' points in these materials. We also see that the spin-up and spin-down states are the same at K and K' meaning that they are degenerate without SOC.

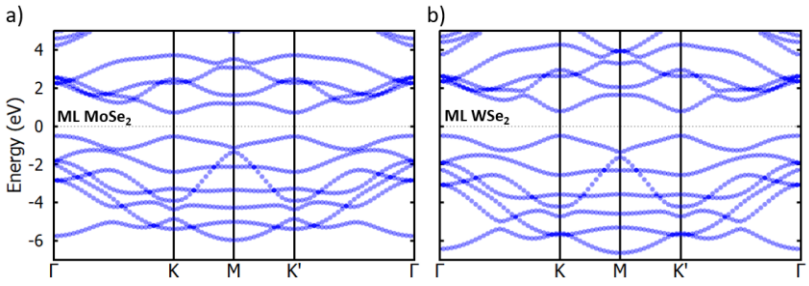

Figure 4.4. Monolayer TMD energy bands. a) $MoSe_2$ b) WSe_2

Including Spin-Orbit Coupling

Monolayer films with spin-orbit coupling, pictured in Figure 4.5, show minor ($MoSe_2$) to modest (WSe_2) splitting based on the transition metal dichalcogenide atoms. This difference in splitting is due to the larger tungsten atom in monolayer WSe_2. We also see that the larger splitting of the bands takes place near the valence band maximum around the K point. This is a result of a lack of inversion symmetry and the inclusion of spin-orbit coupling lifting the degeneracy of the spin states at the K and K' points.

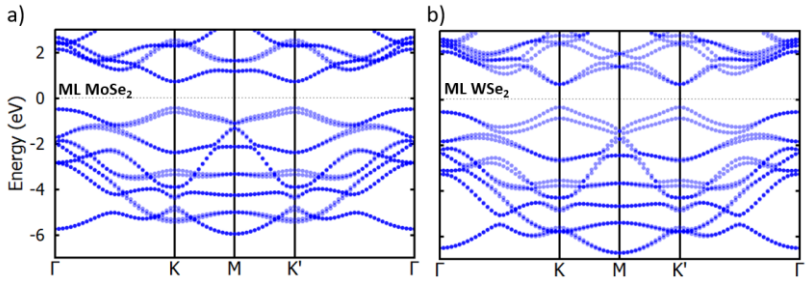

Figure 4.5. Monolayer TMD energy bands including spin-orbit coupling. a) $MoSe_2$ b) WSe_2

4.2.2.2 Bilayer Films

In the bilayer films, pictured in Figure 4.6, we see the transition from a direct band gap to an indirect one. This can be seen in Figure 4.6 for bilayer films composed of $MoSe_2$, WSe_2,

and $MoSe_2$-WSe_2 with the following band gaps 1.36 eV, 1.43 eV, and 0.84 eV respectively. The stacking also alters the bands slightly where we see larger splitting of the energy bands from K to M to K' around -2 eV for H type TMDs.

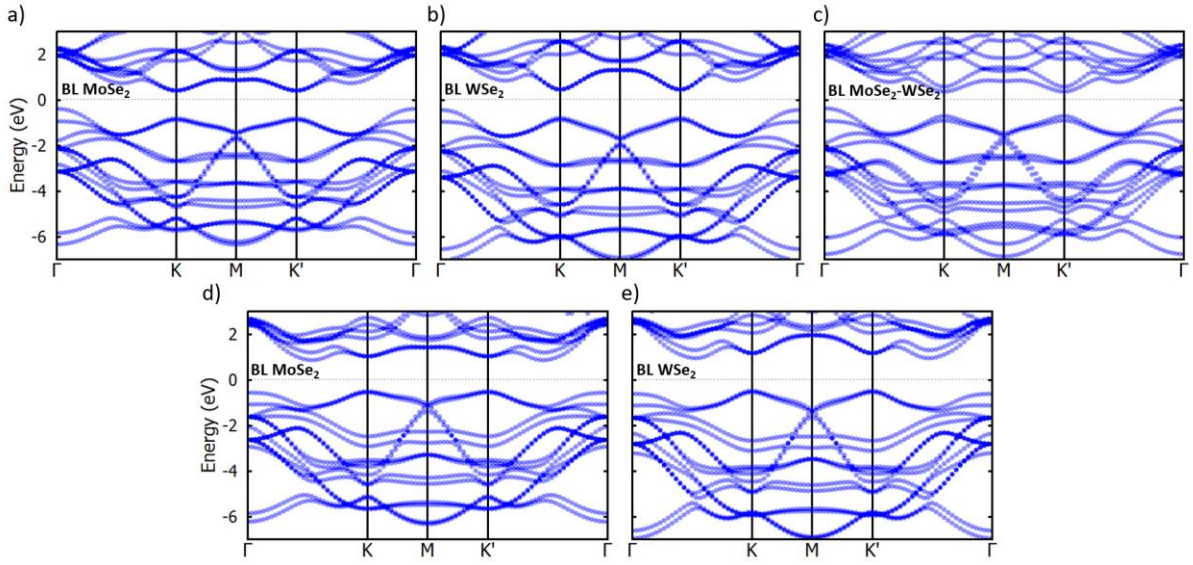

Figure 4.6. Bilayer TMD energy bands. a) AB stack $MoSe_2$ b) AB stack WSe_2 c) AB stack $MoSe_2$-WSe_2 d) AA stack $MoSe_2$ e) AA stack WSe_2

Including Spin-Orbit Coupling

Bilayer films with spin-orbit coupling show minor ($MoSe_2$) to modest (WSe_2) splitting based on the transition metal dichalcogenide atoms. This difference in splitting is due to the larger tungsten atom in monolayer WSe_2. We also see that the larger splitting of the bands takes place near the valence band maximum around the K and K' points. This is a result of the spin-orbit coupling lifting the degeneracy of the spin states at the K and K' points. Bilayer $MoSe_2$-WSe_2 seems to basically produce a linear combination of the monolayers in the energy bands but with slight differences because of the influence of other layer with the different metal atoms.

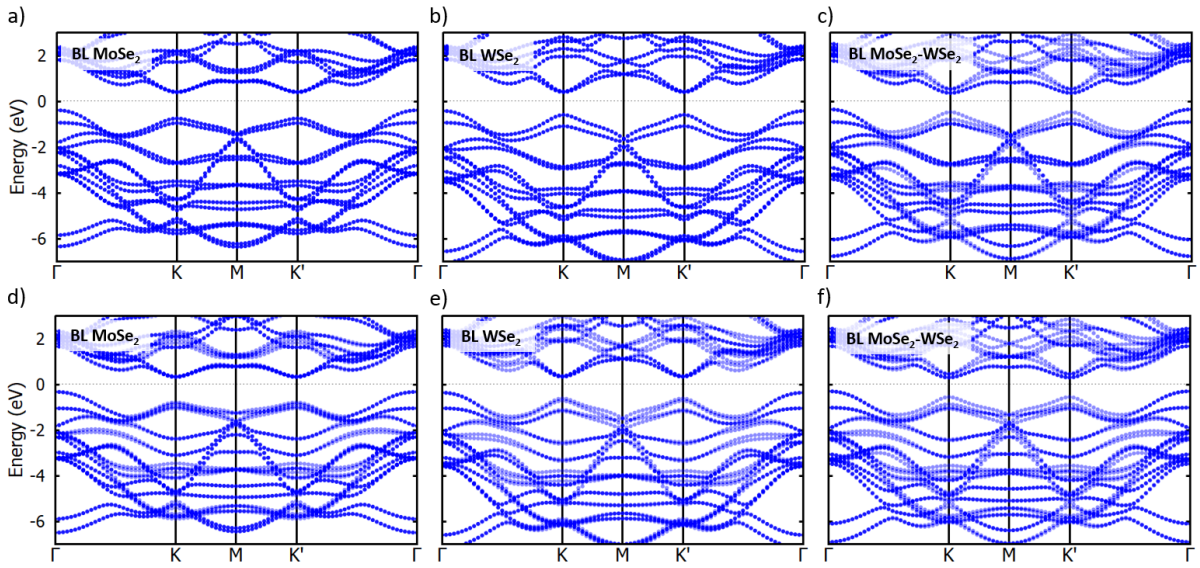

Figure 4.7. Bilayer TMD energy bands including spin-orbit coupling. a) AB stack $MoSe_2$ b) AB stack WSe_2 c) AB stack $MoSe_2$-WSe_2 d) AA stack $MoSe_2$ e) AA stack WSe_2 f) AA stack $MoSe_2$-WSe_2

4.2.3 Tight Binding Approach

The tight binding approach for transition metal dichalcogenides employs the following orbitals: p_x, p_y, and p_z for the chalcogen atoms and d_{xy}, d_{yz}, d_{zx}, d_{z^2}, and $d_{x^2-y^2}$ for the metal atoms similar to other approaches in [17]. Some initial tight-binding models that I worked on did not produce the best fitting bands and I also struggled to develop routines that could better fit the bands. It seemed that I kept finding local minima as opposed to the global minimum. A better fit routine would produce bands that align closer to the DFT bands like in Figure 4.9 for MoS_2 TMD films.

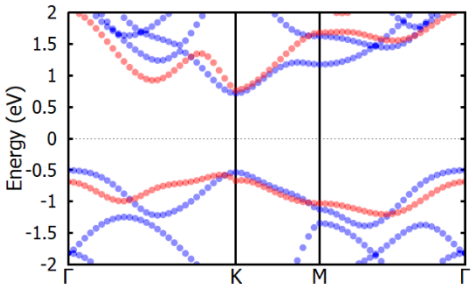

Figure 4.8. DFT bands along with tight binding bands for monolayer $MoSe_2$

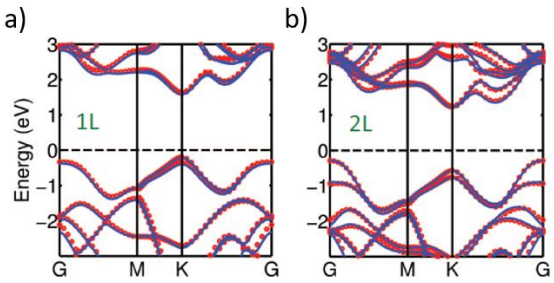

Figure 4.9. Tight binding bands fit to DFT data taken from Zahid et al. [18]. a) monolayer MoS_2 b) bilayer MoS_2

4.4 Density of States

The density of states for transition metal dichalcogenides helps to highlight some of these material's properties. We see that in the density of state plots in both the monolayer and bilayer films, there is a gap between the valence and conduction bands highlighting their semiconducting behavior. Another utility of the density of states is that you can look at the individual orbitals to see which ones contribute to which parts of the energy band structure. The partial density of states for the different TMD films are plotted in Figures 4.10 through 4.14.

4.4.1.1 Monolayer Films

In the monolayer films, pictured in Figures 4.10 and 4.11, we see the distribution of the density of states from the energy range of -7 eV to 5 eV. We also see the band gap of these materials where the DOS drops to 0. The composition of the states at the valence and conduction band edges has contributions from both the metal and chalcogen atoms, except the metal atoms seem to contribute more to these states. The main orbital contributing state seems to be the metal d_{z^2} at the conduction band edge and d_{xy} and $d_{x^2-y^2}$ at the valence band edge.

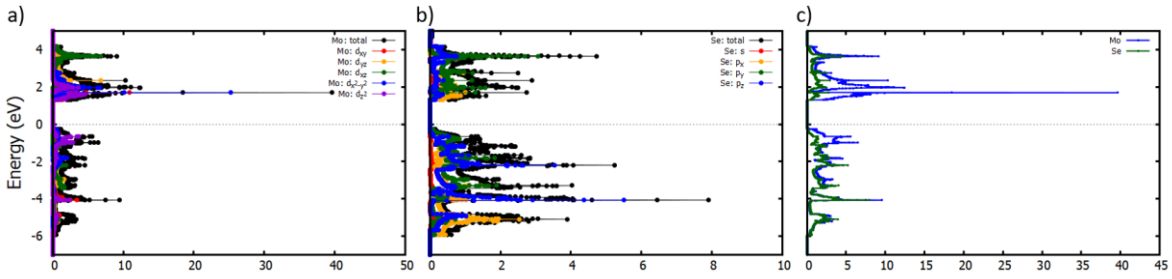

Figure 4.10. Density of states for monolayer $MoSe_2$. a) Mo partial density of states b) Se partial density of states c) total density of states

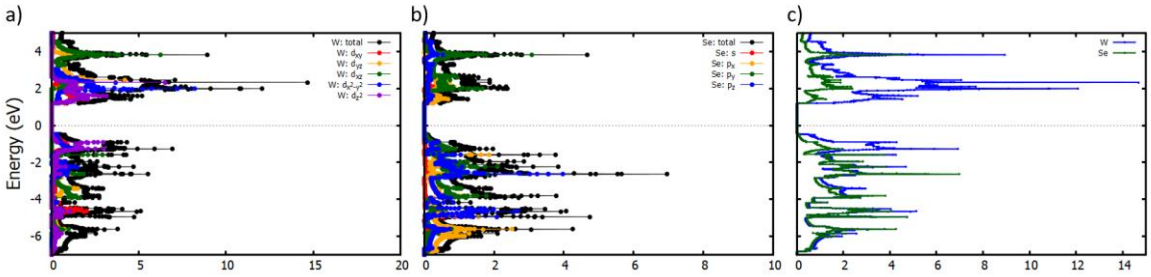

Figure 4.11. Density of states for monolayer WSe_2. a) W partial density of states b) Se partial density of states c) total density of states

4.4.1.2 Bilayer Films

In the bilayer films, pictured in Figures 4.12 through 4.14, we similar types of observations as in the monolayer films except that there seems to be more contribution from the d_{z^2} at valence band edge. There are also slight differences based on the bilayer stackings. It seems that at the valence band edge, the chalcogen atom has more p_z character in the AB stacking configuration.

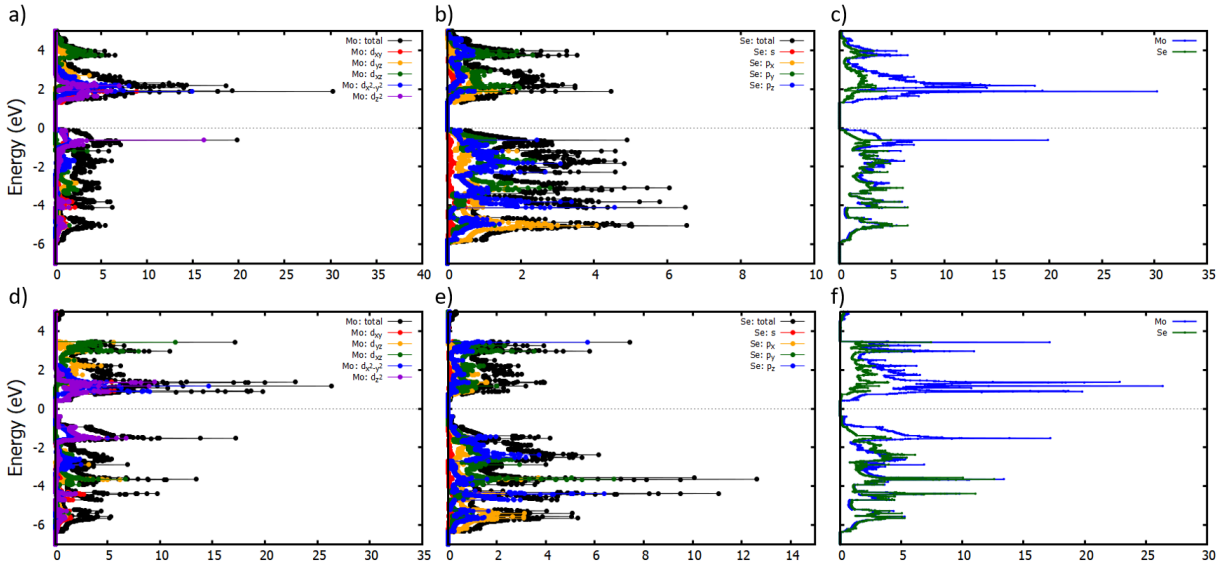

Figure 4.12. Density of states for bilayer $MoSe_2$. a) AA stack Mo partial density of states b) AA stack Se partial density of states c) AA stack total density of states d) AB stack Mo partial density of states e) AB stack Se partial density of states

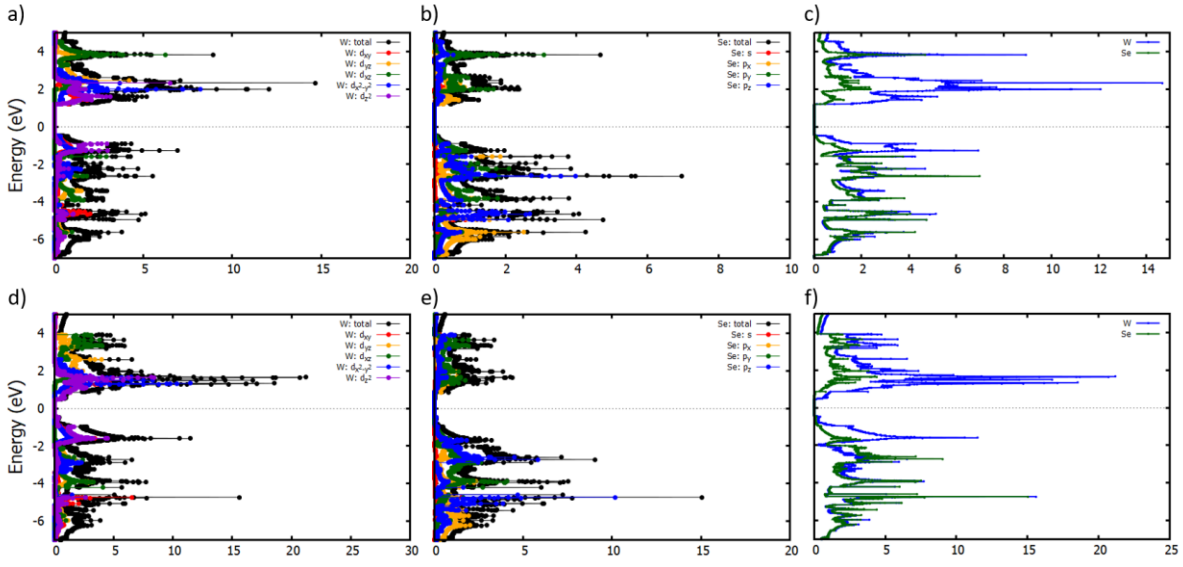

Figure 4.13. Density of states for bilayer WSe_2. a) AA stack W partial density of states b) AA stack Se partial density of states c) AA stack total density of states d) AB stack W partial density of states e) AB stack Se partial density of states f) AB stack total density of states

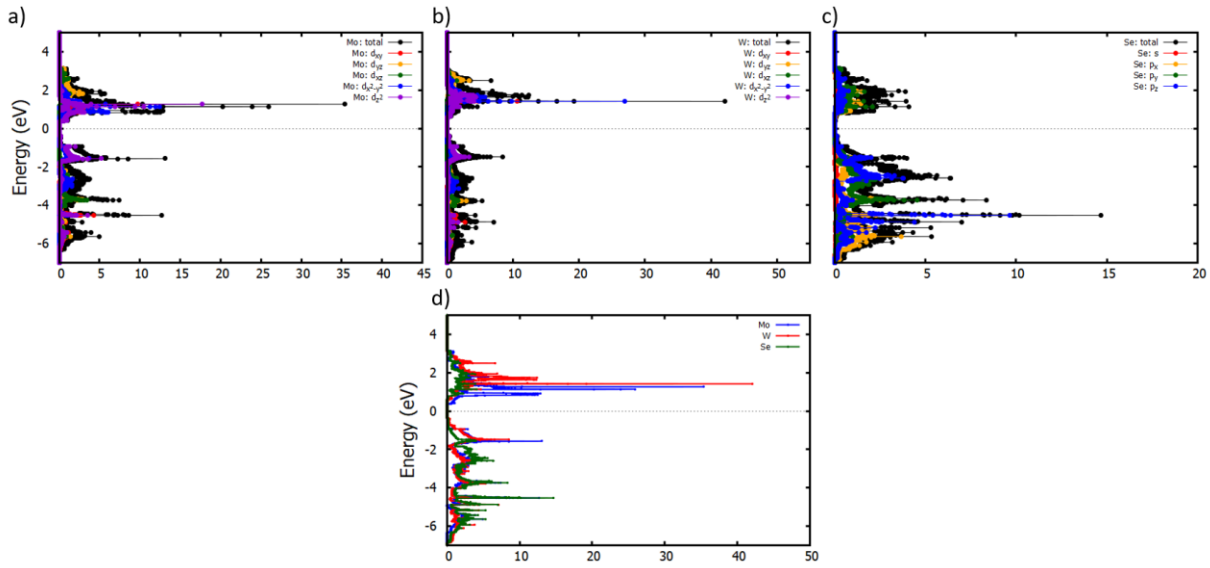

Figure 4.14. Density of States for Bilayer AA stacking $MoSe_2$-WSe_2. a) Mo partial density of states b) W partial density of states c) Se partial density of states d) total density of states

4.5 Charge Distribution

The charge distribution not only depends on factors such as the material but also on the energy range as well. The energy range determines the states of the atoms in the material that are available or can be excited. The charge distribution helps to highlight the states and their interaction in bonding or anti-bonding. Figure 4.15 shows the charge distribution of various TMD films in the energy range -1 eV ≤ E ≤ 0 eV. Notice that most films in this energy range are dominated by the metal d_{z^2} orbitals except AA stacked $MoSe_2$ where the orbital looks slightly different than the others.

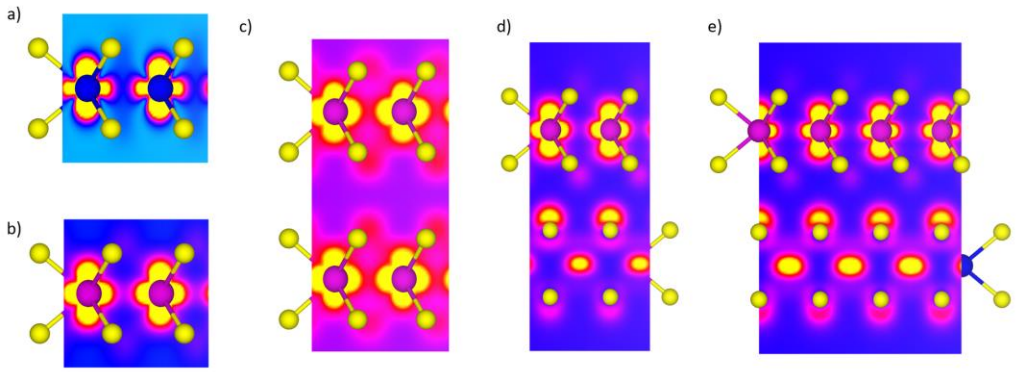

Figure 4.15. Charge distribution of TMD films. a) Monolayer WSe_2 b) Monolayer $MoSe_2$ c) AA stacked bilayer $MoSe_2$ d) AB stacked $MoSe_2$ e) AB stacked $MoSe_2$-WSe_2

4.6 Optical Properties

The optical properties we are primarily concerned with are ones where they can be manipulated into creating electronic devices. These optoelectronic devices can take advantage of the monolayer transition metal dichalcogenides direct band gap, meaning that only a photon with the correct energy can be absorbed or emitted. It has also been observed that at the direct transition circularly polarized light can be used to control the optical transitions [21,22]. The multilayer and bulk TMD structures can be used as well but also require an additional phonon with the correct momentum to transfer an electron from the valence band into the conduction band. In the case of monolayer MoS_2, the band gap not only shifts to a direct band gap but, it also increases in magnitude [2]. The two main components involved in any optoelectronic device are either absorption or emission of photons. TMDs are prime candidates for thin film solar cells, photodetectors, or light emitting diodes (LEDs) considering their direct band gap [23-25].

4.6.1 Excitons

Excitons are created when an electron is excited from a bound state into an excited state leaving a hole in its place. This electron-hole pair is what is referred to as an exciton. This happens when a material absorbs energy, e.g. a photon, and it excites an electron from the valence band to the conduction band creating an exciton from the electron-hole pair. These quasi-particles are useful in describing a material's optical properties because they have energy, momentum, characteristic lifetimes, and can be described using quantum theory. This can yield useful information about excitonic processes that take place such as diffusion or recombination.

4.6.2 Optical Conductivity

The optical conductivity and the dielectric function give information about a materials response to electromagnetic radiation. The real part of the dielectric function gives information about a material's ability to store and transmit electrical energy and the imaginary part relates to energy absorption or dissipation. These quantities are related by equation 2.63 which was derived in section 2.6. We would expect that large spikes in the density of states provide different levels for excited states to transition to, resulting in peaks in the dielectric function. Figures 4.16 and 4.17 display the dielectric function and conductivity for monolayer and bilayer $MoSe_2$, WSe_2, and $MoSe_2$-WSe_2.

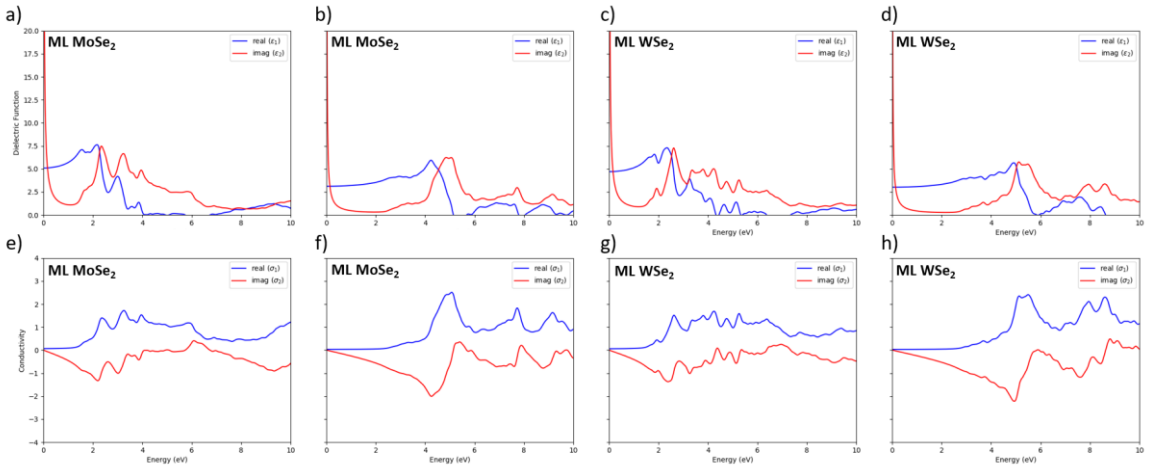

Figure 4.16. Dielectric function ϵ and conductivity σ for monolayer TMDs. a) ϵ_{xx} for monolayer $MoSe_2$ b) ϵ_{zz} for monolayer $MoSe_2$ c) ϵ_{xx} for monolayer WSe_2 d) ϵ_{zz} for monolayer WSe_2 e) σ_{xx} for monolayer $MoSe_2$ f) σ_{zz} for monolayer $MoSe_2$ g) σ_{xx} for monolayer WSe_2 h) σ_{zz} for monolayer WSe_2

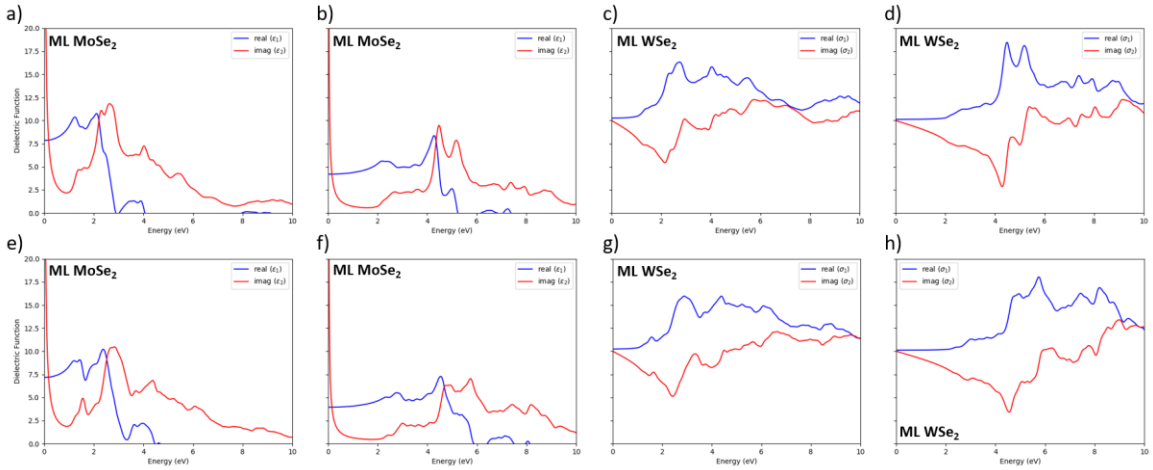

Figure 4.17. Dielectric function ϵ and conductivity σ for bilayer AB stack TMDs. a) ϵ_{xx} for bilayer $MoSe_2$ b) ϵ_{zz} for bilayer $MoSe_2$ c) ϵ_{xx} for bilayer WSe_2 d) ϵ_{zz} for bilayer WSe_2 e) σ_{xx} for bilayer $MoSe_2$ f) σ_{zz} for bilayer $MoSe_2$ g) σ_{xx} for bilayer WSe_2 h) σ_{zz} for bilayer WSe_2

4.6.3 Photoluminescence

Photoluminescence is a process where a material absorbs energy, typically light, then enters an excited state where it then decays back into the ground state emitting a photon. This process can happen directly between states or through other intermittent states until that excited state returns to the ground state. There is also a stronger photoluminescence response for few and monolayer TMDs compared with the bulk [1,9,19,20]. Figure 4.18 a) is a

photoluminescence plot of MoS_2 where we see a large peak corresponding to the band gap of monolayer MoS_2 as well as a comparison between layers pictured in Figure 4.18 b) adapted from the work done by Mak et al. [2].

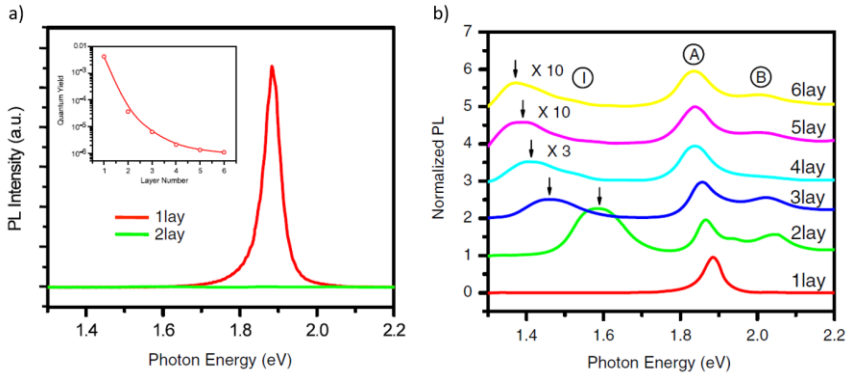

Figure 4.18. Photoluminescence response of MoS_2 adapted from Mak et al. [2] a) monolayer and bilayer comparison b) normalized photoluminescence for layer comparison.

4.7 Simulated Scanning Tunneling Microscopy

Theoretical scanning tunneling microscopy images can be produced using VASP by calculating the partial charge densities for a particular energy range. This can help highlight states around the valance or conduction band which can be tested experimentally. This can also be used to probe specific bands to determine the state composition of that band. Figure 4.19 is a sample STM of image of monolayer and bilayer $MoSe_2$, WSe_2, and $MoSe_2$-WSe_2. We see the typically hexagonal structure that we would expect. There also is very little difference in the STM between monolayer and bilayer films because STM is probing the surface.

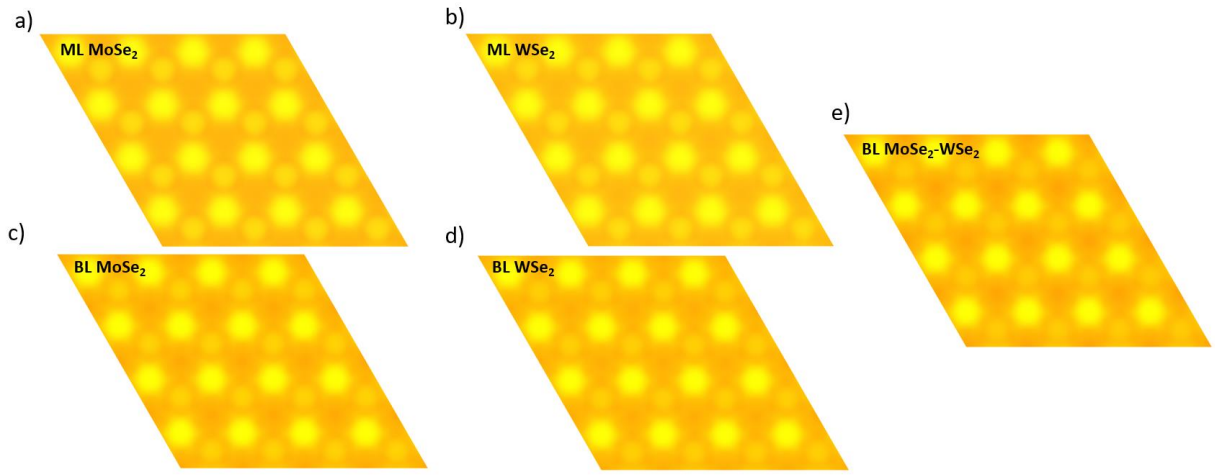

Figure 4.19. Simulated STM Imagery in the energy range -1 eV ≤ E ≤ 0 eV. a) monolayer $MoSe_2$ b) monolayer WSe_2 c) AB stacked bilayer $MoSe_2$ d) AB stacked bilayer WSe_2 e) AB stacked bilayer $MoSe_2$-WSe_2

4.8 Transport Properties

Several experiments using transition metal dichalcogenides as transistors have proven to be unsuccessful in producing devices with high mobilities compared to graphene [6,10,26,28]. This is because the TMD transistor charge carriers, specifically MoS_2, are heavily impacted by impurities as well as the dielectric environment [6,10,26]. Bare monolayer MoS_2 produced higher mobilities than ones encapsulated in a dielectric but, it still produced mobilities lower than that of bulk material [28]. Using a MoS_2 field effect transistor, the mobilities were enhanced by using a top gate but, the carrier mobility was still limited by impurity scattering [27,28]. The low carrier mobility can be attributed to Coulomb scattering from interfacial charge traps and phonon scattering limiting any TMD based logical device [10].

4.9 Defect States

Defects can occur when an impurity is absorbed on the surface, intercalated between the layers of a van der Waals material, or possibly though substitution. Interesting effects can take place when substitution occurs in a transition metal dichalcogenide film. It has been

shown that using another transition metal like copper can induce a large magnetic moment even though neither copper nor the TMDs possess [29,30].

4.9.1 Crystal Structure

The crystal structures used when adding an impurity as a replacement require larger supercells. This is because we want to ensure that the impurity does not interact with each other and, we essentially only want to add a small fraction of replacements with respect to the overall composition. Here we use $\sqrt{13}\ x\ \sqrt{13}$ supercells which an example is pictured in Figure 4.20 where the magenta atoms are metal, the green atoms are chalcogen, and the defect is pictured in orange. The black parallelogram is the supercell unit cell used for DFT calculations. We replaced the metal atoms with manganese, iron, and copper. As we go from to right in the periodic table from molybdenum or tungsten, we add more electrons to the system. In typical semiconductors like silicon, we can replace a small amount of the silicon with phosphorous doping the system with electrons raising the fermi level into the conduction band. This makes the material n-type with its majority carriers as electrons. We observe a different scenario in these TMD systems mainly because the band gap is too large to shift the Fermi level into the conduction band.

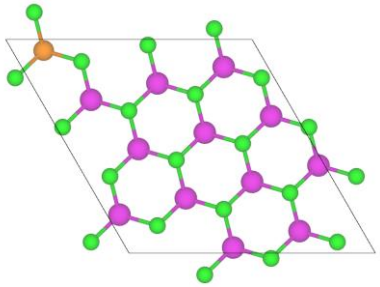

Figure 4.20. Crystal structure of a $\sqrt{13}\ x\ \sqrt{13}$ supercell consisting of monolayer $MoSe_2$ with a copper replacement.

4.9.2 Electronic Band Structure

The electronic band structure of copper doped transition metal dichalcogenides are pictured in Figures 4.21 – 4.22. We can see that the copper impurity adds flat states within the energy gap for both the monolayer and bilayer films. This also happens for the manganese and iron doped films. The energy bandwidth of the copper impurity states in the gap is on the order of 200 meVs. These states also lie at the Fermi level meaning that they are occupied or partially occupied.

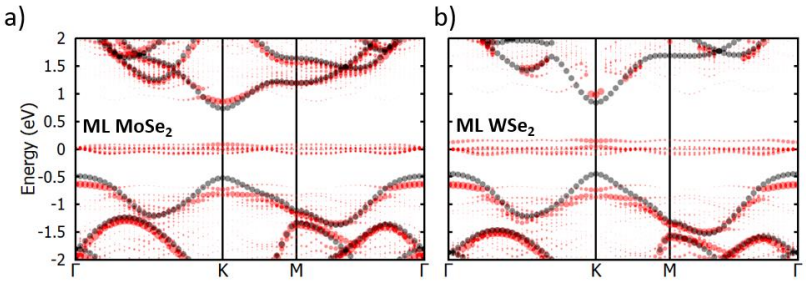

Figure 4.21. Unfolded electronic band structure of copper doped monolayer TMDs. a) $MoSe_2$ b) WSe_2

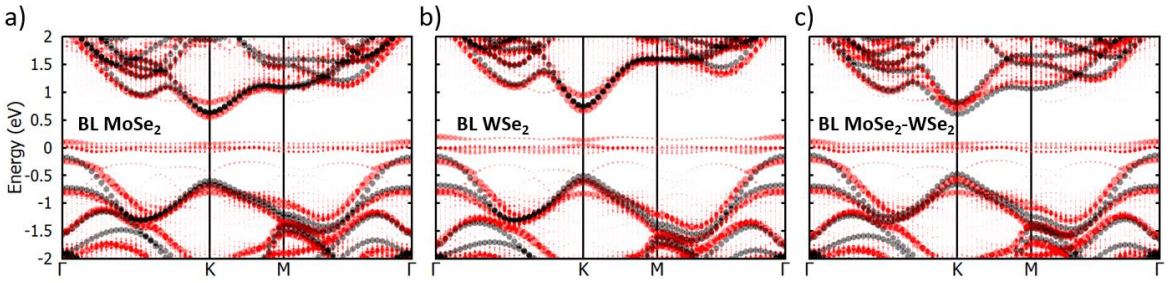

Figure 4.22. Unfolded electronic band structure of copper doped bilayer TMDs. a) $MoSe_2$ b) WSe_2 c) $MoSe_2$-WSe_2

Including Spin-Orbit Coupling

If we include spin-orbit coupling, we see a multitude of interesting things happen. The impurity bands in the gap for the materials split which is evident in Figures 4.23-4.25. We also notice that the bands around K and K' are no longer degenerate meaning that adding these impurities has broken a symmetry in these systems. From the spin polarized calculation in

VASP we see in the WSe_2 films doped with manganese, iron, and copper have a magnetic moment of 1.179, 2.031, and 4.098 μ_B respectively. We also added copper to monolayer $MoSe_2$ where we see a magnetic moment on the order of 2.484 μ_B. It would seem that the interaction between the copper and the tungsten atoms creates a larger moment in the material but something more complex must be taking place. This magnetic moment in this material breaks time reversal symmetry and thus breaks the degeneracy that exists at the K and K' points in these TMDs. This is evident in the energy band structures for monolayer and bilayer films with spin-orbit included where we see that the valence band maximum has shifted up in energy at the K point and down in energy at the K' point. If we measure the splitting at the valence band valleys, we see a splitting of 255, 286, and 128 meV for Mn, Fe, and Cu respectively. The measured splitting in the conduction bands are 26, 59, and 23 meV for Mn, Fe, and Cu respectively.

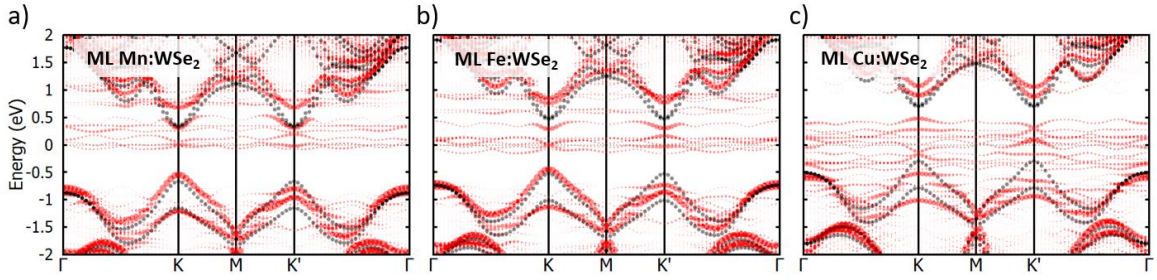

Figure 4.23. Unfolded electronic band structure of monolayer WSe_2 doped films. a) monolayer WSe_2 doped with Mn b) monolayer WSe_2 doped with Fe c) monolayer WSe_2 doped with Cu

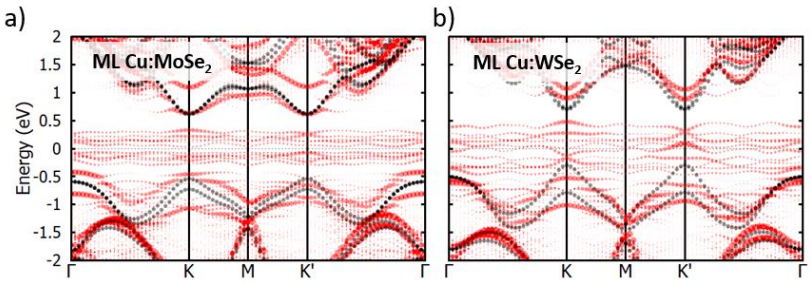

Figure 4.24. Unfolded electronic band structure of copper doped monolayer TMDs with spin-orbit interaction included. a) monolayer $MoSe_2$ b) monolayer WSe_2

When spin orbit-coupling is added to the copper doped bilayers we observe the following magnetic moment in these materials: 3.994 μ_B for bilayer $MoSe_2$, 3.438 μ_B for bilayer WSe_2, and 3.980 μ_B for bilayer $MoSe_2$-WSe_2. Interestingly we see that bilayer WSe_2 has a slightly smaller moment than bilayer $MoSe_2$ and $MoSe_2$-WSe_2 even though in the monolayer case we see that monolayer WSe_2 had a larger magnetic moment than monolayer $MoSe_2$. If we measure the splitting at the valence band valleys, we see a splitting of 181, 432, and 425 meV for $MoSe_2$, WSe_2, and $MoSe_2$-WSe_2 respectively.

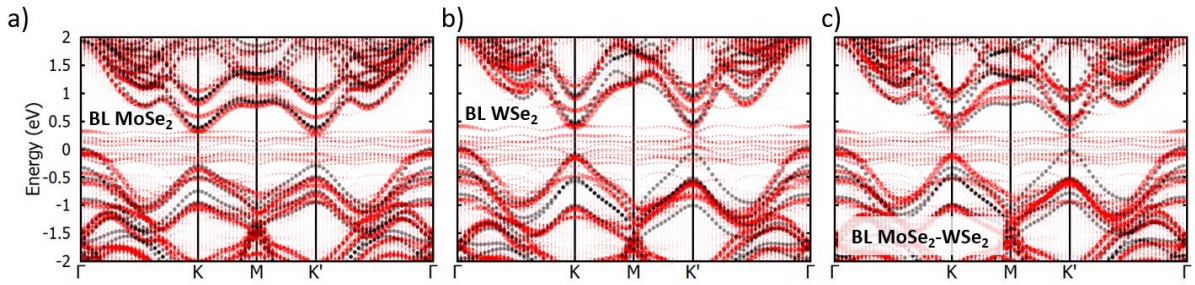

Figure 4.25. Unfolded electronic band structure of copper doped bilayer TMDs with spin-orbit interaction included. a) bilayer $MoSe_2$ b) bilayer WSe_2 c) bilayer $MoSe_2$-WSe_2

4.9.3 Density of States

We are going to focus on the density of states information for the copper doped films primarily because the behavior of the manganese and iron films show similar behavior but the copper doped films displaying a magnetic moment is more interesting. The density of states for monolayer transition metal dichalcogenides doped with copper are pictured in Figures 4.26 –

4.27. We can see that the composition of the flat states within the energy gap are composed of all the atoms in the material meaning that states from the copper dopant, metal atom, and chalcogen atoms all contribute to the flat states around the Fermi level.

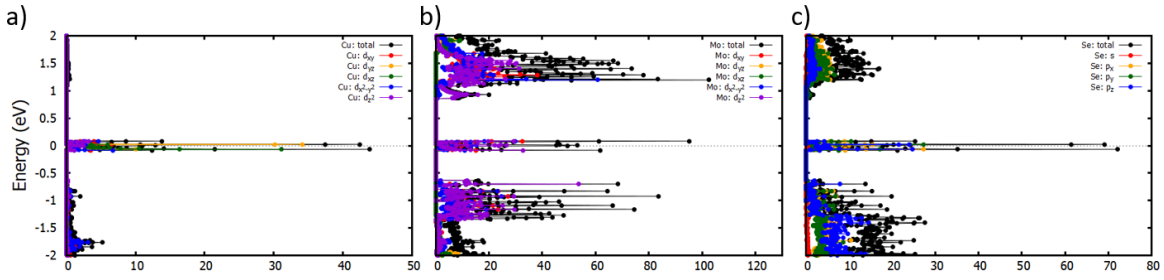

Figure 4.26. Density of states for copper doped monolayer $MoSe_2$ TMD films. a) Cu partial density of states b) Mo partial density of states c) Se partial density of states

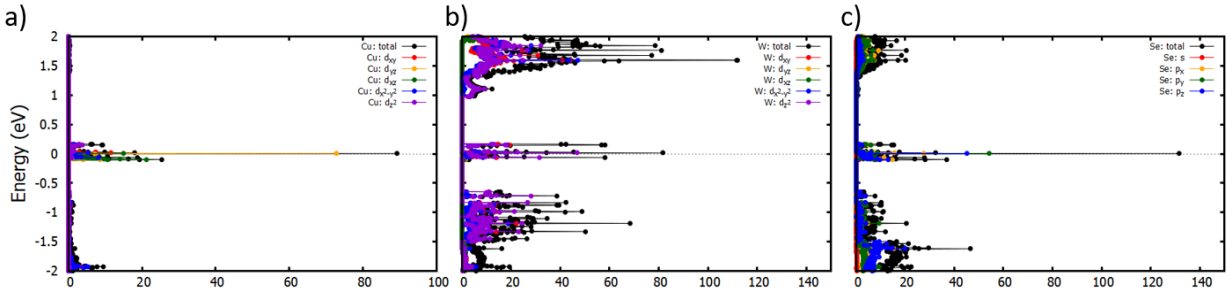

Figure 4.27. Density of states for copper doped monolayer WSe_2 TMD films. a) Cu partial density of states b) W partial density of states c) Se partial density of states

The density of states for bilayer transition metal dichalcogenides doped with copper are pictured in Figures 4.28 – 4.30. We can see a similar scenario that we see in the bilayer films where all the atoms contribute to the flat states within the gap except that there is almost no contribution from the tungsten atoms in bilayer $MoSe_2$-WSe_2.

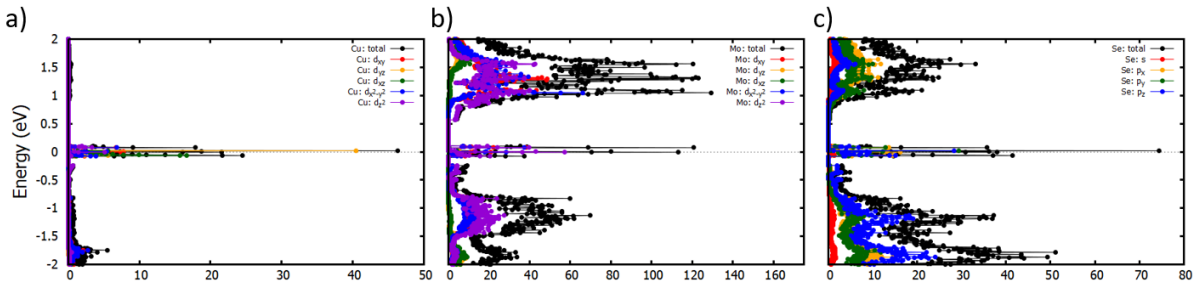

Figure 4.28. Density of states for copper doped bilayer $MoSe_2$ TMD films. a) Cu partial density of states b) Mo partial density of states c) Se partial density of states

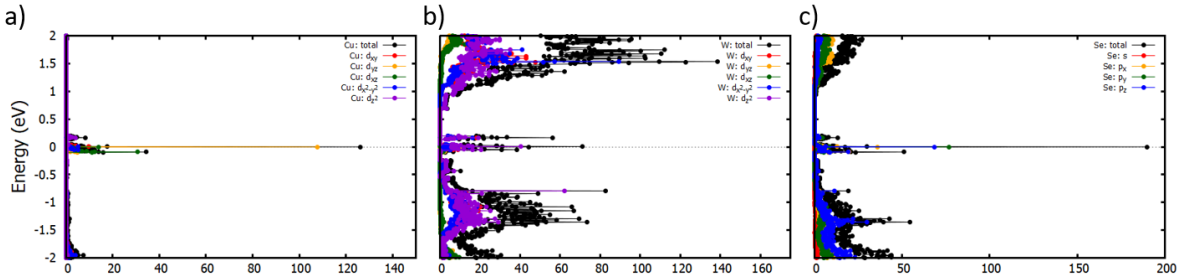

Figure 4.29. Density of states for copper doped bilayer WSe_2 TMD films. a)Cu partial density of states b) W partial density of states c) Se partial density of states

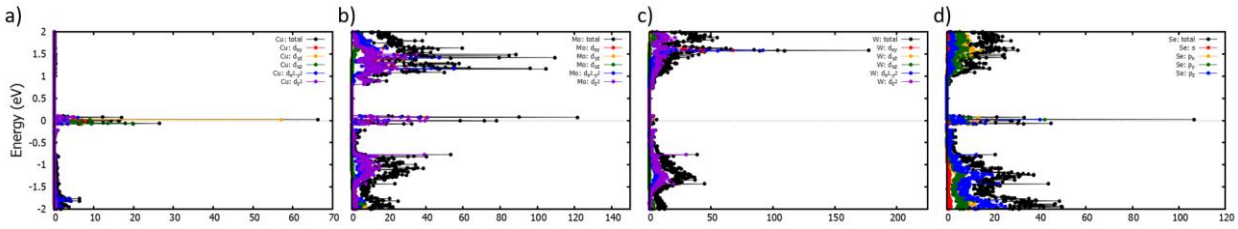

Figure 4.30. Density of states for copper doped bilayer $MoSe_2$-WSe_2 TMD films. a) Cu partial density of states b) Mo partial density of states c) W partial density of states d) Se partial density of states

Origin of the magnetic moment

If we try and investigate where this magnetic moment comes from, we could see if the spin resolved density of states can give us any insight. Magnetism can arise from 3 principal sources: the spin of an electron, their orbital angular momentum, and the change in orbital moment due to an applied field [7]. Looking at the spin resolved density of states in Figure 4.31 for monolayer WSe_2 doped with copper, we see that the filling of the electron levels according to Hund's rules leaves an unequal spin pairing below the Fermi level. This unequal pairing is

also seen in the films doped with manganese and iron but, those materials already show magnetic ordering. We attribute this unequal pairing to the reason why copper doped TMD films display a large magnetic moment. We also see that the magnetic moment for the copper doped films does not have an integer magnetic moment even though there are 5 unpaired electrons that copper can contribute. This is due to the fact that the energy levels of the spin up and spin down states are close and overlapping. As these states are filled up to the Fermi level results in a non-integer observed magnetic moment.

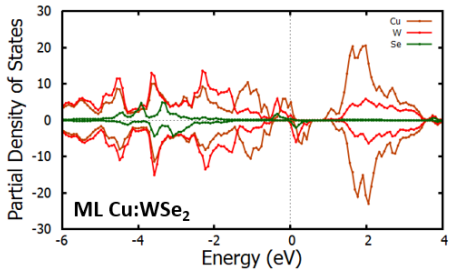

Figure 4.31. Spin resolved partial density of states for copper doped monolayer WSe_2.

4.9.4 Charge Distribution

The charge distribution for copper doped transition metal dichalcogenides is pictured in Figure 4.32. We can see the large contribution due to the copper atom for the states in the gap that are in the energy range of $0.2\ eV \leq E \leq 0.2\ eV$. Looking at the density states plot in the previous section we can see that there are contributions from the other atoms within the same layer but, the charge density shows that most of the charge contribution comes from the copper atom. This charge density also extends far beyond the copper atom in all directions.

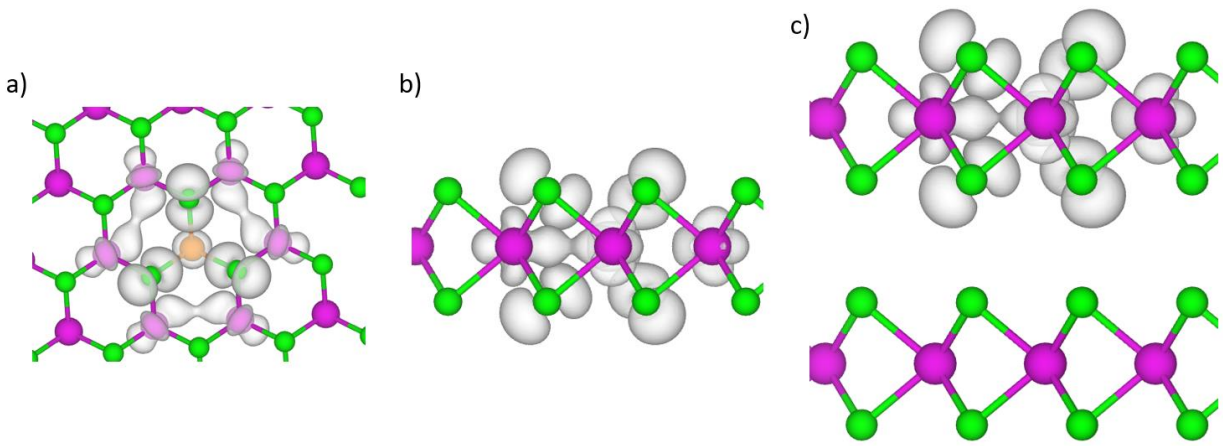

Figure 4.32. Charge distribution of copper doped TMDs where -0.2 eV ≤ E ≤ 0.2 eV. a) monolayer $MoSe_2$ viewed from the c-axis b) monolayer $MoSe_2$ viewed from the a-axis c) bilayer $MoSe_2$ viewed from the a-axis

4.9.5 Optical Properties

The interesting response from the copper doped transition metal dichalcogenides occurs because of the large magnetic moment that is produced when copper replaces one of the metal atoms. We can see from the optical responses that an off-diagonal component of the dielectric function has a non-zero value. This means that non-reciprocal behavior can take place in these materials where something like an applied field in one direction induces a current in a different direction. Most materials, including TMDs, do not have a non-zero off-diagonal component. This can lead to effects like second harmonic generation, frequency doubling, and other non-linear optical effects. Some of these effects can be functionalized into devices like an optical diode that can have current flow in only one direction because of the non-zero off-diagonal component.

Monolayer Films

The optical response for copper doped monolayer $MoSe_2$ is pictured in Figure 4.33 where we can see that off-diagonal component of the dielectric function, ϵ_{xy} and σ_{xy}, and

conductivity are non-zero. The peaks in these functions are smaller than their diagonal counterparts. We can also see that σ_{xy} conductivity has a response in the energy range that spans from 0 eV ≤ E ≤ 10 eV.

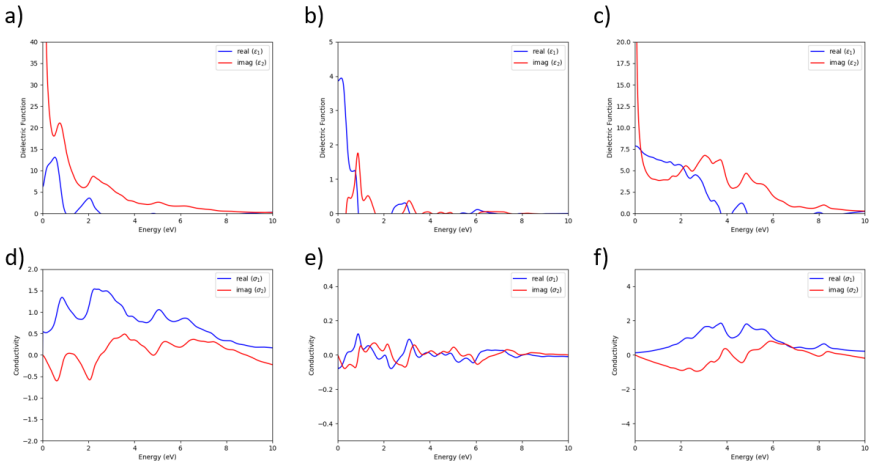

Figure 4.33. Dielectric function ϵ and conductivity σ for monolayer $MoSe_2$. a) ϵ_{xx} b) ϵ_{xy} c) ϵ_{zz} d) σ_{xx} e) σ_{xy} f) σ_{zz}

The optical response for copper doped monolayer WSe_2 is pictured in Figure 4.34. We have the same sort of behavior we see in monolayer $MoSe_2$ except that the response in the σ_{xy} conductivity is slightly stronger than in monolayer $MoSe_2$ but, it also does not span the entire energy range from 0 eV ≤ E ≤ 10 eV.

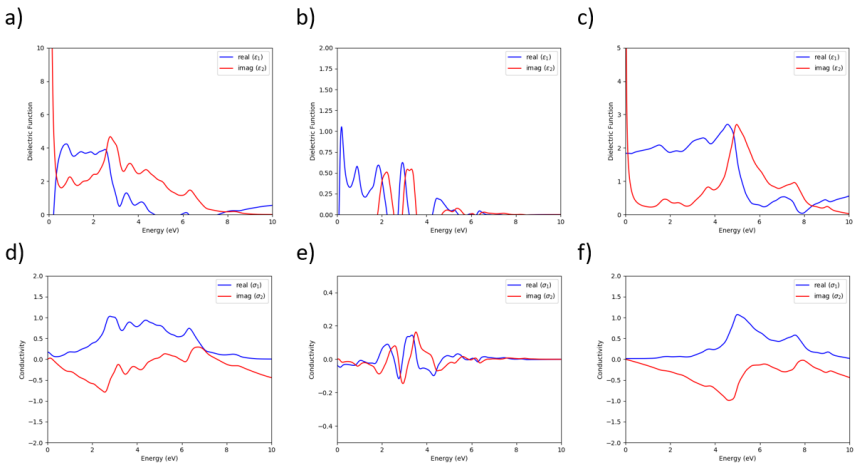

Figure 4.34. Dielectric function ϵ and conductivity σ for monolayer WSe_2. a) ϵ_{xx} b) ϵ_{xy} c) ϵ_{zz} d) σ_{xx} e) σ_{xy} f) σ_{zz}

Bilayer Films

The optical response for copper doped bilayer $MoSe_2$ is pictured in Figure 4.35. We see similar features that we do in the monolayer films except that the peaks in the off-diagonal component are smaller and shifted.

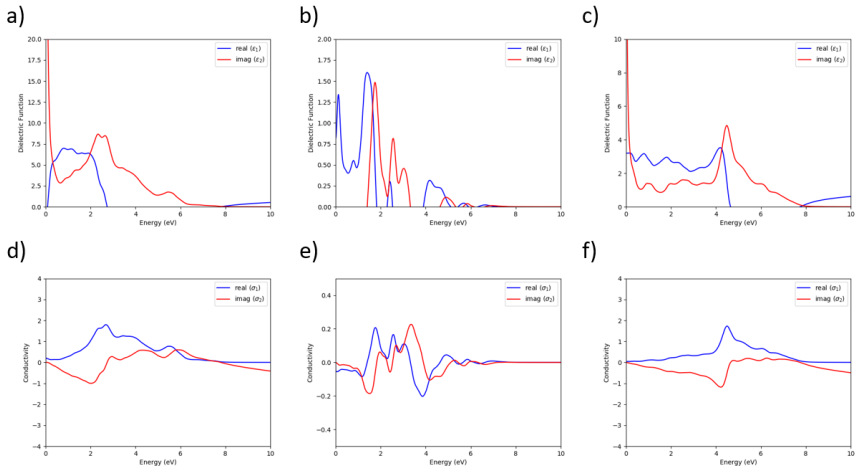

Figure 4.35. Dielectric function ϵ and conductivity σ for bilayer $MoSe_2$. a) ϵ_{xx} b) ϵ_{xy} c) ϵ_{zz} d) σ_{xx} e) σ_{xy} f) σ_{zz}

The optical response for copper doped bilayer WSe_2 is pictured in Figure 4.36. We see similar features as in the monolayer films except that the peak values have been enhanced showing a stronger response than its monolayer counterpart.

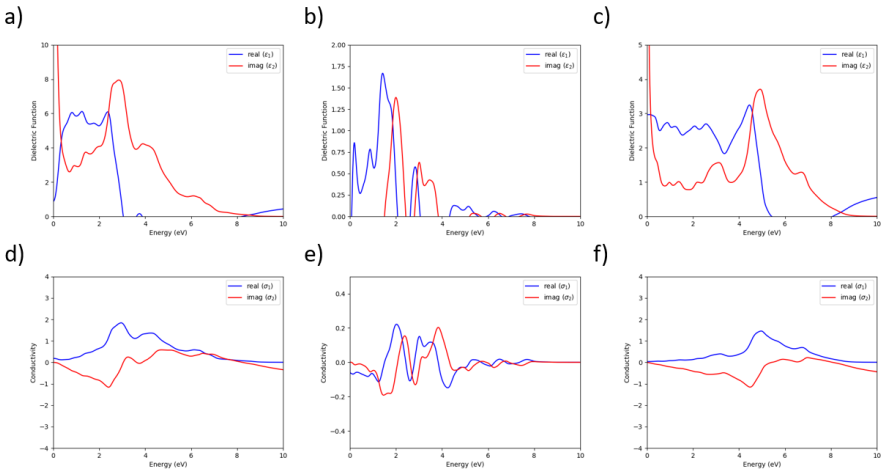

Figure 4.36. Dielectric function ϵ and conductivity σ for bilayer WSe_2. a) ϵ_{xx} b) ϵ_{xy} c) ϵ_{zz} d) σ_{xx} e) σ_{xy} f) σ_{zz}

The optical response for copper doped bilayer $MoSe_2$-WSe_2 is pictured in Figure 4.37. We can see that this response seems more similar to the bilayer WSe_2 films.

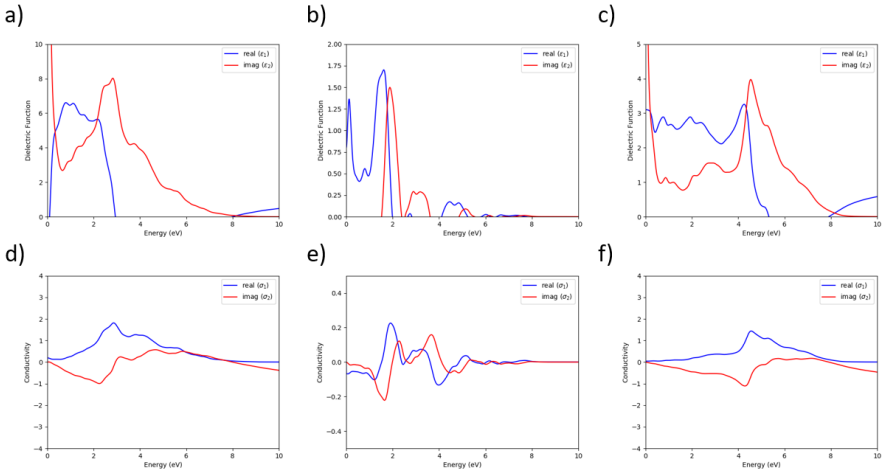

Figure 4.37. Dielectric function ϵ and conductivity σ for bilayer $MoSe_2$-WSe_2. a) ϵ_{xx} b) ϵ_{xy} c) ϵ_{zz} d) σ_{xx} e) σ_{xy} f) σ_{zz}

4.9.6 Simulated Scanning Tunneling Microscopy Imagery

The simulated scanning tunneling microscopy imagery for copper doped transition metal dichalcogenide films are pictured in Figure 4.38. We can see the large contribution from the copper orbitals that show up on the surface. There is a pronounced effect from the hybridization that takes place between the copper and chalcogen atoms. This effect seems to

be larger in WSe_2 than in $MoSe_2$. The simulated STM images are similar to what you see in the charge density and are dominated by the effect of adding the copper atom. What is interesting is when you place the copper atom in the bottom layer so that when imaging the surface, we still see effects of the replacement on the surface. This is pictured in 4.38 d) where the effect seems more pronounced than when the copper atoms are in the same layer.

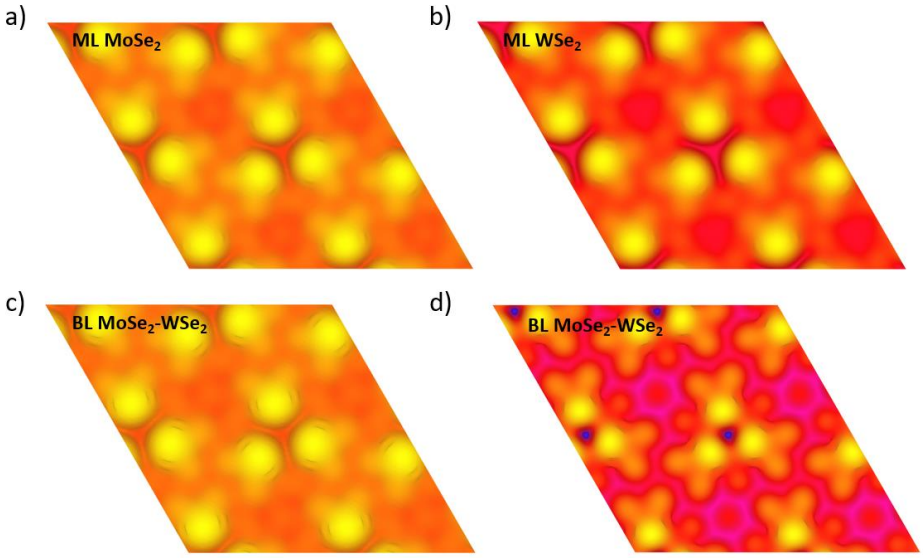

Figure 4.38. Simulated scanning tunneling microscopy imagery for copper doped TMDs in the energy range -0.2 eV ≤ E ≤ 0.2 eV. a) monolayer $MoSe_2$ b) monolayer WSe_2 c) bilayer $MoSe_2$-WSe_2 where the copper is in the Mo layer on top d) bilayer $MoSe_2$-WSe_2 where the copper is in the W layer in the bottom

References

1. Novoselov, K. S., Geim, A. K., Morozov, S. V., Jiang, D., Zhang, Y., Dubonos, S. V., . . . Firsov, A. A. (2004). Electric Field Effect in Atomically Thin Carbon Films. *Science, 306*(5696), 666-669. doi:10.1126/science.1102896
2. Mak, K. F., Lee, C., Hone, J., Shan, J., & Heinz, T. F. (2010). Atomically Thin MoS2: A New Direct-Gap Semiconductor. *Physical Review Letters, 105*, 1-4. doi:10.1103/PhysRevLett.105.136805
3. Schwierz, F. (2010). Graphene transistors. *Nature Nanotechnology, 5*, 487-796. doi:10.1038/nnano.2010.89
4. Podzorov, V., Gershenson, M. E., Kloc, C., Zeis, R., & Bucher, E. (2004). High-mobility field-effect transistors based on transition metal dichalcogenides. *Applied Physics Letters, 84*, 3301-3303. doi:https://doi.org/10.1063/1.1723695
5. Ayari, A., Cobas, E., Ogundadegbe, O., & Fuhrer, M. S. (2007). Realization and electrical characterization of ultrathin crystals of layered transition-metal dichalcogenides. *Journal of Applied Physics, 101*, 1-5. doi:https://doi.org/10.1063/1.2407388
6. Radisavljevic, B., Radenovic, A., Brivio, J., Giacometti, V., & Kis, A. (2011). Single-layer MoS2 transistors. *Nature Nanotechnology, 6*, 147-150. doi:10.1038/NNANO.2010.279
7. Kittel, C. (2005). *Introduction to Solid State Physics.* Hoboken, New Jersey: John Wiley & Sons, Inc.
8. Kuc, A., Zibouche, N., & Heine, T. (2011). Influence of quantum confinement on the electronic structure of the transition metal sulfide TS2. *Physical Review B, 8.*, 1-4. doi:https://doi.org/10.1103/PhysRevB.83.245213
9. Wang, Q. H., Kalantar-Zadeh, K., Kis, A., Coleman, J. N., & Strano, M. S. (2012). Electronics and optoelectronics of two-dimensional transition metal dichalcogenides. *Nature Nanotechnology, 7*, 699-712. doi:10.1038/NNANO.2012.193
10. Manzeli, S., Ovchinnikov, D., Pasquier, D., Yazyev, O. V., & Kis, A. (2017). 2D transition metal dichalcogenides. *Nature Reviews Materials, 2*, 1-15. doi:10.1038/natrevmats.2017.33
11. Zhou, B. T., Yuan, N. F., Jiang, H.-L., & Law, K. T. (2016). Ising superconductivity and Majorana fermions in transition-metal dichalcogenides. *Physical Review B, 93*, 1-5. doi:https://doi.org/10.1103/PhysRevB.93.180501
12. Tang, S., Zhang, C., Wong, D., Pedramrazi, Z., Tsai, H.-Z., Jia, C., . . . Shen, Z.-X. (2017). Quantum spin Hall state in monolayer 1T'-WTe2. *Nature Physics, 13*, 683-687. doi:10.1038/NPHYS4174
13. Shankar, R. (1994). *Principles of Quantum Mechanics* (2nd ed.). New York, New York: Springer.
14. Yuan, H., Bahramy, M. S., Morimoto, K., Wu, S., Nomura, K., Yang, B.-J., . . . Iwasa, Y. (2013). Zeeman-type spin splitting controlled by an electric field. *Nature Physics, 9*, 563-569. doi:10.1038/NPHYS2691
15. Murakami, S., Nagaosa, N., & Zhang, S.-C. (2003). Dissipationless Quantum Spin Current at Room Temperature. *301*, 1348-1351. doi:10.1126/science.1087128
16. Lu, J. P., Yau, J. B., Shukla, S. P., & Shayegan, M. (1998). Tunable Spin-Splitting and Spin-Resolved Ballistic Transport in GaAs/AlGaAs Two-Dimensional Holes. *Physical Review Letters, 81*, 1282-1285. doi:https://doi.org/10.1103/PhysRevLett.81.1282

17. Silva-Guillén, J. Á., San-Jose, P., & Roldán, R. (2016). Electronic Band Structure of Transition Metal Dichalcogenides from ab initio and Slater-Koster Tight-Binding Model. arXiv, 1-10. doi:https://doi.org/10.48550/arXiv.1611.04512
18. Zahid, F., Liu, L., Zhu, Y., Wang, J., & Guo, H. (2013). A generic tight-binding model for monolayer, bilayer and bulk MoS2. AIP Advances, 3, 1-6. doi:https://doi.org/10.1063/1.4804936
19. Splendiani, A., Sun, L., Zhang, Y., Li, T., Kim, J., Chim, C.-Y., . . . Wang, F. (2010). Emerging Photoluminescence in Monolayer MoS2. *Nano Letters, 10*, 1271-1275. doi:10.1021/nl903868w
20. Wang, X., Gong, Y., Shi, G., Chow, W. L., Keyshar, K., Ye, . . . Ajayan, P. M. (2014). Chemical Vapor Deposition Growth of Crystalline Monolayer MoSe2. *ACS Nano, 8*, 5125-5131. doi:10.1021/nn501175k
21. Xiao, D., Liu, G.-B., Feng, W., Xu, X., & Yao, W. (2012). Coupled Spin and Valley Physics in Monolayers of MoS2 and Other Group-VI Dichalcogenides. *Physical Review Letters, 108*, 1-5. doi:10.1103/PhysRevLett.108.196802
22. Cao, T., Wang, G., Han, W., Ye, H., Zhu, C., Shi, J., . . . Feng, J. (2012). Valley-selective circular dichroism of monolayer molybdenum disulphide. *Nature Communications, 3*, 1-5. doi:10.1038/ncomms1882
23. Yin, Z., Li, H., Li, H., Jiang, L., Shi, Y., Sun, Y., . . . Zhang, H. (2011). Single-Layer MoS2 Phototransistors. *ACS Nano, 6*, 74-80. doi:10.1021/nn2024557
24. Carladous, A., Coratger, R., Ajustron, F., Seine, G., Péchou, R., & Beauvillain, J. (2002). Light emission from spectral analysis of Au/MoS2 nanocontacts stimulated by scanning tunneling microscopy. *Physical Review B, 66*, 1-8. doi:https://doi.org/10.1103/PhysRevB.66.045401
25. Hwangbo, S., Hu, L., Hoang, A. T., Choi, J. Y., & Ahn, J.-H. (2022). Wafer-scale monolithic integration of full-colour micro-LED display using MoS2 transistor. *Nature Nanotechnology, 17*, 500-506. doi:https://doi.org/10.1038/s41565-022-01102-7
26. Novoselov, K. S., Jiang, D., Schedin, F., Booth, T. J., Khotkevich, V. V., Morozov, S. V., & Geim, A. K. (2005). Two-dimensional atomic crystals. *Proceedings of the National Academy of Sciences, 102*, 10451-10453. doi:https://doi.org/10.1073/pnas.0502848102
27. Fivaz, R., & Mooser, E. (1967). Mobility of Charge Carriers in Semiconducting Layer Structures. *Physical Review, 163*, 743-755. doi:https://doi.org/10.1103/PhysRev.163.743
28. Radisavljevic, B., & Kis, A. (2013). Mobility engineering and a metal–insulator transition in monolayer MoS2. *Nature Materials, 12*, 815-820. doi:10.1038/NMAT3687
29. Tedstone, A. A., Lewis, D. J., & O'Brien, P. (2016). Synthesis, Properties, and Applications of Transition Metal-Doped Layered Transition Metal Dichalcogenides. *Chemistry of Materials, 28*, 1965-1974. doi:10.1021/acs.chemmater.6b00430
30. Fan, X.-L., An, Y.-R., & Guo, W.-J. (2016). Ferromagnetism in Transitional Metal-Doped MoS2 Monolayer. *Nanoscale Research Letters, 11*, 1-10. doi:10.1186/s11671-016-1376-y

Chapter Five Electronic Properties of Twisted Transition Metal Dichalcogenides

Twisted transition metal dichalcogenides is a new emerging field of study based on work done on twisted bilayer graphene. Bilayer systems where a twist is applied between the layers creates a Moiré pattern and superlattice that can host exciting phenomenon. For small twist angles, these superlattice unit cells are extremely large and contain a large number of atoms. These superlattice unit cells are commensurate for only a specific set of twist angles. Twisted bilayer graphene displayed flat bands at the magic angle near 1° twist that led to the observation of superconductivity in those systems [1]. These flat bands lead to a high density of states where correlation effects can lead to different interesting phenomena such as superconductivity, mott insulators, magnetism and also but not limited to topological effects [1-5].

These discoveries have extended similar research into other two-dimensional van der Waals systems such as bilayer transition metal dichalcogenides [6-24]. Studies have shown spin-layer locking to exist in stacked TMD heterostructures [25,26]. More recent studies have shown flat bands and correlation effects in twisted TMD systems. Mit H. Naik and Manish Jain report results from a DFT study for twisted layers of MoS_2 where flat bands are observed at angles of 3.5° and 65.5° near the valance band edge [10]. Zhiming Zhang et al. report detecting flat bands in twisted TMDs consisting of homo-bilayers of WSe_2 at angles of 3° and 57.5° near the valence band as well. They determine the existence of flat bands by peaks in the dI/dV spectra, which are proportional to the DOS, and related to the wave functions of the flat band

states [6]. Shabani et al. created samples of twisted bilayers of $MoSe_2$ and WSe_2 and showed that at small angles a Moiré potential that describes the structural rippling and electronic coupling can store a significant amount of charge carries [7]. This Moiré potential is larger at the valence band and on the order of 300 meV [7]. They also argue that the interlayer strain is a more significant contributor to the Moiré potential [7]. These states created by the Moiré potential can be probed using optical experiments such as photoluminescence (PL) and Raman spectroscopy. Specifically in these PL experiments, they create intralayer and interlayer excitons and observe that twisting these bilayers typically decreases the intensities of the PL peaks as well as shifting their peak positions based on the level of interlayer interaction [11-14]. They also observe an increase in the lifetimes of these excitons because of twisting of these bilayers [11-14].

5.1 Crystal Structure

This dissertation covers the followings angles for the twisted bilayer transition metal dichalcogenide $MoSe_2$-WSe_2: 13.174°, 21.787°, 27.796°, 32.204°, 38.213°, and 46.826°. The twisted crystal structures are found based on methods outlined in chapter 2 section 2.4.1. The next subsections are going to go over the twisted crystal structure supercell, basis vectors, reciprocal lattice vectors and their relation to the primitive 1 x 1 hexagonal cells, as well as the high symmetry points in k-space for both the supercell and the primitive cell. These quantities help to compare the twisted band structures to the non-twisted ones. Figure 5.1 shows the standard non twisted $MoSe_2$-WSe_2 bilayer crystal structure where we denote the interlayer separation as the distance between the metal atoms. Figure 5.2 shows the primitive Brillouin zones in the layers, pictured as blue and green hexagons, and their relation to the supercell

Brillouin zone pictured in black. Note, that the twist angle θ separates the K point in the primitive Brillouin zones which is the same separation between the K and K' point in the supercell Brillouin zone. Figures 5.3-5.5 show the crystal structures for the various angles under study when viewed from the *c* and *a* axes.

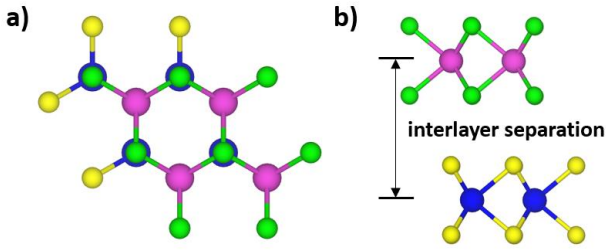

Figure 5.1. Bilayer $MoSe_2$-WSe_2 crystal structure. a) view from c-axis b) view from a-axis

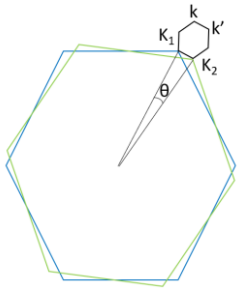

Figure 5.2. Primitive Brillouin zones in the layers and their relation to the supercell Brillouin zone.

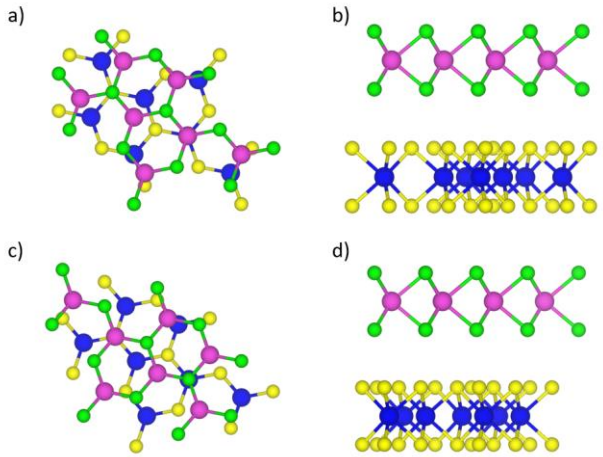

Figure 5.3. $\sqrt{7}x\sqrt{7}$ crystal structures. a) view from c-axis for $\theta = 21.787°$ b) view from a-axis for $\theta = 21.787°$ c) view from c-axis for $\theta = 38.213°$ d) view from a-axis for $\theta = 38.213°$

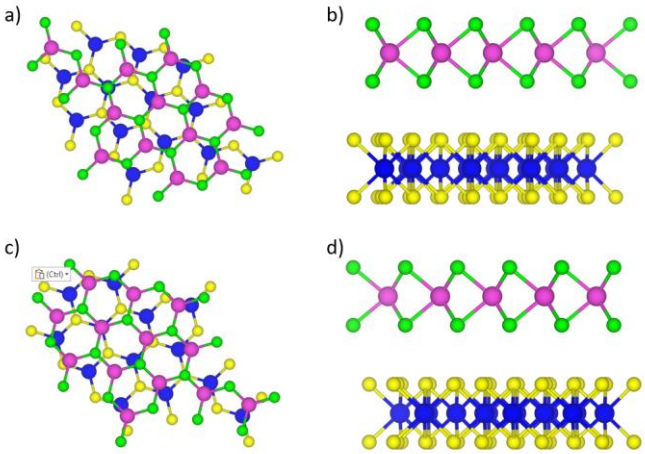

Figure 5.4. $\sqrt{13}x\sqrt{13}$ crystal structures. a) view from c-axis for $\theta = 27.796°$ b) view from a-axis for $\theta = 27.796°$ c) view from c-axis for $\theta = 32.204°$ d) view from a-axis for $\theta = 32.204°$

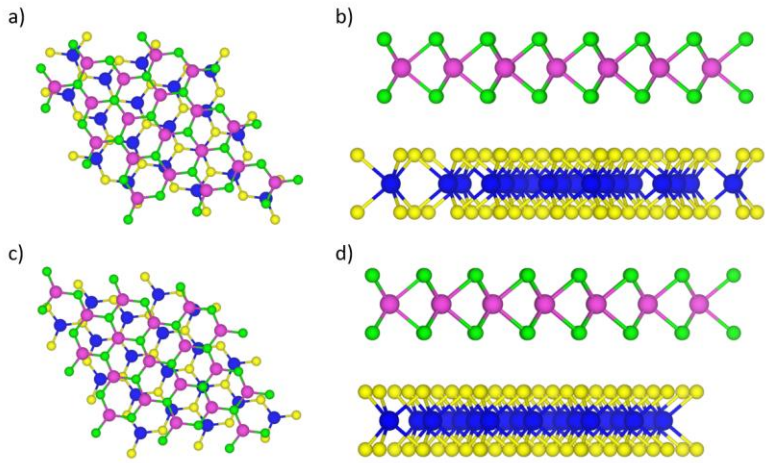

Figure 5.5. $\sqrt{19}x\sqrt{19}$ crystal structures. a) view from c-axis for $\theta = 13.174°$ b) view from a-axis for $\theta = 13.174°$ c) view from c-axis for $\theta = 46.826°$ d) view from a-axis for $\theta = 46.826°$

From here on out I am going to denote the primitive lattice vectors for the 1 x 1 hexagonal Brillouin zone as $\mathbf{A}_1$ and $\mathbf{A}_2$ and their corresponding reciprocal lattice vectors as $\mathbf{B}_1$ and $\mathbf{B}_2$. Table 5.1 contains the relationship between the primitive reciprocal lattice vectors and the supercell reciprocal lattice vectors along with their symmetry points in order to generate the correct band structure in the 1 x 1 Brillouin zone. This information along with the band unfolding describe in chapter 2 section 2.4.4.

Table 5.1. Reciprocal lattice vector relationship between the primitive Brillouin zone and the supercell Brillouin zone along with the standard symmetry points, K, M, and K', in the primitive Brillouin zone.

Cell Type	Angle (°)	Layer	Direction		Symmetry Points		
			A	B	K (1/3, 1/3)	M (0, 1/2)	K' (-1/3, 2/3)
$\sqrt{7}\ x\ \sqrt{7}$	21.787	top	b_1= 3 B_1 - B_2	b_2= B_1 + 2 B_2	(4/3, 1/3)	(1/2, 1)	(-1/3, 5/3)
		bottom	b_1= 3 B_1 - 2 B_2	b_2= 2 B_1 + B_2	(5/3, -1/3)	(1, 1/2)	(1/3, 4/3)
	38.213	top	b_1= 3 B_1 - 2 B_2	b_2= 2 B_1 + B_2	(5/3, -1/3)	(1, 1/2)	(1/3, 4/3)
		bottom	b_1= 2 B_1 - 3 B_2	b_2= 3 B_1 - B_2	(5/3, -4/3)	(3/2, -1/2)	(4/3, 1/3)
$\sqrt{13}\ x\ \sqrt{13}$	27.796	top	b_1= 4 B_1 - 3 B_2	b_2= 3 B_1 + B_2	(7/3, -2/3)	(3/2, 1/2)	(2/3, 5/3)
		bottom	b_1= 3 B_1 - 4 B_2	b_2= 4 B_1 - B_2	(7/3, -5/3)	(2, -1/2)	(5/3, 2/3)

	32.204	top	b_1= 4 B_1 - B_2	b_2= B_1 + 3 B_2	(5/3, 2/3)	(1/2, 3/2)	(-2/3, 7/3)
		bottom	b_1= 4 B_1 - 3 B_2	b_2= 3 B_1 + B_2	(7/3, -2/3)	(3/2, 1/2)	(2/3, 5/3)
$\sqrt{19}\,x\,\sqrt{19}$	13.174	top	b_1= 5 B_1 - 2 B_2	b_2= 2 B_1 + 3 B_2	(7/3, 1/3)	(1, 3/2)	(-1/3, 8/3)
		bottom	b_1= 5 B_1 - 3 B_2	b_2= 3 B_1 + 2 B_2	(8/3, -1/3)	(3/2, 1)	(1/3, 7/3)
	46.826	top	b_1= 5 B_1 - 3 B_2	b_2= 3 B_1 + 2 B_2	(8/3, -1/3)	(3/2, 1)	(1/3, 7/3)
		bottom	b_1= 3 B_1 - 5 B_2	b_2= 5 B_1 - 2 B_2	(8/3, -7/3)	(5/2, -1)	(7/3, 1/3)

To find the equilibrium interlayer separation, we perform self-consistent DFT calculations and plot the total energy as a function of interlayer separation which is shown in Figures 5.6 – 5.8. The minimum of this function is the ideal interlayer separation. We also constrict the atoms from relaxing in this step.

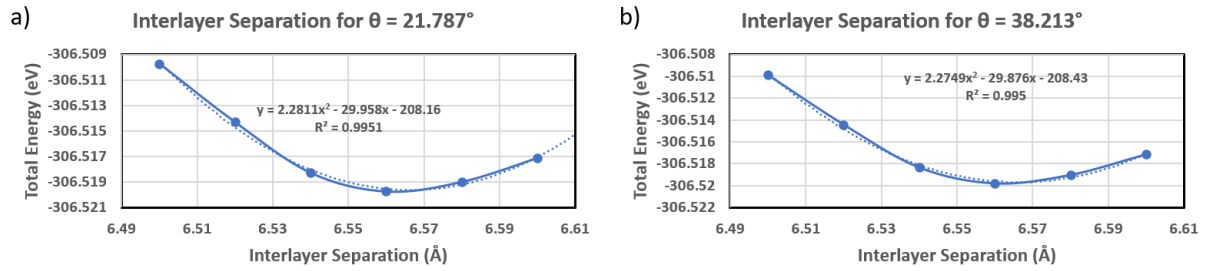

Figure 5.6. Interlayer separation determination for $\sqrt{7}x\sqrt{7}$ supercells. a) interlayer separation for $\theta = 21.787°$ b) interlayer separation for $\theta = 38.213°$

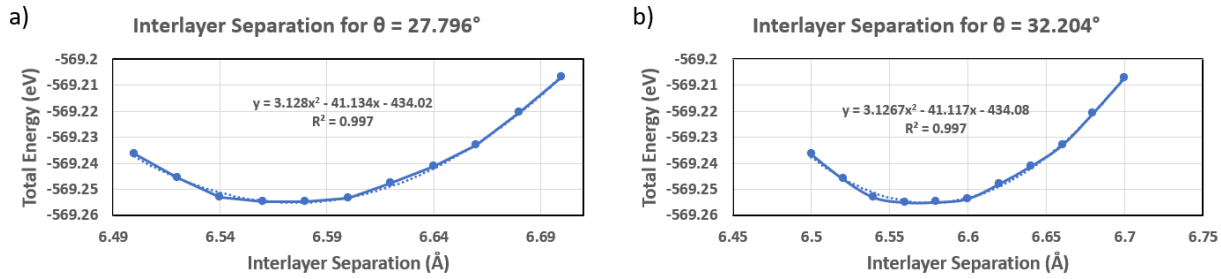

Figure 5.7. Interlayer separation determination for $\sqrt{13}x\sqrt{13}$ supercells. a) interlayer separation for $\theta = 27.796°$ b) interlayer separation for $\theta = 32.204°$

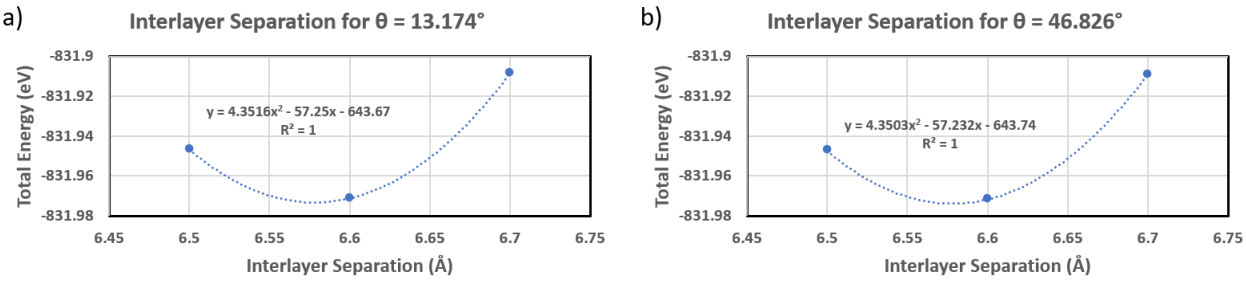

Figure 5.8. Interlayer separation determination for $\sqrt{19}x\sqrt{19}$ supercells. a) interlayer separation for $\theta = 13.174°$ b) interlayer separation for $\theta = 46.826°$

5.2 Electronic Band Structure

This electronic band structures for twisted bilayer $MoSe_2$-WSe_2 are plotted for the following angles: 13.174°, 21.787°, 27.796°, 32.204°, 38.213°, and 46.826°. These band structures are plotted in the supercell Brillouin zone as well as the 1 x 1 Brillouin zone to help better compare the band structures. We also include spin-orbit coupling to see its effects at the K and K' points.

5.2.1 Density Functional Theory

Density functional theory calculations were once again performed using VASP. The pseudopotentials made from projected augmented wave with the generalized gradient approximation using the Perdew-Burke-Ernzerhof exchange correlation functionals were used. The supercells also included approximately 20 Å of vacuum in the *c* direction between the bilayers in order to isolate these twisted bilayer TMD systems. The Monkhorst-Pack k point grid sampling that was used was 9 x 9 x 1 because denser k meshes did not alter any of the results. Some initial results on the relaxation of the twisted bilayer $MoSe_2$-WSe_2 structures did not alter the energy bands significantly so in this dissertation relaxation was not considered. Later in section 5.7, we instead investigate the role of the interlayer spacing and orbital interaction between the layers.

Figures 5.9 and 5.10 plot the electronic band structure for twisted $MoSe_2$-WSe_2 in the supercell Brillouin zone. Figure 5.9 a) has all the bands that have been folded back in whereas in Figure 5.9 b) the bands are unfolded in the 1 x 1 Brillouin zone. Since the size of the circle corresponds to the weight of the band in the 1 x 1 BZ, we see that the majority of the weight corresponds to the bands of $MoSe_2$ and WSe_2 layers in the supercell BZ. Figure 5.10 shows the angular dependence of the bands along the k path in the supercell BZ. Here we can see that the band structures in the same supercells but different angles produce similar energy bands when unfolded in the 1 x 1 BZ.

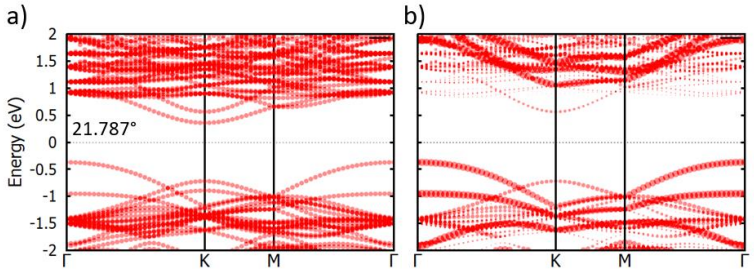

Figure 5.9. Energy band plots of twisted $MoSe_2$-WSe_2 bilayers, where $\theta = 21.787°$ ($\sqrt{7}x\sqrt{7}$ supercells) a) full band structure in the supercell Brillouin zone b) unfolded in the 1 x 1 Brillouin zone.

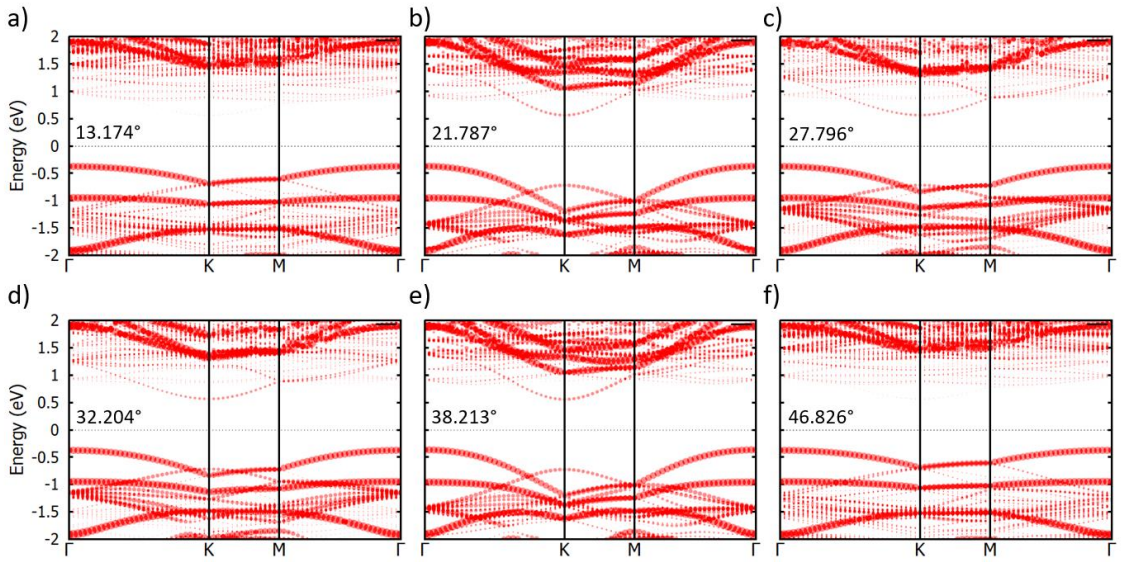

Figure 5.10. Energy band plots of the twisted $MoSe_2$-WSe_2 bilayers along the high symmetry points in the supercell Brillouin zone and unfolded in the 1 x 1 Brillouin zone. a) $\sqrt{19}x\sqrt{19}$ supercell where $\theta = 13.174°$ b) $\sqrt{7}x\sqrt{7}$ supercell where $\theta = 21.787°$ c) $\sqrt{13}x\sqrt{13}$ supercell where $\theta = 27.796°$ d) $\sqrt{13}x\sqrt{13}$ supercell where $\theta = 32.204°$ e) $\sqrt{7}x\sqrt{7}$ supercell where $\theta = 38.213°$ f) $\sqrt{19}x\sqrt{19}$ supercell where $\theta = 46.826°$

Figure 5.11 shows the comparison when the energy bands are plotted in the supercell BZ, a), and unfolded in either the bottom, b), or top layer, c), in red along with the untwisted bilayer $MoSe_2$-WSe_2 in black. We can see that there are 2 different levels of bands at the K point corresponding to states in either the bottom or top layer. Figure 5.12 a)-f) are energy band plots for twisted $MoSe_2$-WSe_2 viewed from the bottom layer and unfolded in the 1 x 1 Brillouin zone. We can see the splitting at K corresponds to different states in the different layers. Figure 5.12 helps to highlight the states in the bottom $MoSe_2$ layer. We also see that in figure 5.12 a) – f) that there are only slight differences in the energy band structure for these various twist angles. In table 5.2, we list the band gap as a function of twist angle and we see that there is only minute difference in the band gap values.

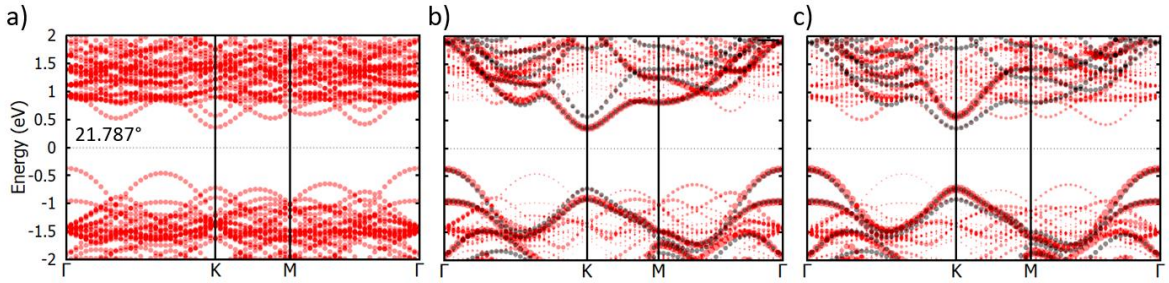

Figure 5.11. Energy band plots of twisted $MoSe_2$-WSe_2 bilayers, where $\theta = 21.787°$ ($\sqrt{7}x\sqrt{7}$ supercells). Black is standard bilayer and red is twisted bilayer. a) bands plotted in the supercell Brillouin zone (note: the scale along the k-path is not the same length as in b) and c)) b) unfolded in the 1 x 1 Brillouin zone and in the bottom layer c) unfolded in the 1 x 1 Brillouin zone and in the top layer

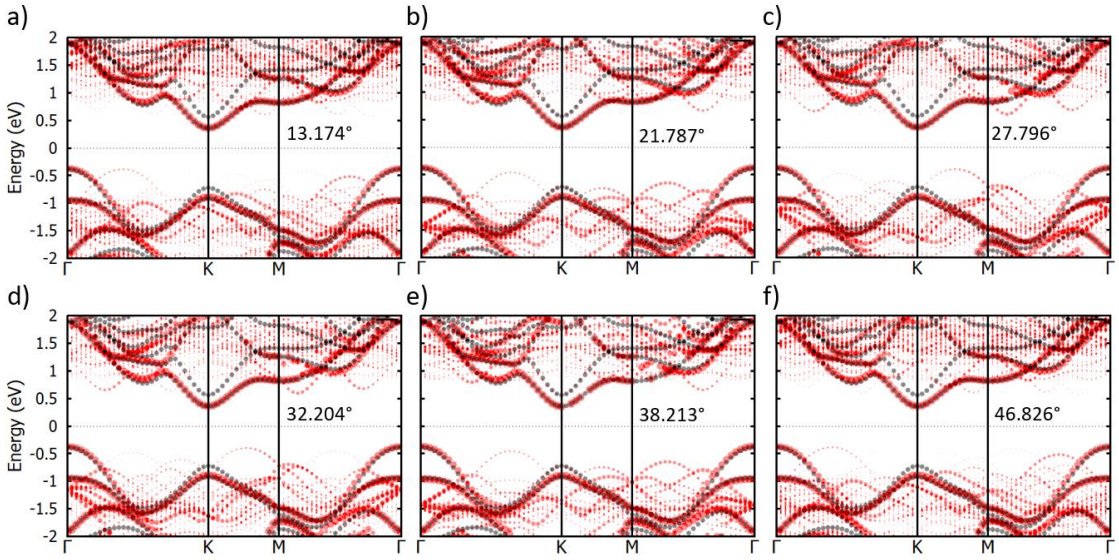

Figure 5.12. Energy band plots of the twisted $MoSe_2$-WSe_2 bilayers viewed from the bottom layer and unfolded in the 1 x 1 Brillouin zone. Black is standard bilayer and red is twisted bilayer. a) $\sqrt{19}x\sqrt{19}$ supercell where $\theta = 13.174°$ b) $\sqrt{7}x\sqrt{7}$ supercell where $\theta = 21.787°$ c) $\sqrt{13}x\sqrt{13}$ supercell where $\theta = 27.796°$ d) $\sqrt{13}x\sqrt{13}$ supercell where $\theta = 32.204°$ e) $\sqrt{7}x\sqrt{7}$ supercell where $\theta = 38.213°$ f) $\sqrt{19}x\sqrt{19}$ supercell where $\theta = 46.826°$

Table 5.2. Band gap information for twisted bilayer $MoSe_2$-WSe_2

Angle (°)	Supercell Size	Interlayer Separation (Å)	Band Gap (eV)
0	1 x 1	6.77	0.842
13.174	$\sqrt{19}\ x\ \sqrt{19}$	6.58	0.732
21.787	$\sqrt{7}\ x\ \sqrt{7}$	6.57	0.728

27.796	$\sqrt{13}\ x\ \sqrt{13}$	6.58	0.732
32.204	$\sqrt{13}\ x\ \sqrt{13}$	6.58	0.732
38.213	$\sqrt{7}\ x\ \sqrt{7}$	6.56	0.718
46.826	$\sqrt{19}\ x\ \sqrt{19}$	6.58	0.732

Including Spin Orbit Coupling

If we include spin-orbit coupling, we see similar results as we have seen in the simple monolayer and bilayer systems. That is, these systems without inversion symmetry and including spin-orbit coupling, we see a larger spin splitting due to the heavier tungsten atom in the top layer. Figure 5.13 plots the energy bands including spin-orbit coupling where θ = 21.787°. We see similar splitting at K and K' at the valence band edge we have seen in the bilayer TMD films.

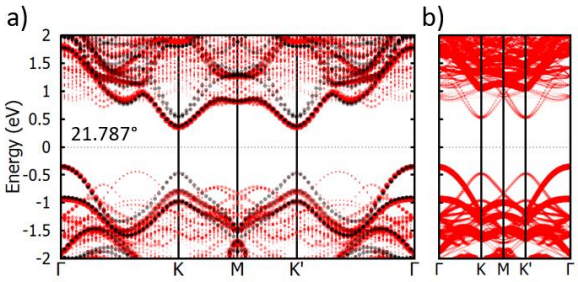

Figure 5.13. Energy band plots of the twisted $MoSe_2$-WSe_2 bilayers including spin-orbit coupling where $\theta = 21.787°$ ($\sqrt{7}\ x\ \sqrt{7}$ supercell). Black is standard bilayer and red is twisted bilayer. a) viewed from the bottom layer and unfolded in the 1 x 1 Brillouin zone b) plotted in the supercell Brillouin zone

5.3 Density of States

The density of states for twisted bilayer $MoSe_2$-WSe_2 are plotted in Figures 5.14 – 5.16. For the θ = 21.787° ($\sqrt{7}\ x\ \sqrt{7}$ supercells), θ = 27.796° ($\sqrt{13}\ x\ \sqrt{13}$ supercells), and θ = 46.826° ($\sqrt{19}\ x\ \sqrt{19}$ supercells) we see that the orbital character of the valence band is d_{z^2} for the

metal atoms and slight s but mostly p_z character for the chalcogens. At the conduction band edge, we see that the metal atoms are d_{z^2} still but the chalcogens are slightly more p_x as well as p_y in character. For the θ = 38.213° ($\sqrt{7}\ x\ \sqrt{7}$ supercells), θ = 32.204° ($\sqrt{13}\ x\ \sqrt{13}$ supercells), and θ = 13.174° ($\sqrt{19}\ x\ \sqrt{19}$ supercells) we see that the orbital character of the metal atoms is still d_{z^2} at both the conduction and valence band edges. For the chalcogens we see that orbital character at the conduction band is slightly more p_y than p_x in character opposite of what we see for θ = 21.787° ($\sqrt{7}\ x\ \sqrt{7}$ supercells), θ = 27.796° ($\sqrt{13}\ x\ \sqrt{13}$ supercells), and θ = 46.826° ($\sqrt{19}\ x\ \sqrt{19}$ supercells).

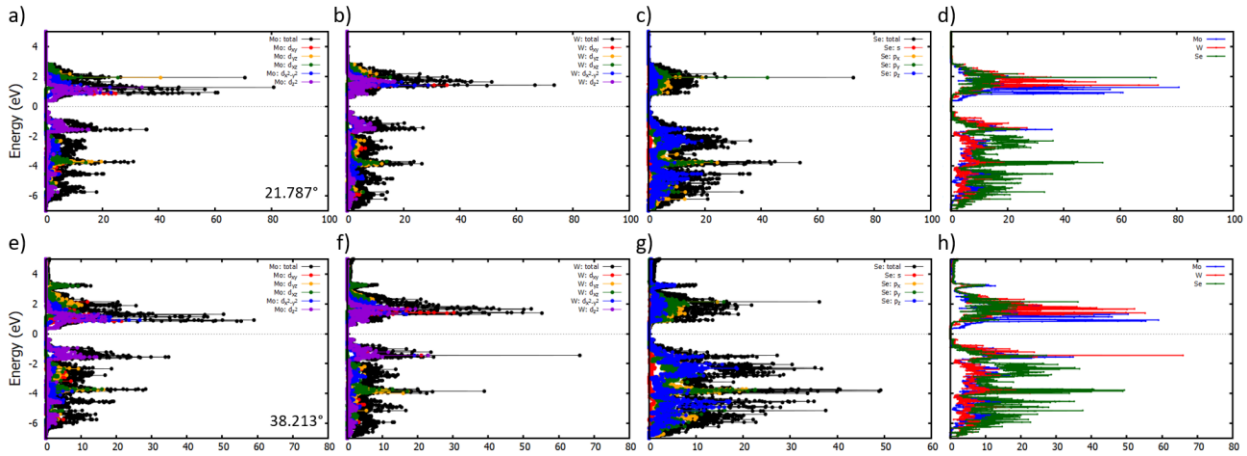

Figure 5.14. Density of states for twisted $MoSe_2$-WSe_2 bilayers $\sqrt{7}x\sqrt{7}$ supercells. a) Mo partial density of states $\theta = 21.787°$ b) W partial density of states $\theta = 21.787°$ c) Se partial density of states $\theta = 21.787°$ d) total density of states $\theta = 21.787°$ e) Mo partial density of states $\theta = 38.213°$ f) W partial density of states $\theta = 38.213°$ g) Se partial density of states $\theta = 38.213°$ h) total density of states $\theta = 38.213°$

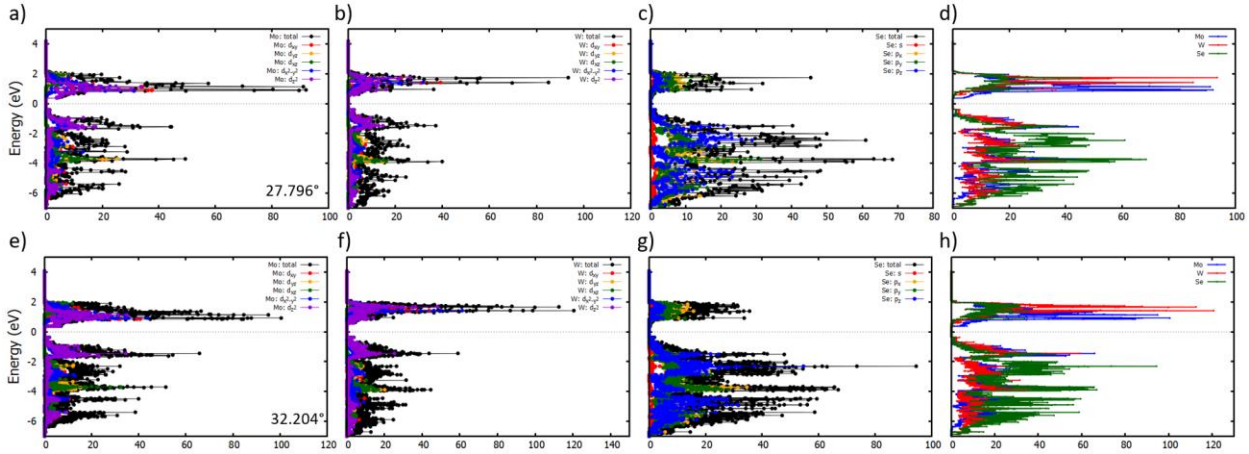

Figure 5.15. Density of states for twisted $MoSe_2$-WSe_2 bilayers $\sqrt{13}x\sqrt{13}$ supercells. a) Mo partial density of states $\theta = 27.796°$ b) W partial density of states $\theta = 27.796°$ c) Se partial density of states $\theta = 27.796°$ d) total density of states $\theta = 27.796°$ e) Mo partial density of states $\theta = 32.204°$ f) W partial density of states $\theta = 32.204°$ g) Se partial density of states $\theta = 32.204°$ h) total density of states $\theta = 32.204°$

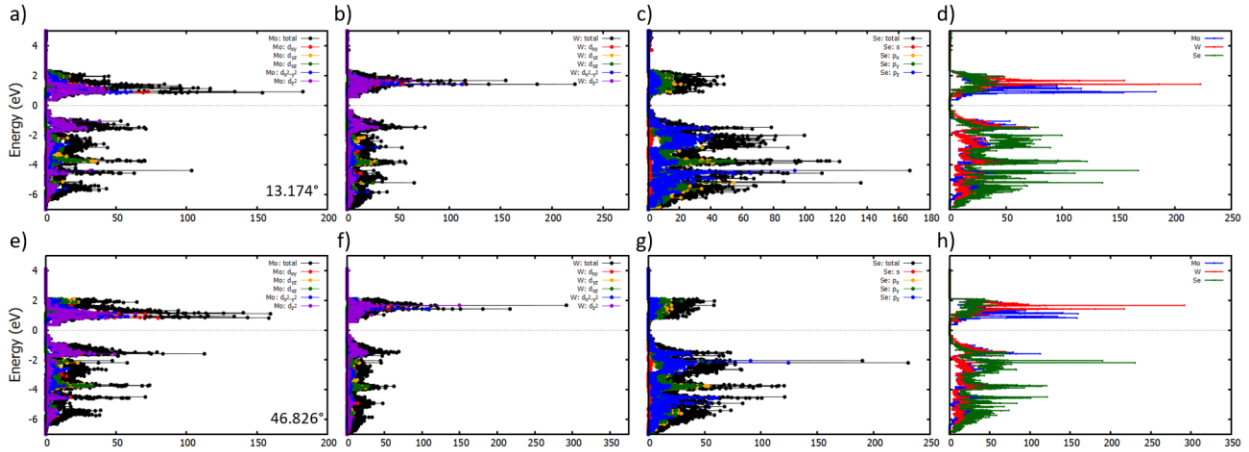

Figure 5.16. Density of states for twisted $MoSe_2$-WSe_2 bilayers $\sqrt{19}x\sqrt{19}$ supercells. a) Mo partial density of states $\theta = 13.174°$ b) W partial density of states $\theta = 13.174°$ c) Se partial density of states $\theta = 13.174°$ d) total density of states $\theta = 13.174°$ e) Mo partial density of states $\theta = 46.826°$ f) W partial density of states $\theta = 46.826°$ g) Se partial density of states $\theta = 46.826°$ h) total density of states $\theta = 46.826°$

5.4 Charge Distribution

The charge distribution for θ = 21.787° ($\sqrt{7}\ x\ \sqrt{7}$ supercells) is plotted along the c-axis in Figure 5.17 a) and along a-axis in Figure 5.17 b). These charge distributions correspond to the valence band edge in the energy range -1 eV ≤ E ≤ 0 eV. We can see the obvious d_{z^2} character for the metal atoms in the twisted bilayer $MoSe_2$-WSe_2 in Figure 5.17 a) and b). The character

of the chalcogen atoms are not as clear but, from the density of states plots in the previous section, 5.3, we know that they are mostly p_x and p_y in character.

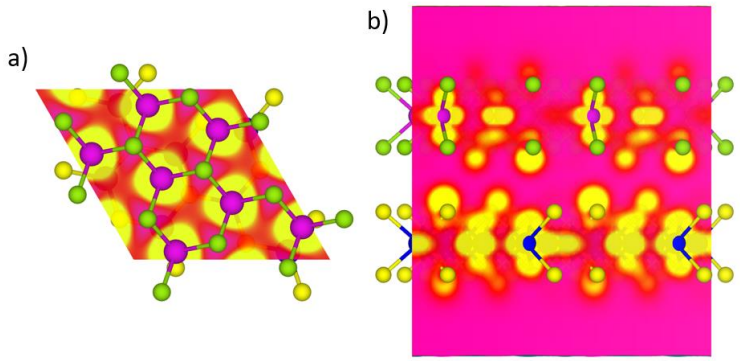

Figure 5.17. Charge distribution for twisted $MoSe_2$-WSe_2 bilayers $\sqrt{7}x\sqrt{7}$ supercells where $\theta = 21.787°$ in the energy range-1 eV ≤ E ≤ 0 eV. a) viewed from c-axis b) viewed from a-axis.

5.5 Optical Properties

The optical properties for twisted bilayer $MoSe_2$-WSe_2 share some of the same properties as regular bilayer $MoSe_2$-WSe_2. Optical studies typically focus on photoluminescence and Raman spectroscopy [8,11,12,23]. Photoluminescence of twisted bilayer TMDs can help reveal information about excitons and their processes in these materials. Raman spectroscopy can show how the twisting of the bilayers effects the vibrational modes in the materials.

5.5.1 Excitons

Twisted bilayer $MoSe_2$-WSe_2 has been shown to increase the lifetimes of excitons in these materials [8,9,12,23]. This has been attributed to the Moiré superlattice and potential that arises due to the twisting of the bilayers that creates pockets where the excitons can get trapped increasing their lifetime by isolating them. There are also interlayer excitons that can

be created between the conduction and valence bands of the layers which are more isolated and result in longer lifetimes.

Alexeev et al perform a study where they observe hybridized excitons in $MoSe_2$-WS_2 bilayers which manifested in angle-dependent shifts in the photoluminescence peak position [12]. This can be seen in Figure 5.18 adapted from [12] where we see a variation in the PL peak position as a function of twist angle. We can see that the peak position varies around the order of 50 meV. From this variation we would expect the band gap to also vary as a function of the twist angle but based on the DFT results it seems to not be the case meaning that there are more complex processes involved in twisted TMDs. Things like exciton diffusion or possible recombination can alter the PL peak position but not effect the band gap because the excitons depend on the transition between initial and final states which can be other than the states that span the gap.

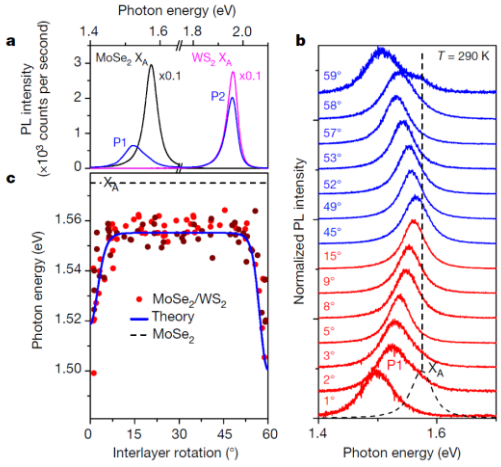

Figure 5.18. Photoluminescence response of twisted bilayer $MoSe_2$-WS_2 adapted from Alexeev et al. [12]. a) PL response in monolayer $MoSe_2$ (black), WS_2 (pink), and bilayer $MoSe_2$-WS_2 (blue) b) PL response of bilayer $MoSe_2$-WS_2 as a function of twist angle c) PL peak energy position as a function of twist angle

5.5.2 Optical Conductivity

The optical conductivity and the dielectric function are plotted in Figures 5.19 – 5.21. It seems that the twist angle has little impact on the dielectric function and the optical conductivity. This should be expected since there was little difference in the electronic band structure as a function of twist angle.

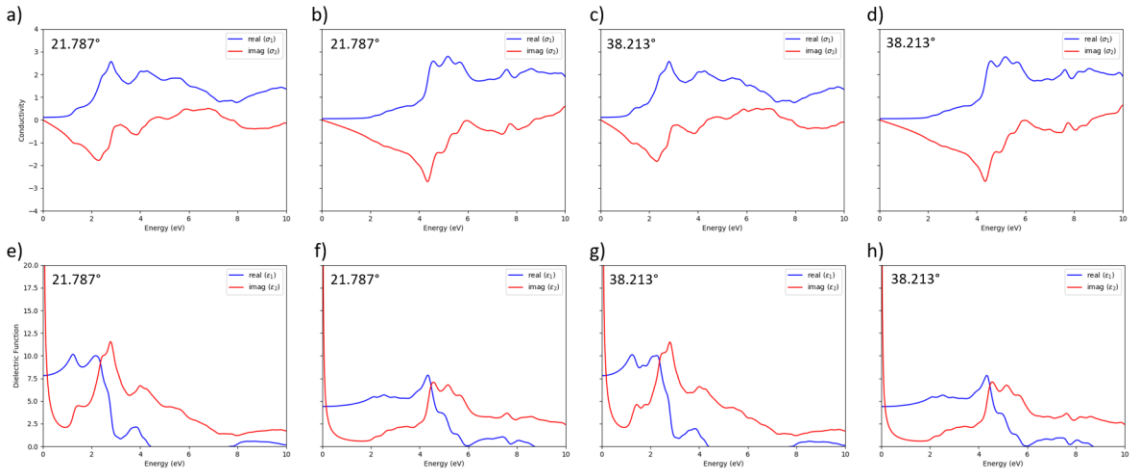

Figure 5.19. Dielectric function ϵ and conductivity σ for twisted bilayer $MoSe_2$-WSe_2 $\sqrt{7}$ x $\sqrt{7}$ supercells. a) ϵ_{xx} where $\theta = 21.787°$ b) ϵ_{zz} where $\theta = 21.787°$ c) ϵ_{xx} where $\theta = 38.213°$ d) ϵ_{zz} where $\theta = 38.213°$ e) σ_{xx} where $\theta = 21.787°$ f) σ_{zz} where $\theta = 21.787°$ g) σ_{xx} where $\theta = 38.213°$ h) σ_{zz} where $\theta = 38.213°$

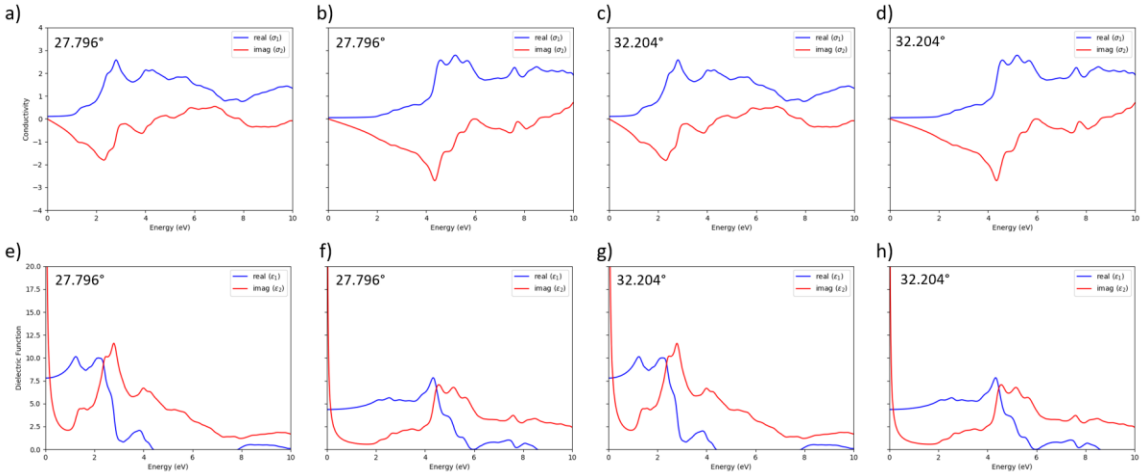

Figure 5.20. Dielectric function ϵ and conductivity σ for twisted bilayer $MoSe_2$-WSe_2 $\sqrt{13}$ x $\sqrt{13}$ supercells. a) ϵ_{xx} where $\theta = 27.796°$ b) ϵ_{zz} where $\theta = 27.796°$ c) ϵ_{xx} where $\theta = 32.204°$ d) ϵ_{zz} where $\theta = 32.204°$ e) σ_{xx} where $\theta = 27.796°$ f) σ_{zz} where $\theta = 27.796°$ g) σ_{xx} where $\theta = 32.204°$ h) σ_{zz} where $\theta = 32.204°$

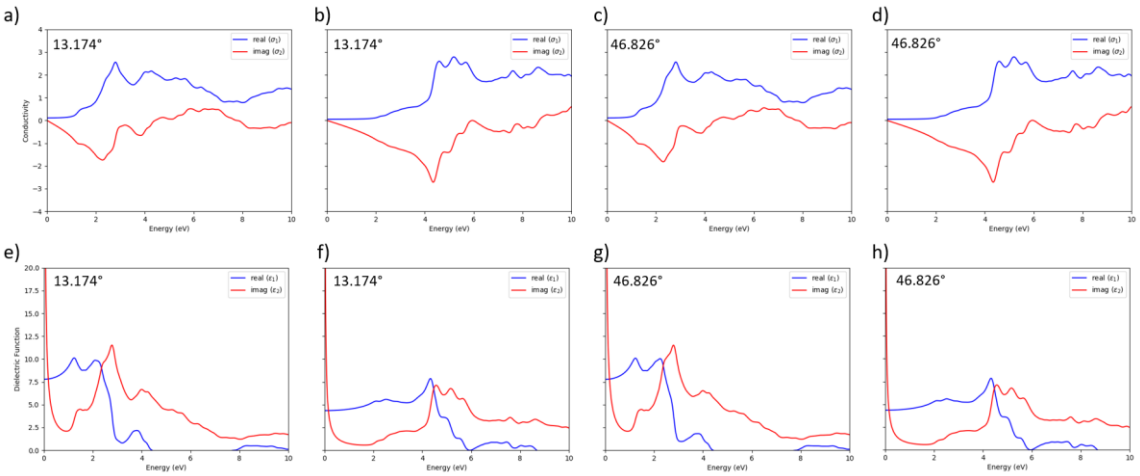

Figure 5.21. Dielectric function ϵ and conductivity σ for twisted bilayer $MoSe_2$-WSe_2 $\sqrt{19}$ x $\sqrt{19}$ supercells. a) ϵ_{xx} where $\theta = 13.174°$ b) ϵ_{zz} where $\theta = 13.174°$ c) ϵ_{xx} where $\theta = 46.826°$ d) ϵ_{zz} where $\theta = 46.826°$ e) σ_{xx} where $\theta = 13.174°$ f) σ_{zz} where $\theta = 13.174°$ g) σ_{xx} where $\theta = 46.826°$ h) σ_{zz} where $\theta = 46.826°$

5.6 Simulated Scanning Tunneling Microscopy Imagery

Simulated scanning tunneling microscopy images for twisted $MoSe_2$-WSe_2 are plotted in Figure 5.22 a) through f) in the energy range -1 eV ≤ E ≤ 0 eV. The black parallelogram corresponds to the unit cell for reference. This highlights the states at the valence band edge where we can easily see the Moiré pattern in the larger supercells in Figure 5.22 c) and f). We are able to see the 7 1 x 1 unit cells in Figure 5.22 a) and d), 13 1 x 1 unit cells in Figure 5.22 b) and e), and 19 1 x 1 unit cells in Figure 5.22 c) and f).

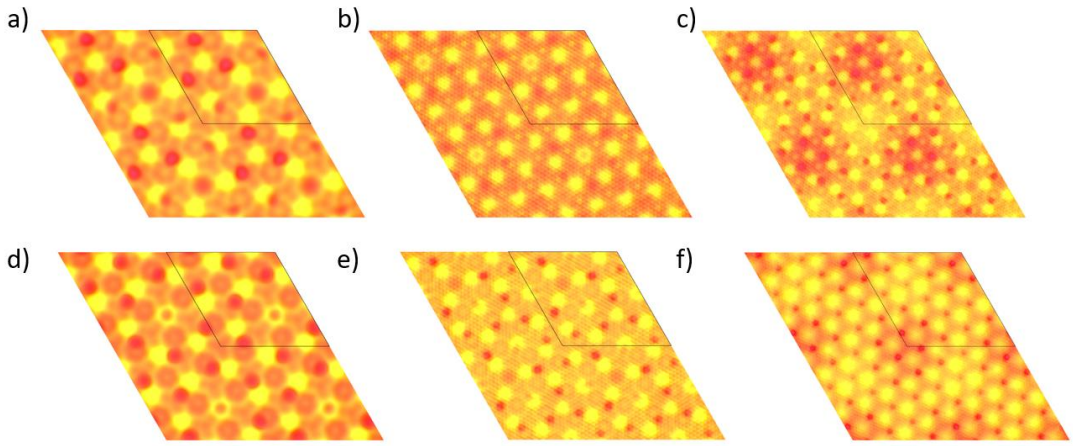

Figure 5.22. Simulated scanning tunneling microscopy images of twisted bilayer $MoSe_2$-WSe_2 in the energy range -0.5 eV ≤ E ≤ 0 eV. a) $\theta = 21.787°$ ($\sqrt{7}$ x $\sqrt{7}$ supercells) b) $\theta = 27.796°$ ($\sqrt{13}$ x $\sqrt{13}$ supercells) c) $\theta = 13.174°$ ($\sqrt{19}$ x $\sqrt{19}$ supercells) d) $\theta = 38.213°$ ($\sqrt{7}$ x $\sqrt{7}$ supercells) e) $\theta = 32.204°$ ($\sqrt{13}$ x $\sqrt{13}$ supercells) f) $\theta = 46.826°$ ($\sqrt{19}$ x $\sqrt{19}$ supercells)

5.7 Pressure Induced Flat Bands

There are also studies that observe the effect of pressure on the existence and variation of flat bands within the energy band structure [27-29]. These studies observe that flat bands can be observed for slightly larger twist angles under pressure in twisted bilayer graphene [27-29]. Carr et al., using density functional theory (DFT) and localized Wannier functions, observe flat band states in twisted bilayer graphene at angles larger than 1°, specifically θ=1.47° and θ=2.0°, with added pressure of 5% and 10% compression respectively. This suggests that there is an interplay in the formation of flat bands with the level of interlayer coupling.

We can relate the level of interaction by the decrease in the interlayer spacing from estimating the pressure of these compressed films. The pressure can be estimated by [27],

$$P = -\frac{1}{\Omega_s}\frac{dE_{tot}}{dh} \tag{5.1}$$

where Ω_s is the surface area of the supercell ($\overrightarrow{a_1} \times \overrightarrow{a_2}$). This gives us a metric to gauge how the orbitals between the layers interact.

5.7.1 Electronic Band Structure

The electronic band structure in twisted bilayer transition metal dichalcogenides, specifically bilayer $MoSe_2$-WSe_2, has many interesting features, especially when we force the bilayers to interact. This can be accomplished by applying pressure to the bands forcing the layers to come into closer proximity. We can see in figures 5.23 – 5.25 that as we decrease the interlayer separation, bands near the valence band maximum get pushed out of the valence band and into the gap of the twisted films. As we decrease the interlayer separation the bands begin to flatten out which can be seen in Figures 5.23 – 5.25. This is not seen by the normal non-twisted bilayer $MoSe_2$-WSe_2 films plotted in Figure 5.23 for both AB stacked and AA stacked. We can attribute the flattening and forcing of the bands out of the valence band into the gap to the twisting of the bilayers. Later in section 5.7.2 and 5.7.3 we can see the orbital composition of these flat band states to help highlight the nature of these flat bands.

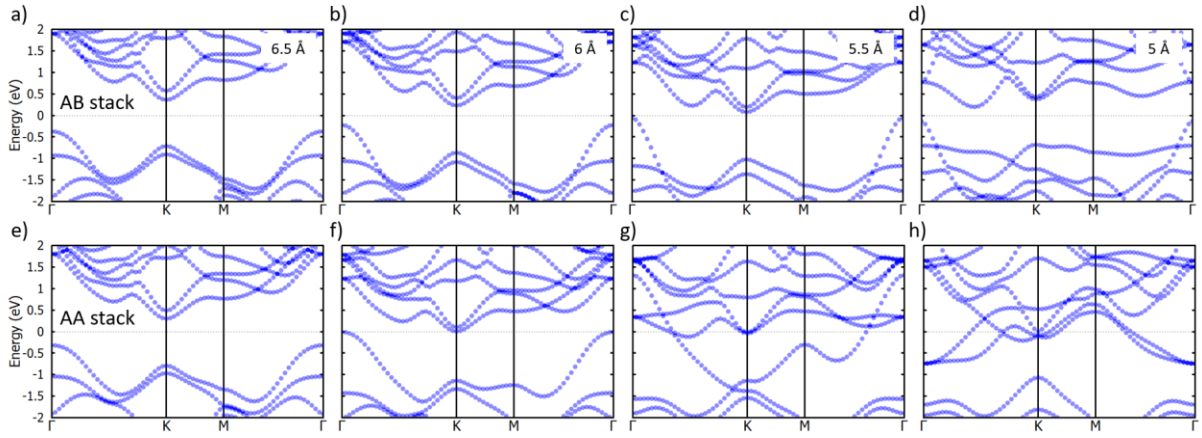

Figure 5.23. Bilayer $MoSe_2$-WSe_2 as a function of interlayer spacing. a) AB stacked bilayer $MoSe_2$-WSe_2 with an interlayer spacing of 6.5 Å b) AB stacked bilayer $MoSe_2$-WSe_2 with an interlayer spacing of 6 Å c) AB stacked bilayer $MoSe_2$-WSe_2 with an interlayer spacing of 5.5 Å d) AB stacked bilayer $MoSe_2$-WSe_2 with an interlayer spacing of 5 Å e) AA stacked bilayer $MoSe_2$-WSe_2 with an interlayer spacing of 6.5 Å f) AA stacked bilayer $MoSe_2$-WSe_2 with an interlayer spacing of 6 Å g) AA stacked bilayer $MoSe_2$-WSe_2 with an interlayer spacing of 5.5 Å h) AA stacked bilayer $MoSe_2$-WSe_2 with an interlayer spacing of 5 Å

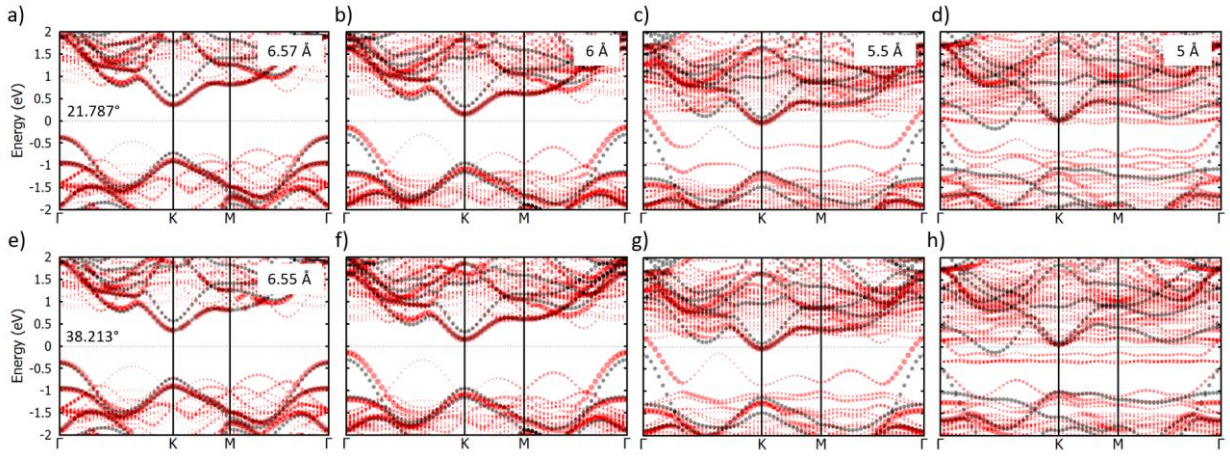

Figure 5.24. Electronic energy bands of twisted bilayer $MoSe_2$-WSe_2 as a function of interlayer spacing for $\sqrt{7}\ x\ \sqrt{7}$ supercells. Black is standard bilayer and red is twisted bilayer. a) – d) $\theta = 21.787°$ and e) – h) $\theta = 38.213°$

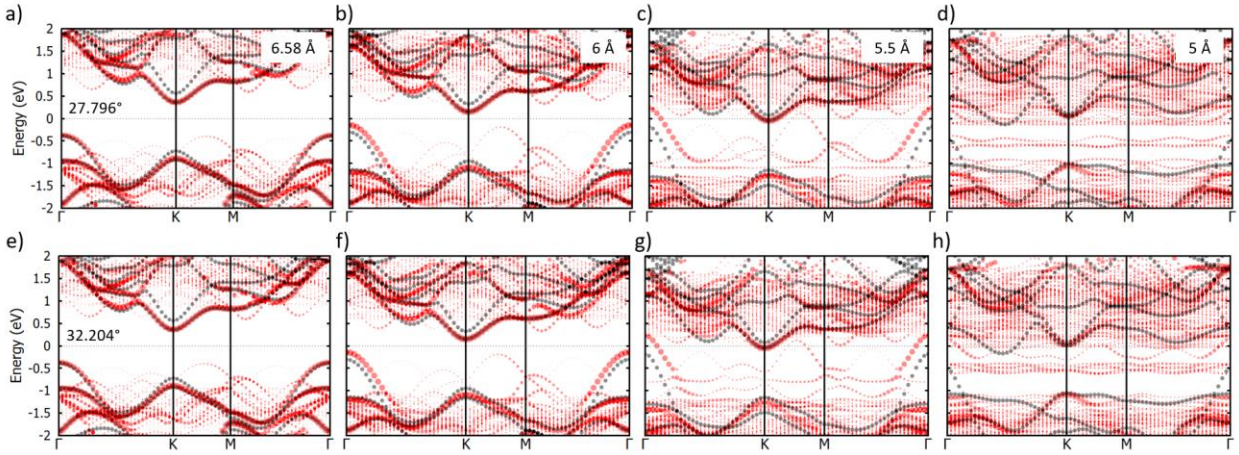

Figure 5.25. Electronic energy bands of twisted bilayer $MoSe_2$-WSe_2 as a function of interlayer spacing for $\sqrt{13}\ x\ \sqrt{13}$ supercells. Black is standard bilayer and red is twisted bilayer. a) – d) $\theta = 27.796°$ and e) – h) $\theta = 32.204°$

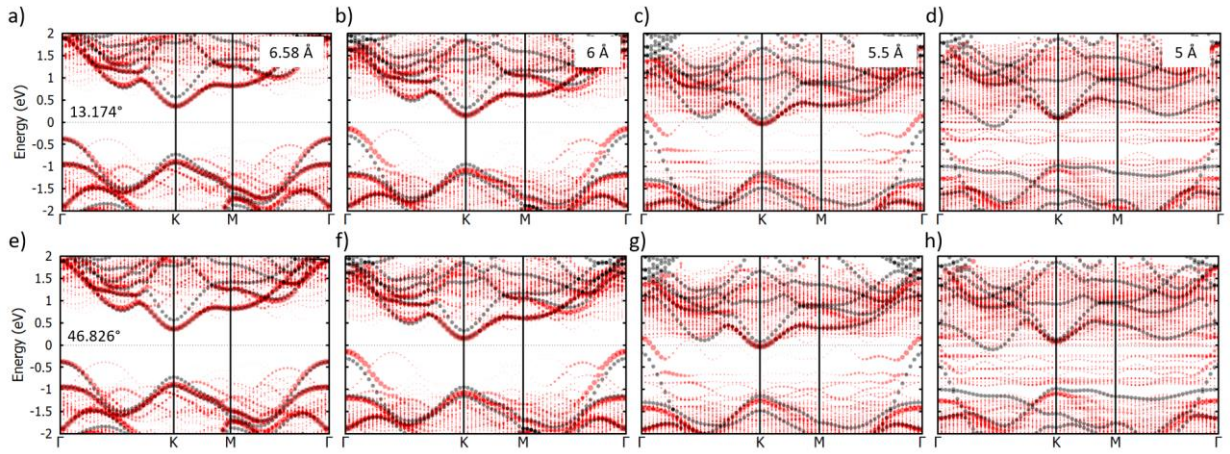

Figure 5.26. Electronic energy bands of twisted bilayer $MoSe_2$-WSe_2 as a function of interlayer spacing for $\sqrt{19}\ x\ \sqrt{19}$ supercells. Black is standard bilayer and red is twisted bilayer. a) – d) $\theta = 13.174°$ and e) – h) $\theta = 46.826°$

Including Spin-Orbit Coupling

The electronic band structures where spin-orbit coupling is included are plotted in Figures 5.27 – 5.28. We see that spin-orbit coupling splits the bands at the K and K' point as we have seen earlier. In Figure 5.27 for θ = 21.787° ($\sqrt{7}\ x\ \sqrt{7}$ supercells) with an interlayer separation of 5.4 Å we see that including spin-orbit coupling only slightly splits the flat band in the gap. In Figure 5.28 for θ = 46.826° ($\sqrt{19}\ x\ \sqrt{19}$ supercells) with an interlayer separation of 5.2 Å we see that including spin-orbit coupling it does not have much of an impact on the electronic band structure. The effect of spin-orbit coupling is minimal for these TMD films.

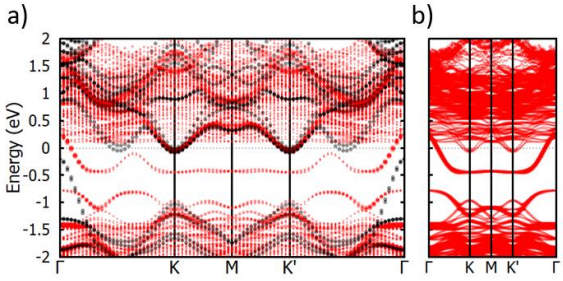

Figure 5.27. Electronic energy bands for twisted bilayer $MoSe_2$-WSe_2 including spin-orbit coupling where $\theta = 21.787°$ ($\sqrt{7}\ x\ \sqrt{7}$ supercells) and with an interlayer spacing of 5.4 Å. Black is standard bilayer and red is

twisted bilayer. a) unfolded in the 1 x 1 Brillouin zone b) plotting in the supercell Brillouin zone

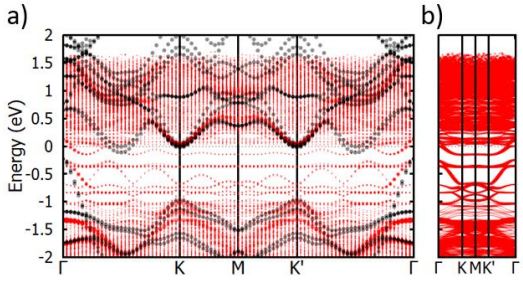

Figure 5.28. Electronic energy bands for twisted bilayer $MoSe_2$-WSe_2 including spin-orbit coupling where $\theta = 46.826°$ ($\sqrt{19}\ x\ \sqrt{19}$ supercells) and with an interlayer spacing of 5.2 Å. Black is standard bilayer and red is twisted bilayer. a) unfolded in the 1 x 1 Brillouin zone b) plotting in the supercell Brillouin zone

Spin Resolved Energy Bands

We can attempt to extract more information about the bands and their spin resolution by plotting the energy bands and their spin components. This is plotted in Figure 5.29 where we see the complex nature of the flat bands in the gap for θ = 21.787° ($\sqrt{7}\ x\ \sqrt{7}$ supercells) with an interlayer separation of 5.4 Å. It seems that the flat band split in the gap where the spin component pointing in the $-s_x$ direction is lower in energy along this k path. Whereas the spin component pointing in the $-s_y$ and $-s_z$ goes from lower in energy to higher in energy along this k path. We also notice that the valleys around the conduction band maximum at K and K' have different spin polarizations as we would expect from including spin-orbit coupling.

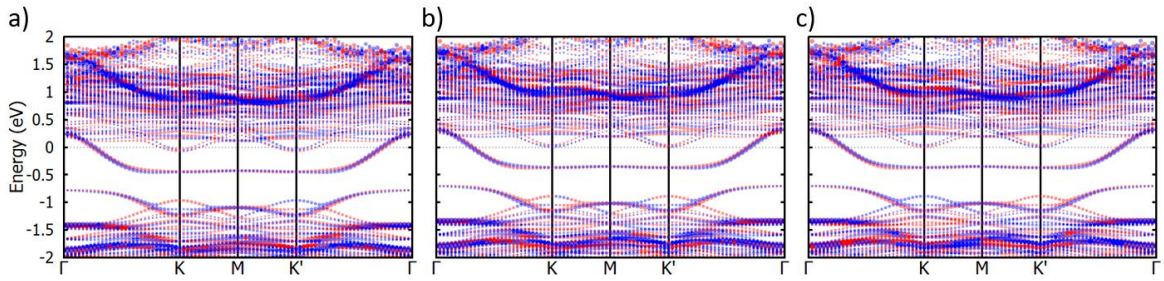

Figure 5.29. Spin texture of the electronic energy bands for twisted $MoSe_2$-WSe_2 bilayers with a twist angle of 21.787° ($\sqrt{7}$ x $\sqrt{7}$ supercells) and an interlayer separation of 5.4 Å. Red (blue) represents the spin pointing in the positive (negative) direction. Spin components are as follows: a) s_x b) s_y c) s_z

5.7.2 Density of States

The density of states of the twisted bilayer $MoSe_2$-WSe_2 gives useful information about the composition of the bands. We can see in Figure 5.30 where θ = 21.787° ($\sqrt{7}\ x\ \sqrt{7}$ supercells) with an interlayer separation of 5.4 Å that there exists a flat band in the gap and a subsequent spike in the density of states in Figure 5.30 c). This highlights the composition as well as the nature of a flat band. We also see that there is a larger spike in the density of states for selenium in both Figure 5.30 c) and Figure 5.31 c) highlighting the higher composition of selenium and its possible influence on creating these flat bands. We also see a similar effect in the twisted bilayer films where θ = 46.826° ($\sqrt{19}\ x\ \sqrt{19}$ supercells) with an interlayer separation of 5.2 Å except that there is a higher contribution from the metal atoms than the chalcogen atoms. We can also see that from the partial density of states plots in Figures 5.31 and 5.33 that there are multiple orbitals that contribute to these flat bands highlighting their complex nature.

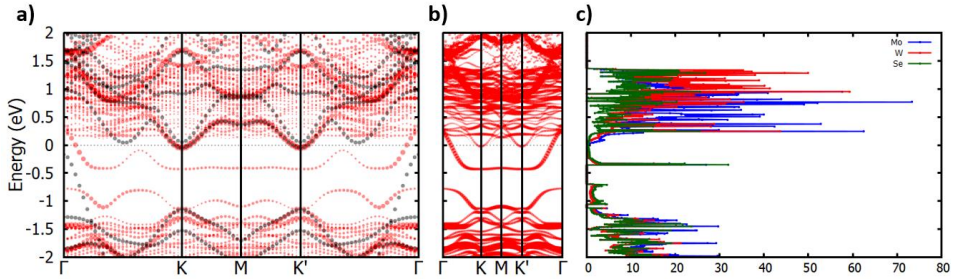

Figure 5.30. Energy bands and density of states for twisted bilayer $MoSe_2$-WSe_2 where $\theta = 21.787°$ ($\sqrt{7}$ x $\sqrt{7}$ supercells) and with an interlayer spacing of 5.4 Å. Black is standard bilayer and red is twisted bilayer. a) Energy band unfolded in the 1 x 1 Brillouin zone b) energy bands plotted in the supercell Brillouin zone c) Total partial density of states for each element

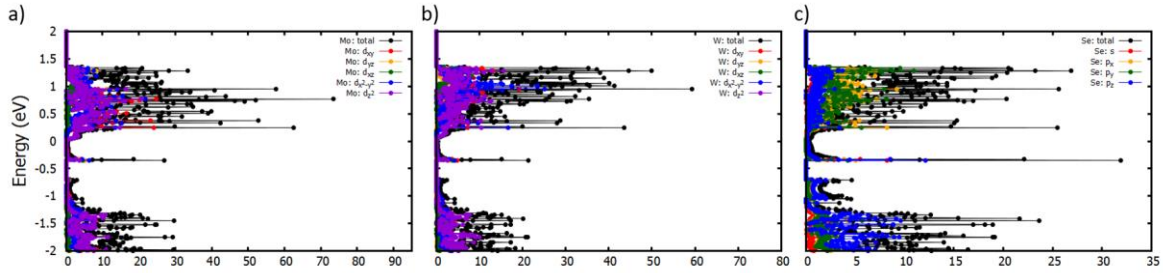

Figure 5.31. Partial density of states for twisted bilayer $MoSe_2$-WSe_2 where $\theta = 21.787°$ ($\sqrt{7}$ x $\sqrt{7}$ supercells) and with an interlayer spacing of 5.4 Å. a) Partial density of states for Mo orbitals b) Partial density of states for W orbitals c) Partial density of states for Se orbitals

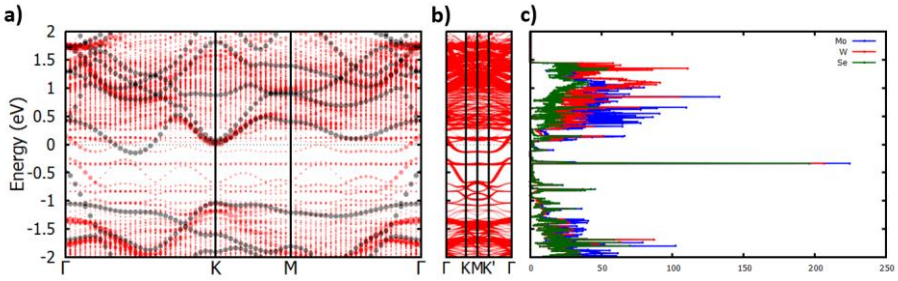

Figure 5.32. Energy bands and density of states for twisted bilayer $MoSe_2$-WSe_2 where $\theta = 46.826°$ ($\sqrt{19}$ x $\sqrt{19}$ supercells) and with an interlayer spacing of 5.2 Å. Black is standard bilayer and red is twisted bilayer. a) Energy band unfolded in the 1 x 1 Brillouin zone b) energy bands plotted in the supercell Brillouin zone c) Total partial density of states for each element

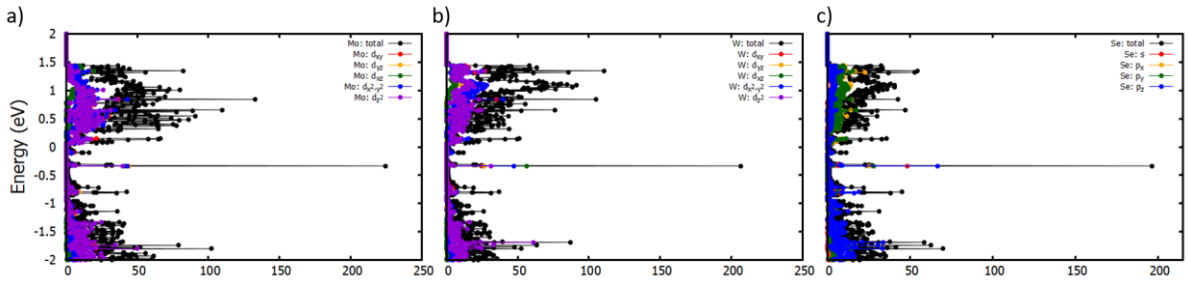

Figure 5.33. Partial density of states for twisted bilayer $MoSe_2$-WSe_2 where $\theta = 46.826°$ ($\sqrt{19}\ x\ \sqrt{19}$ supercells). a) Partial density of states for Mo orbitals b) Partial density of states for W orbitals c) Partial density of states for Se orbitals

5.7.3 Charge Distribution

The charge distribution for these twisted bilayer $MoSe_2$-WSe_2 films helps to highlight the key states and orbitals that contribute to features in the electronic energy band structure that are of interest. If we look at the charge density distribution in the energy range -0.5 eV ≤ E ≤ 0 eV where the flat band exists for θ = 21.787° ($\sqrt{7}\ x\ \sqrt{7}$ supercells) with an interlayer separation of 5.4 Å we see that there is a large contribution from the seleniums and metal atoms where the seleniums are in closest proximity, approximately 2.15 Å apart, which is pictured in Figure 5.34. The metal atoms surrounding the chalcogens in closest proximity bond with each other creating a triangular type state and the chalcogen atom create an antibonding state which can be seen in Figure 5.34 b). A similar scenario exists for θ = 46.826° ($\sqrt{19}\ x\ \sqrt{19}$ supercells) with an interlayer separation of 5.2 Å except we see that there are 3 times more seleniums in closest proximity, approximately 2.0 Å apart, pictured in Figure 5.35.

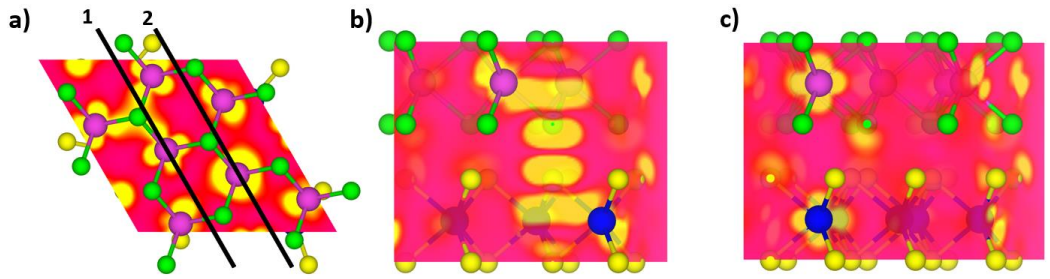

Figure 5.34. Charge density for twisted bilayer $MoSe_2$-WSe_2 where $\theta = 21.787°$ ($\sqrt{7}$ x $\sqrt{7}$ supercells) and with an interlayer spacing of 5.4 Å in the energy range -0.5 eV ≤ E ≤ 0 eV. a) slice of charge density viewed from c-axis b) slice of charge density viewed along slice 1 in a) c) slice of charge density viewed along slice 2 in a)

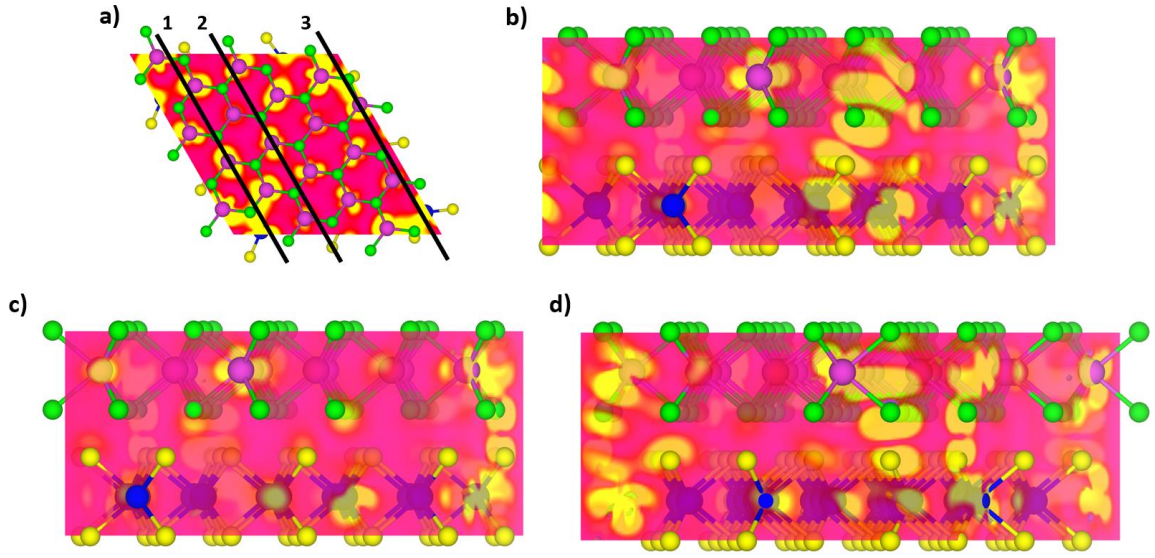

Figure 5.35. Charge density for twisted bilayer $MoSe_2$-WSe_2 where $\theta = 46.826°$ ($\sqrt{19}$ x $\sqrt{19}$ supercells) and with an interlayer spacing of 5.2 Å in the energy range -0.5 eV ≤ E ≤ -0.25 eV. a) slice of charge density viewed from c-axis b) slice of charge density viewed along slice 1 in a) c) slice of charge density viewed along slice 2 in a) d) slice of charge density viewed along slice 3 in a)

5.7.4 Optical Properties

The optical properties we are going to focus on are the dielectric function and the optical conductivity of the compressed twisted bilayers. The optical conductivity and dielectric function for twisted bilayer $MoSe_2$-WSe_2 where θ = 21.787° and an interlayer separation of 5.4 Å is plotted in Figure 5.36. We can see that peaks have been suppressed. This is mostly likely due to the fact that there are more available states that can transition from occupied states below the Fermi level to unoccupied states within the conduction band.

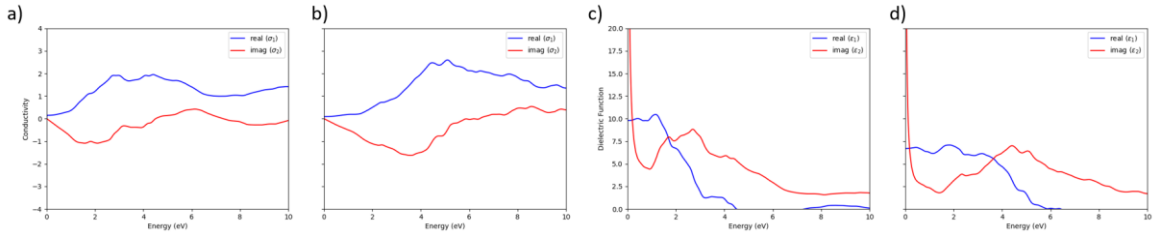

Figure 5.36. Dielectric function ϵ and conductivity σ for twisted bilayer $MoSe_2$-WSe_2 where $\theta = 21.787°$ ($\sqrt{7}\ x\ \sqrt{7}$ supercells) and with an interlayer spacing of 5.4 Å. a) σ_{xx} b) σ_{zz} c) ϵ_{xx} d) ϵ_{zz}

5.7.5 Simulated Scanning Tunneling Microscopy Imagery

The simulated scanning tunneling microscopy imagery for θ = 21.787° ($\sqrt{7}\ x\ \sqrt{7}$ supercells) with an interlayer separation of 5.4 Å and θ = 46.826° ($\sqrt{19}\ x\ \sqrt{19}$ supercells) with an interlayer separation of 5.2 Å are plotted in Figure 5.37 b)-d) and Figure 5.38 b)-d) respectively. We can see that as we decrease the interlayer spacing the states become more localized as we would expect from the flat bands that occur in the electronic band structure in Figures 5.30 and 5.32 and the charge distribution we see in Figures 5.34 and 5.35.

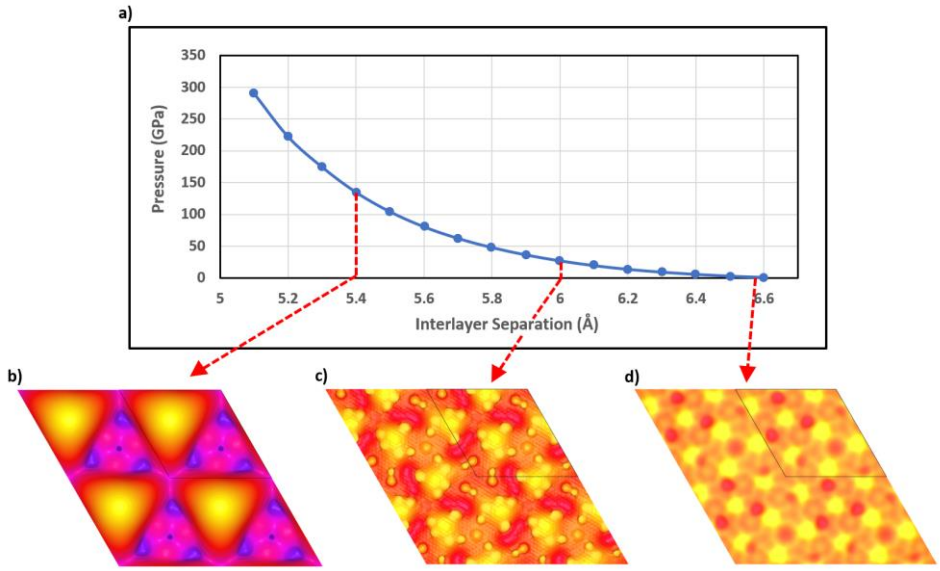

Figure 5.37. Pressure dependent scanning tunneling microscopy images for twisted bilayer $MoSe_2$-WSe_2 where $\theta = 21.787°$ ($\sqrt{7}\ x\ \sqrt{7}$ supercells). a) calculated pressure as a function of interlayer separation b)-d) STM imagery in the energy range -0.5 eV ≤ E ≤ 0 eV at approximately 4 Å from the surface.

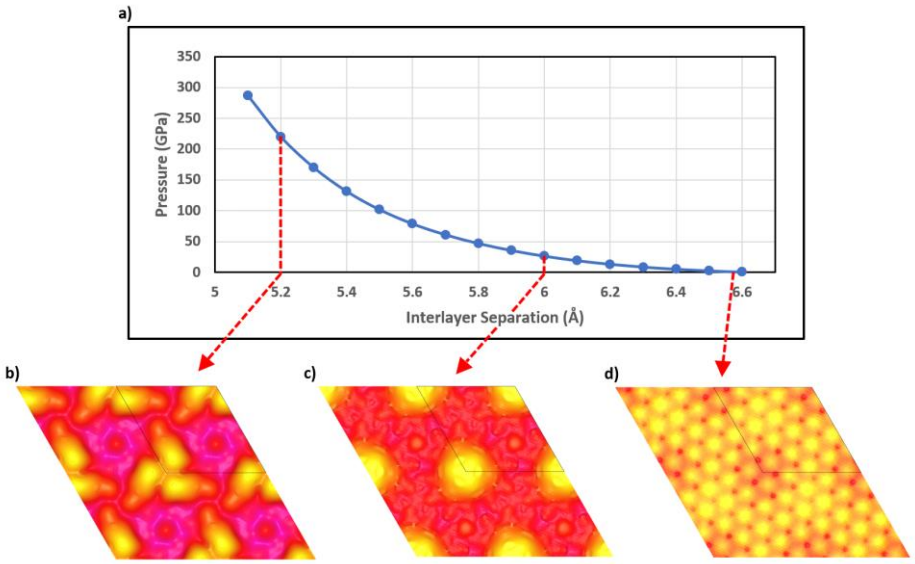

Figure 5.38. Pressure dependent scanning tunneling microscopy images for twisted bilayer $MoSe_2$-WSe_2 where $\theta = 46.826°$ ($\sqrt{19}$ x $\sqrt{19}$ supercells). a) calculated pressure as a function of interlayer separation b)-d) STM imagery in the energy range -0.5 eV ≤ E ≤ -0.25 eV at approximately 4 Å from the surface.

5.8 Defect States in Compressed Twisted Bilayer Transition Metal Dichalcogenides

Now we introduce an impurity like copper as we did in section 4.9 to probe the effects of both the copper replacement and the twisting of the bilayers. If we choose the correct interlayer separation and twist angle, we can have the pressure induced flat bands as well as the impurity bands overlap and see what sort of effects these have on each other and the overall material system. What we observe is that it is non-trivial to create a scenario where the flat bands from the impurities and the flat bands from the compressed twisted bilayers overlap because they exist too far apart in energy. Overall, what we observe is that these two effects in a sense destructively interfere with each other and reduce their individual effects to the material system.

5.8.1 Crystal Structure

The crystal structures are created the same as in section 5.1 except that one of the metal atoms is replaced by copper. Figure 5.39 show a sample crystal structure for the

$\sqrt{13}\ x\ \sqrt{13}$ supercells where θ = 27.796° and a Mo is replaced by a Cu, picture as orange within the crystal structure, in the $MoSe_2$ layer. Once again, supercell size plays a role in whether or not these impurities interact with each other so supercells of at least $\sqrt{13}\ x\ \sqrt{13}$ were used.

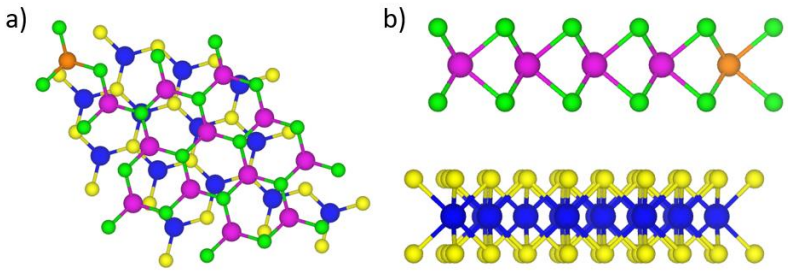

Figure 5.39. $\sqrt{13}x\sqrt{13}$ crystal structure with a copper impurity (orange in picture) in the $MoSe_2$ layer. a) view from c-axis for $\theta = 27.796°$ b) view from a-axis for $\theta = 27.796°$

5.8.2 Electronic Band Structure

The electronic band structure of copper doped twisted bilayer $MoSe_2$-WSe_2 has similar features to ones we see in section 4.9.2 where there are flat states around the Fermi energy due to the copper replacement. Figure 5.40 plots the electronic energy bands for twisted bilayer $MoSe_2$-WSe_2 as a function of decreasing interlayer separation. We can see that the effect of pushing the bands around the valence band maximum out of the bulk and into the gap still happens as we decrease the interlayer separation. Unfortunately matching the flat bands due to decreasing the interlayer separation did not occur for the list of commensurate angles studied mostly because the flat bands creating from decreasing interlayer separation and the flat states from the copper replacement never quite aligned. We can see that some of the bands that are pushed out of the valence band intersect the band around the Fermi level from the copper replacement.

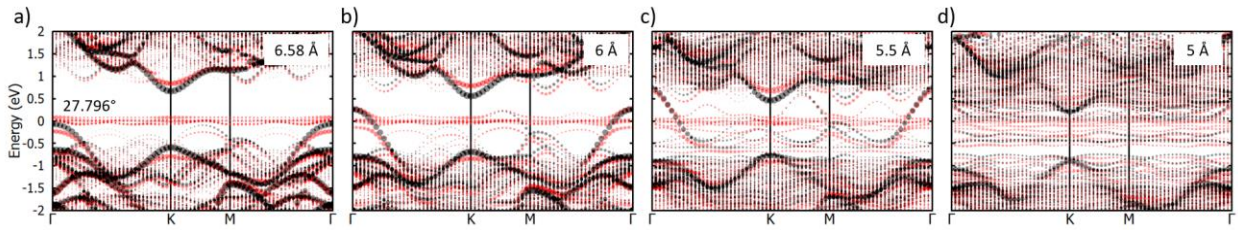

Figure 5.40. Energy band plots of copper doped twisted $MoSe_2$-WSe_2 for $\sqrt{13}x\sqrt{13}$ supercells where $\theta = 27.796°$ viewed from the bottom layer and unfolded in the 1 x 1 BZ as a function of interlayer spacing. Black is standard twisted bilayer and red is with the copper impurity. a) interlayer spacing of 6.58 Å b) interlayer spacing of 6 Å c) interlayer spacing of 5.5 Å d) interlayer spacing of 5 Å

Including Spin-Orbit Coupling

If we include spin-orbit coupling, we see similar trends in section 4.9.1 in Figure 5.41 where the flat states around the Fermi split. From the spin polarized calculation in VASP we see that the copper atom has added a magnetic moment to this material. For twisted bilayer $MoSe_2$-WSe_2 $\sqrt{13}\ x\ \sqrt{13}$ supercells where θ = 27.796° we see that the induced magnetic moment is on the order of 4.006 μ_B for an interlayer separation of 6.58 Å, 3.545 μ_B for an interlayer separation of 6 Å, and 2.422 μ_B for an interlayer separation of 5.5 Å. It would seem that decreasing the interlayer separation tends to decrease the strength of the overall magnetic moment of these materials. The effect of twist and adding the impurity seems to negate the effect of both of their overall effects, meaning suppression of the magnetic moments and the real space localization is dominated by the impurity state.

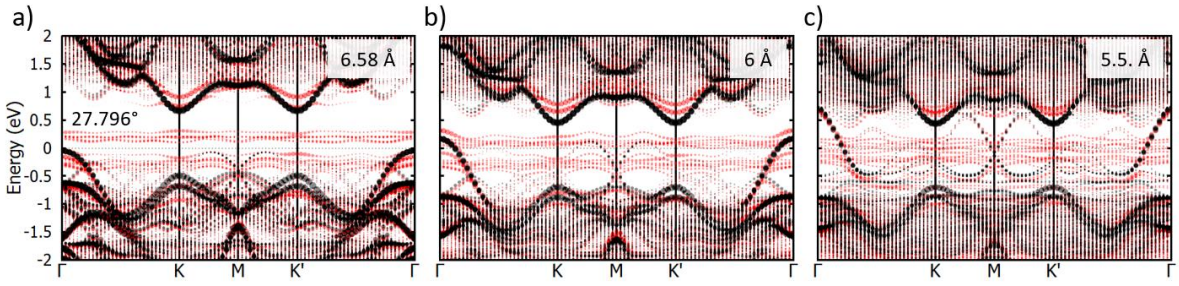

Figure 5.41. Energy bands (black) including spin-orbit coupling (red) of copper doped twisted $MoSe_2$-WSe_2 for $\sqrt{13}x\sqrt{13}$ supercells where $\theta = 27.796°$ viewed from the bottom layer and unfolded in the 1 x 1 BZ as a function of

interlayer spacing. a) interlayer spacing of 6.58 Å b) interlayer spacing of 6 Å c) interlayer spacing of 5.5 Å

5.8.3 Density of States

The density of states helps to highlight the contributions, not only in terms of atoms but also in terms orbitals, to the electronic band structure. We can see that the copper doped twisted bilayer TMDs at the equilibrium interlayer separation produce similar band structures and density of states as the non-twisted bilayers in sections 4.9.2 and 4.9.3. When we decrease the interlayer separation, we see that density of states in the flat bands from the copper replacement is suppressed compared to the equilibrium separation.

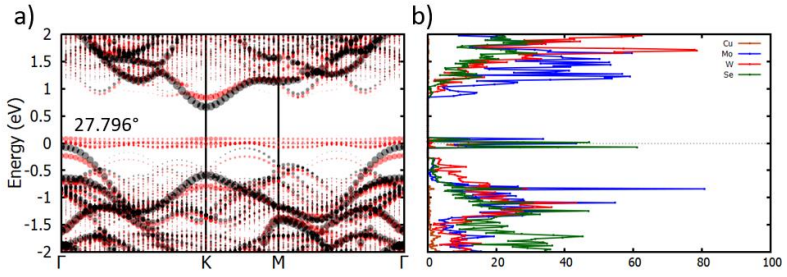

Figure 5.42. Electronic energy bands and density of states of twisted bilayer Cu:$MoSe_2$-WSe_2 for $\sqrt{13}x\sqrt{13}$ supercells where $\theta = 27.796°$ and an interlayer separation of 6.58 Å. a) energy bands viewed from the bottom layer and unfolded in the 1 x 1 BZ. Black is standard twisted bilayer and red is with the copper impurity. B) total density of states decomposed into the main atoms

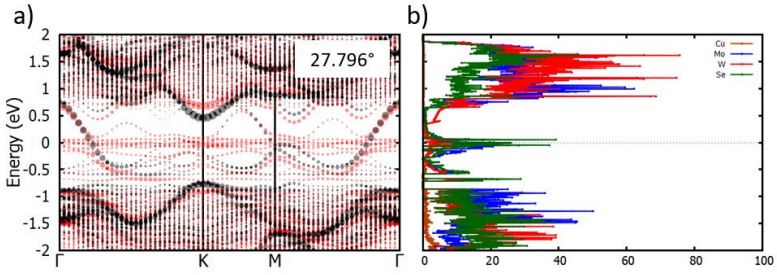

Figure 5.43. Electronic energy bands and density of states of twisted bilayer Cu:$MoSe_2$-WSe_2 for $\sqrt{13}x\sqrt{13}$ supercells where $\theta = 27.796°$ and an interlayer separation of 5.5 Å. a) energy bands viewed from the bottom layer and unfolded in the 1 x 1 BZ. Black is standard twisted bilayer and red is with the copper impurity. B) total density of states decomposed into the main atoms

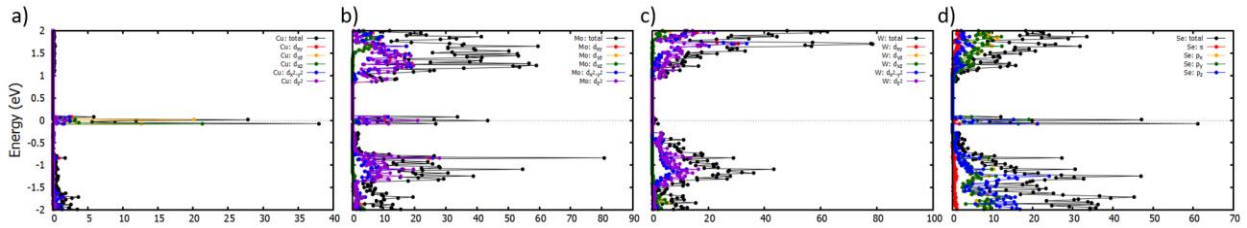

Figure 5.44. Density of states of twisted bilayer Cu:$MoSe_2$-WSe_2 for $\sqrt{13}x\sqrt{13}$ supercells where $\theta = 27.796°$ for an interlayer separation of 6.58 Å. a) Cu partial density of states b) Mo partial density of states c) W partial density of states d) Se partial density of states

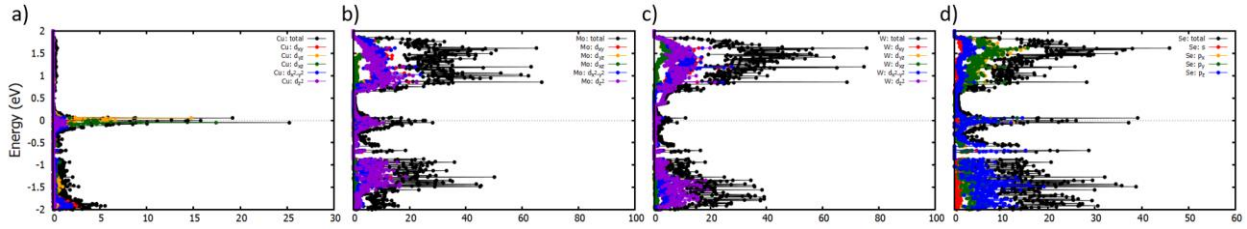

Figure 5.45. Density of states of twisted bilayer Cu:$MoSe_2$-WSe_2 for $\sqrt{13}x\sqrt{13}$ supercells where $\theta = 27.796°$ for an interlayer separation of 5.5 Å. a) Cu partial density of states b) Mo partial density of states c) W partial density of states d) Se partial density of states

5.8.4 Charge Distribution

The charge distribution helps to highlight the states and their interaction in the desired energy range. For copper doped twisted bilayer $MoSe_2$-WSe_2 $\sqrt{13}\ x\ \sqrt{13}$ supercells where θ = 27.796° we see that the charge distribution is similar to what we see in the untwisted case meaning that even though the charge distribution of the copper atom is extended, both in and out plane, it does not change anything in the other layer since they are loosely coupled. Note that the copper atom is highlighted with a black circle for reference. This is pictured in Figure 5.46 a) and b) and we also see in c) that as we decrease the interlayer separation the states in the layer containing the copper atom starts to effect the states in the opposite layer. This can be seen by the increase in the charge distribution of the selenium in the tungsten layer not containing the copper atom.

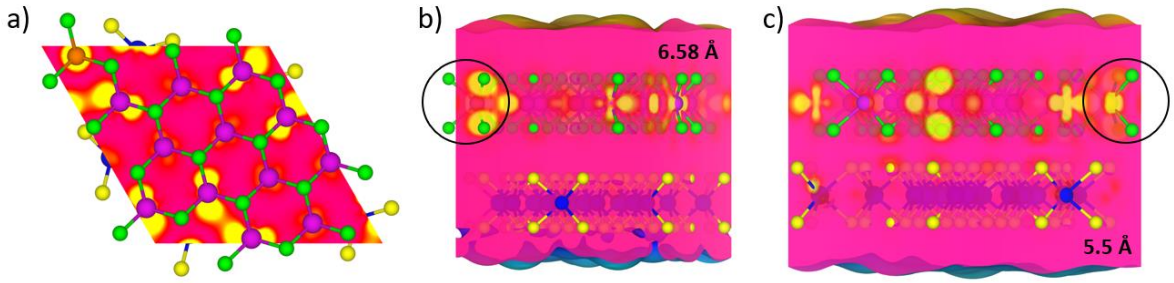

Figure 5.46. Charge density for twisted bilayer Cu:$MoSe_2$-WSe_2 where $\theta = 27.796°$ ($\sqrt{13}\ x\ \sqrt{13}$ supercells) in the energy range -0.25 eV ≤ E ≤ 0.25 eV. a) slice of charge density viewed from c-axis. b) slice of the charge density viewed along the a-axis with an interlayer separation of 6.58 Å. c) slice of the charge density viewed along the a-axis with an interlayer separation of 5.5 Å. Note: the black circle highlights the position of the copper atom.

5.8.5 Optical Properties

The optical properties for copper doped twisted bilayer $MoSe_2$-WSe_2 $\sqrt{13}\ x\ \sqrt{13}$ supercells where θ = 27.796° differ from the non-twisted case where we see a non-zero off-diagonal component. It seems that twisting the layers suppresses the off-diagonal component because the values we see are small that they might be due to noise. These are pictured in Figure 5.47 for reference. We also observe the small non-zero values for the yz and zx components but, given that they are small and can also be effected by the supercell selection size, they cannot be trusted.

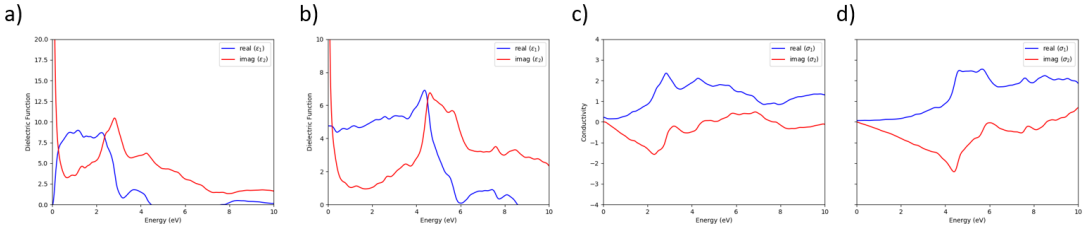

Figure 5.47. Dielectric function ϵ and conductivity σ for twisted bilayer Cu:$MoSe_2$-WSe_2 where $\theta = 27.796°$ ($\sqrt{13}\ x\ \sqrt{13}$ supercells) and with an interlayer spacing of 6.58 Å. a) ϵ_{xx} b) ϵ_{zz} c) σ_{xx} d) σ_{zz}

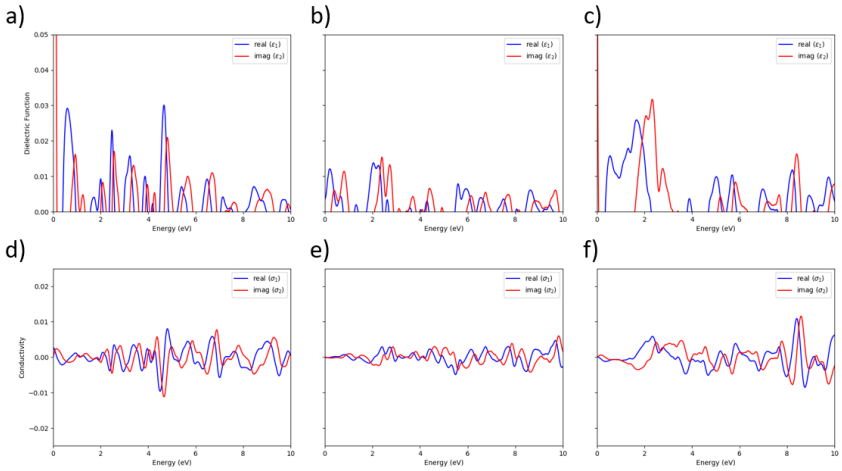

Figure 5.48. Dielectric function ϵ and conductivity σ for twisted bilayer Cu:$MoSe_2$-WSe_2 where $\theta = 27.796°$ ($\sqrt{13}$ x $\sqrt{13}$ supercells) and with an interlayer spacing of 6.58 Å. a) ϵ_{xy} b) ϵ_{yz} c) ϵ_{zx} d) σ_{xy} e) σ_{yz} f) σ_{zx}

5.8.6 Simulated Scanning Tunneling Microscopy Imagery

The simulated scanning tunneling microscopy images helps to highlight what an experimentalist might observe for the copper doped twisted bilayer $MoSe_2$-WSe_2 films. We can see in Figure 5.49 that the dominant features come from the hybridization between the copper atom and the other local atoms. It almost looks like 3 water molecules where the hydrogen lobes are pointed outward and are separated 120° apart from the center. The larger contribution comes from the bonding between the copper and the local chalcogen atoms but also extends outward to the next ring of metal atoms. The interaction between the copper and the chalcogens show up as pronounced yellow spheres. If we compare what we saw in the pressured induced simulated STM imagery in section 5.7, we can see that the localization from the twist angle is washed out by the stronger interaction from the copper dopant. We can also that the simulated STM imagery of the non-twisted TMS in section 4.9.6 are almost identical to the twisted bilayer $MoSe_2$-WSe_2 films.

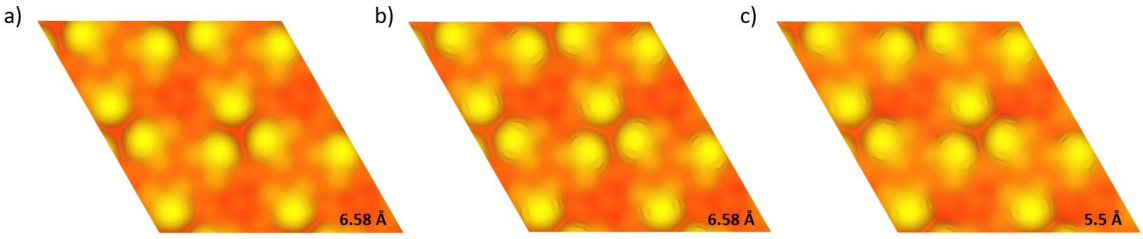

Figure 5.49. Simulated scanning tunneling microscopy images of twisted bilayer Cu:$MoSe_2$-WSe_2 for $\sqrt{13}\ x\ \sqrt{13}$ supercells where $\theta = 27.796°$ in the energy range -0.25 eV ≤ E ≤ 0.25 eV. a) interlayer spacing of 6.58 Å where copper is in the top Mo layer b) interlayer spacing of 6.58 Å where copper is in the top W layer c) interlayer spacing of 5.5 Å where copper is in the top Mo layer

References

1. Cao, Y., Fatemi, V., Fang, S., Watanabe, K., Taniguchi, T., Kaxiras, E., & Jarillo-Herrero, P. (2018). Unconventional superconductivity in magic-angle graphene superlattices. *Nature, 556*, 43-50. doi:10.1038/nature26160
2. Cao, Y., Fatemi, V., Demir, A., Fang, S., Tomarken, S. L., Luo, J. Y., . . . Jarillo-Herrero, P. (2018). Correlated insulator behaviour at half-filling in magic-angle graphene superlattices. *Nature, 556*, 80-84. doi:doi:10.1038/nature26154
3. Yankowitz, M., Chen, S., Polshyn, H., Zhang, Y., Watanabe, K., Taniguchi, T., . . . Dean, C. R. (2019). Tuning superconductivity in twisted bilayer graphene. *Science, 363*(6431), 1059-1064. doi:10.1126/science.aav1910
4. Xie, Y., Lian, B., Jäck, B., Liu, X., Chiu, C.-L., Watanabe, K., . . . Yazdani, A. (2019). Spectroscopic signatures of many-body correlations in magic-angle twisted bilayer graphene. *Nature, 572*, 101-105. doi:https://doi.org/10.1038/s41586-019-1422-x
5. Kerelsky, A., McGilly, L. J., Kennes, D. M., Xian, L., Yankowitz, M., Chen, S., . . . Pasupathy, A. N. (2019). Maximized electron interactions at the magic angle in twisted bilayer graphene. *Nature, 572*, 95-100. doi:https://doi.org/10.1038/s41586-019-1431-9
6. Zhang, Z., Wang, Y., Watanabe, K., Taniguchi, T., Ueno, K., Tutuc, E., & LeRoy, B. J. (2020). Flat bands in twisted bilayer transition metal dichalcogenides. *Nature Physics, 16*, 1093-1096. doi:https://doi.org/10.1038/s41567-020-0958-x
7. Shabani, S., Halbertal, D., Wu, W., Chen, M., Liu, S., Hone, J., . . . Pasupathy, A. N. (2021). Deep moiré potentials in twisted transition metal dichalcogenide bilayers. *Nature Physics, 17*, 720-725. doi:https://doi.org/10.1038/s41567-021-01174-7
8. Tran, K., Moody, G., Wu, F., Lu, X., Choi, J., Kim, K., . . . Li, X. (2019). Evidence for moiré excitons in van der Waals heterostructures. *Nature, 567*, 71-75. doi:https://doi.org/10.1038/s41586-019-0975-z
9. Choi, J., Hsu, W.-T., Lu, L.-S., Sun, L., Cheng, H.-Y., Lee, M.-H., . . . Chang, W.-H. (2020). Moiré potential impedes interlayer exciton diffusion in van der Waals heterostructures. *Science Advances, 6*, 1-6. doi:10.1126/sciadv.aba8866
10. Waters, D., Nie, Y., Lüpke, F., Pan, Y., Fölsch, S., Lin, Y.-C., . . . Feenstra, R. M. (2020). Flat Bands and Mechanical Deformation Effects in the Moiré Superlattice of MoS2-WSe2 Heterobilayers. *ACS Nano, 14*, 7564-7573. doi:https://dx.doi.org/10.1021/acsnano.0c03414
11. Zheng, S., Sun, L., Zhou, X., Liu, F., Liu, Z., Shen, Z., & Fan, H. J. (2015). Coupling and Interlayer Exciton in Twist-Stacked WS2 Bilayers. *Advanced Optical Materials, 3*, 1600-1605. doi:10.1002/adom.201500301
12. Alexeev, E. M., Ruiz-Tijerina, D. A., Danovich, M., Hamer, M. J., Terry, D. J., Nayak, P. K., . . . Tartakovskii, A. I. (2019). Resonantly hybridized excitons in moiré superlattices in van der Waals heterostructures. *Nature, 567*, 81-86. doi:https://doi.org/10.1038/s41586-019-0986-9
13. Scuri, G., Andersen, T. I., Zhou, Y., Wild, D. S., Sung, J., Gelly, R. J., . . . Park, H. (2020). Electrically Tunable Valley Dynamics in Twisted WSe2/WSe2 Bilayers. *Physical Review Letters, 124*, 1-8. doi:10.1103/PhysRevLett.124.217403

14. Yan, W., Meng, L., Meng, Z., Weng, Y., Kang, L., & Li, X.-a. (2019). Probing Angle-Dependent Interlayer Coupling in Twisted Bilayer WS2. *Journal of Physical Chemistry, 123*, 30684-30688. doi:10.1021/acs.jpcc.9b08602
15. Naik, M. H., & Jain, M. (2018). Ultraflatbands and Shear Solitons in Moiré Patterns of Twisted Bilayer Transition Metal Dichalcogenides. *Physical Review Letters, 121*, 1-6. doi:10.1103/PhysRevLett.121.266401
16. Naik, M. H., Kundu, S., Maity, I., & Jain, M. (2020). Origin and evolution of ultraflat bands in twisted bilayer transition metal dichalcogenides: Realization of triangular quantum dots. *Physical Review B, 102*(7), 075413. doi:https://doi.org/10.1103/PhysRevB.102.075413
17. Vitale, V., Atalar, K., Mostofi, A. A., & Lischner, J. (2021). Flat band properties of twisted transition metal dichalcogenide homo- and heterobilayers of MoS2, MoSe2, WS2 and WSe2. *2D Materials, 8*, 1-17. doi:https://doi.org/10.1088/2053-1583/ac15d9
18. Tan, Y., Chen, F. W., & Ghosh, A. W. (2016). First principles study and empirical parametrization of twisted bilayer MoS2 based on band-unfolding. *Applied Physics Letters, 109*, 1-4. doi:http://dx.doi.org/10.1063/1.4962438
19. Patra, S., Kumari, P., & Mahadevan, P. (2020). Evolution of the electronic structure of twisted bilayer MoSe2. *Physical Review B, 102*, 1-7. doi:10.1103/PhysRevB.102.205415
20. Liu, K., Zhang, L., Cao, T., Jin, C., Qiu, D., Zhou, Q., . . . Wang, F. (2014). Evolution of interlayer coupling in twisted molybdenum disulfide bilayers. *Nature Communications, 5*(4966). doi:https://doi.org/10.1038/ncomms5966
21. Zhang, C., Chuu, C.-P., Ren, X., Li, M.-Y., Li, L.-J., Jin, C., . . . Shih, C.-K. (2017). Interlayer couplings, Moiré patterns, and 2D electronic superlattices in MoS2/WSe2 hetero-bilayers. *Science Advances, 3*(1), e1601459. doi:10.1126/sciadv.1601459
22. Zhang, Z., Li, J., Yang, G., & Ouyang, G. (2019). Interface Engineering of Band Evolution and Transport Properties of Bilayer WSe2 under Different Electric Fields. *Journal of Physics Chemistry, 123*(32), 19812-19819. doi:https://doi.org/10.1021/acs.jpcc.9b06828
23. Förg, M., Basimuratov, A. S., Kruhcinin, S. Y., Vovk, I. A., Scherzer, J., Förste, J., . . . Högele, A. (2021). Moiré excitons in MoSe2-WSe2 heterobilayers and heterotrilayers. *Nature Communications, 12*, 1-7. doi:https://doi.org/10.1038/s41467-021-21822-z
24. Zhang, Y., Zhan, Z., Guinea, F., Silva-Guillen, J. A., & Yuan, S. (2020). Tuning band gaps in twisted bilayer MoS2. *Physical Review B, 102*(23), 235418. doi:https://link.aps.org/doi/10.1103/PhysRevB.102.235418
25. Brotons-Gisbert, M., Baek, H., Molina-Sanchez, A., Cambell, A., Scerri, E., White, D., . . . Gerardot, B. D. (2020). Spin–layer locking of interlayer excitons trapped in moiré potentials. *Nature Materials, 19*, 630-636. doi:https://doi.org/10.1038/s41563-020-0687-7
26. Zhan, Z., Zhang, Y., Lv, P., Zhong, H., Yu, G., Guinea, F., . . . Yuan, S. (2020). Tunability of multiple ultraflat bands and effect of spin-orbit coupling in twisted bilayer transition metal dichalcogenides. *Physical Review B, 102*, 1-6. doi:10.1103/PhysRevB.102.241106
27. Lin, X., Zhu, H., & Ni, J. (2020). Pressure-induced gap modulation and topological transitions in twisted bilayer and twisted double bilayer graphene. *Physical Review B, 101*, 1-10. doi:10.1103/PhysRevB.101.155405

28. Chittari, B. L., Leconte, N., Javvaji, S., & Jung, J. (2018). Pressure induced compression of flatbands in twisted bilayer graphene. *Electronic Structure, 1*, 1-7. doi:10.1088/2516-1075/aaead3
29. Carr, S., Fang, S., Jarillo-Herrero, P., & Kaxiras, E. (2018). Pressure dependence of the magic twist angle in graphene superlattices. *Physical Review B, 98*, 1-5. doi:10.1103/PhysRevB.98.085144

Chapter Six Summary and Outlook

6.1 Summary

This dissertation focused on methods to synthesize, characterize, and simulate properties of two-dimensional materials. These methods are important in the discovery and characterization of new materials that could possibly replace the digital electronics that rely on silicon technology.

The main methods that were used for synthesis included polymer transferred graphene and molecular beam epitaxy. We covered the components and conditions required to create these samples including growing high quality crystalline materials in a UHV chamber using molecular beam epitaxy. Using these methods, we create samples of polymer transferred graphene onto arbitrary substrates and grow samples of FeSe on epitaxial graphene and STO.

We demonstrated typical methods used to characterize the success of transferred graphene using Raman spectroscopy and atomic force microscopy. In the AFM imagery, we can clearly see that the polymer transferred graphene produces ripples and ridges on the surface indicate a non-uniform contact with the surface of the substrate. This non-uniform contact was confirmed by STS studies as well as temperature dependent IV measurements. The temperature dependent IV characteristics show that the Schottky barrier had temperature dependence indicating an imperfect contact that was later model using a Gaussian distribution of barrier heights.

We doped the monolayer and bilayer TMD films with manganese, iron, and copper where observed a large induced magnetic moment in copper doped films and a non-zero off-diagonal component to the dielectric function. The copper creates flat impurity bands that lie

around the Fermi level within the gap. The copper atom hybridized with the local chalcogens and the next nearest metal atoms to form a state that is extended in plane and out of plane. The filling of the states up to the Fermi level, which results in unpaired spins, accounts for the magnetic moment of these materials.

We studied twisted bilayer TMDs as a function of twist angle and interlayer separation to determine that stronger interaction between the layers can give rise to flat bands. This electronic information was calculated using DFT and VASP to produce the energy band structure, density of states information, and charge density distribution to confirm the states that contribute to the flat bands. These flat bands create localized charge densities around the chalcogens that are in closest proximity along with the surrounding metal atoms.

Lastly, we looked at the effect of adding a copper replacement to the compressed twisted bilayer TMDs. We saw that the flat band states from the copper impurity and the flat band states from the twist were not close enough energy to overlap and interact. Adding the twist to the copper replacement suppressed the observed magnetic moment and the effect of a non-zero off-diagonal component to the optical response. Also, the simulated STM imagery is dominated by the effect of adding the copper replacement and any effect of the twist is suppressed.

6.2 Outlook

Considering the breadth of material covered in this dissertation, there are many new aspects that can be investigated. Devices of polymer transferred graphene that have extremely small channels can be studied [1,2]. This can take advantage of graphene's high mobility and also induce a gap making it a suitable replacement for transistor-based devices. There are

other aspects of the twisted bilayer TMD structures that can be investigated such as including relaxation, investigating other twist angles, investigating other structural properties, as well as using different metal or chalcogen atoms. Investigation of the flat bands for the $\sqrt{13}\ x\ \sqrt{13}$ supercells, where θ = 27.796° with an interlayer separation of 5.2 Å, around the energy level of -0.5 eV where we see the real space localization can lead to the possible creation of a quantum dot lattice.

References

1. Chen, Z., Narita, A., & Müllen, K. (2020). Graphene Nanoribbons: On-Surface Synthesis and Integration into Electronic Devices. *Advanced Materials, 32*, 1-26. doi:10.1002/adma.202001893
2. Kato, T., Kitada, T., Seo, M., Okita, W., Sato, N., Shinozaki, M., . . . Otsuka, T. (2022). Scalable fabrication of graphene nanoribbon quantum dot devices with stable orbital-level spacing. *Communications Materials, 3*, 1-7. doi:https://doi.org/10.1038/s43246-022-00326-3
3. Davenport, J. W., Watson, R. E., & Weinert, M. (1988). Linear augmented-Slater-type-orbital method for electronic-structure calculations. V. Spin-orbit splitting in Cu3Au. *Physical Review B, 37*, 9985-9992. doi:https://doi.org/10.1103/PhysRevB.37.9985
4. Sharan, A., Gui, Z., & Janotti, A. (2017). Hybrid-Functional Calculations of the Copper Impurity in Silicon. *Physical Review Applied, 8*, 1-12. doi:10.1103/PhysRevApplied.8.024023

Curriculum Vitae

Lawrence Hudy
lawrence.hudy@gmail.com

Education

PhD Physics August 2023
University of Wisconsin – Milwaukee, Milwaukee, WI
Dissertation title: "Synthesis, Characterization, and Simulation of Two-Dimensional Materials"

MS Physics May 2012
Texas Tech University, Lubbock, TX

BS Physics May 2010
Marquette University, Milwaukee, WI

Teaching Experience

Teaching Assistant
Physics Department, *University of Wisconsin-Milwaukee*, Milwaukee, WI

- Taught introductory physics lab courses

Teaching Assistant
Physics Department, *Texas Tech University*, Lubbock, TX

- Taught introductory astronomy lab courses – taught into astronomy concepts, operated TTU observatory telescopes

Teaching Assistant
Physics Department, Marquette University, Milwaukee, WI

- Taught introductory physics lab courses

Technical Skills

- Programming languages: C/C++, python, Java, Matlab, delphi pascal, LabVIEW
- Scripting languages: python, BASH, perl
- Data analysis: custom fitting functions and routines, cleaning and parsing data
- Computer aided design: AutoCAD, AutoCAD Inventor
- Micro-fabrication: Class 1000 cleanroom processes, photolithography, wet chemical etching, reactive ion etching, wire bonding
- Thin film deposition: thin film sputtering, e-beam evaporation, molecular beam epitaxy
- Thin film characterization: optical microscopy, atomic force microscopy, Raman spectroscopy, scanning tunneling microscopy/spectroscopy
- Device characterization: carrier transport measurements (IV characteristics, Hall measurements)

Research Experience

Research Assistant
Physics Department, University of Wisconsin-Milwaukee, Milwaukee, WI

- Program linear drive for precise sampling dipping

- Designed 4-point probe/Van der Pauw/Hall bar station to perform temperature dependent IV characteristics
- Programmed meters and interface for temperature dependent IV characteristics
- Designed and built e-beam substrate heating apparatus

Research Assistant
Physics Department, Texas Tech University, Lubbock, TX
- Analyzed muonium spectroscopy data related to III-IV compounds to determine muon spin relaxation, rotation, and resonance transition rates

Research Assistant
Physics Department, Marquette University, Milwaukee, WI
- Relocated new lab. Designed radiation protection and shielding for positronium experiments

Presentations and Publications

Presentations

- Hudy, L. J., Liu, Y., Weinert, M., Li, L. Measuring the Charge of a Defect in Graphene using Atomic Force Microscopy [Oral Presentation] APS March meeting 2014, Denver, CO

Publications

- Tomer, D., Rajput, S., **Hudy, L. J.**, Li, C. H., & Li, L. (2014). Intrinsic inhomogeneity in barrier height at monolayer graphene/SiC Schottky junction. *Applied Physics Letters, 105*, 021607. doi:10.1063/1.4890405
- Tomer, D., Rajput, S., **Hudy, L. J.**, Li., C. H., & Li, L. (2015). Inhomogeneity in barrier height at graphene/Si (GaAs) Schottky junctions. *26*(21), 215702.
- Tomer, D., Rajput, S., **Hudy, L. J.**, Li., C. H., & Li, L. (2015). Carrier transport in reverse-biased graphene/semiconductor Schottky junctions. *Applied Physics Letters, 106*, 173510. doi:10.1063/1.4919727
- **Hudy, L. J.** & Weinert, M. Pressure Induced Triangular Quantum Dot Lattice. In preparation

Honors and Awards

David Lichtman Memorial Scholarship for Experimental Research 2016
University of Wisconsin-Milwaukee

Graduate Student Excellence Fellowship 2016
University of Wisconsin-Milwaukee

Research Excellence Award 2012-2015
University of Wisconsin-Milwaukee

Gott Gold Tooth Award for Astronomy 2011
Texas Tech University